



저작자표시-비영리-변경금지 2.0 대한민국

이용자는 아래의 조건을 따르는 경우에 한하여 자유롭게

- 이 저작물을 복제, 배포, 전송, 전시, 공연 및 방송할 수 있습니다.

다음과 같은 조건을 따라야 합니다:



저작자표시. 귀하는 원 저작자를 표시하여야 합니다.



비영리. 귀하는 이 저작물을 영리 목적으로 이용할 수 없습니다.



변경금지. 귀하는 이 저작물을 개작, 변형 또는 가공할 수 없습니다.

- 귀하는, 이 저작물의 재이용이나 배포의 경우, 이 저작물에 적용된 이용허락조건을 명확하게 나타내어야 합니다.
- 저작권자로부터 별도의 허가를 받으면 이러한 조건들은 적용되지 않습니다.

저작권법에 따른 이용자의 권리와 책임은 위의 내용에 의하여 영향을 받지 않습니다.

이것은 [이용허락규약\(Legal Code\)](#)을 이해하기 쉽게 요약한 것입니다.

[Disclaimer](#)



이학박사 학위논문

Effects of mesoscale circulation
on internal wave enhancements in
the southwestern East Sea

동해 남서부 해역의 내부파 증폭에 미치는
중규모 순환 효과

2021년 8월

서울대학교 대학원
지구환경과학부
노수연

Effects of mesoscale circulation on internal wave enhancements in the southwestern East Sea

지도 교수 남 성 현

이 논문을 이학박사 학위논문으로 제출함

2021년 8월

서울대학교 대학원
지구환경과학부
노 수 연

노수연의 이학박사 학위논문을 인준함

2021년 8월

위원장 조 양 기

부위원장 남 성 현

위원 나 한 나

위원 박 재 훈

위원 변 상 신

Abstract

Effects of mesoscale circulation on internal wave enhancements in the southwestern East Sea

Suyun Noh

School of Earth and Environmental Sciences

The Graduate School

Seoul National University

Oceanic internal wave frequency range from inertial frequency to buoyancy frequency are ubiquitous in the stratified rotating ocean. They are mainly generated by wind, tide and current, propagate away from generation site, and ultimately dissipate. The internal wave-driven mixing affects vertical transport of water, heat, and consequently contribute maintain the thermohaline circulation, marine ecosystem, and climate system.

Near-inertial internal waves and internal tides are two types of low-frequency internal waves. Their interactions, interaction with mesoscale flow field, and resulting internal waves at higher frequencies beyond the near-inertial and tidal frequencies (continuum frequency waves) have rarely been reported despite its importance on ocean mixing and circulation of energy and materials.

This dissertation investigates enhancements of continuum frequency waves (CFWs) observed in the southwestern East Sea and discuss causes for the enhanced CFWs in relation to near-inertial waves (NIWs), semidiurnal internal tides (SDITs),

mesoscale flow fields, and their interactions (Chapter 2). The NIWs were amplified due to local surface wind forcing, significantly interacting with mesoscale strain via wave capture process. The SDITs were generated in a remote place and propagated into the observational site, largely depending on the mesoscale fields. The observational results suggest that the episodes of CFWs are results of enhanced NIWs or SDITs, or their wave-wave interaction, rather than locally generated lee-waves. In Chapter 2, it is highlighted that the significant impact of mesoscale circulation on the variability of internal waves from near-inertial to buoyancy frequencies through multiple pathways.

The NIWs of typhoon origin under varying mesoscale circulation, especially Ulleung Warm Eddy (UWE), are investigated using damped slab model in Chapter 3. Without local passage of typhoon, the wind stress was favorable to generate NIWs since they lasted nearly local inertial period with clockwise rotation during Events 1–3. The extension and shrinking of UWE also played an important role in the NIW amplification by including or excluding the mooring site within the UWE. The wind-induced NIWs was trapped and effectively enhanced in the region of anticyclonic eddy (negative relative vorticity) due to the lowered effective Coriolis frequency.

Intraseasonal (3–100 days) variations of near-inertial kinetic energy at 400m is analyzed using the 21-year-long time-series data from 2000 to 2020. In Chapter 4, considering the impact of mesoscale flows on NIWs, the rate of wind work, relative vorticity, total strain, Okubo-Weiss parameter are composited. Composite analysis reveals that the negative relative vorticity and positive Okubo-Weiss parameter (dominant total strain) imposed by mesoscale flow fields, rather than surface wind forcing, play a decisive role in enhancing NIW kinetic energy at 400 m to a degree of statistically significant level as providing favorable condition. This chapter reveals

the NIWs below the surfaced mixed layer are under the statistically significant influence of the mesoscale flow fields varying on intraseasonal, interannual, and decadal as well as seasonal time scale.

Statistical results on intraseasonal variations of semidiurnal kinetic energy at 400 m is presented in Chapter 5. The variations of semidiurnal kinetic energies are dominant at periods around 14, 28, and 56 days related to fortnight, sidereal month, and mesoscale circulations. When the characteristic slope matches the bottom slope at the northern slope of the Korea Strait, the intraseasonal variations of semidiurnal kinetic energies are higher than those of another period with 95 % significance. The generated SDIT propagates poleward interacting with mesoscale circulation.

This study highlights that the significant impact of mesoscale circulation on the variability of NIWs, SDITs, and CFWs in intraseasonal, interannual, and decadal time scale.

Keyword: Near-inertial waves, semidiurnal internal tides, continuum frequency waves, mesoscale variability, wave-wave interaction, Nonseasonal variation, intraseasonal variation

Student Number: 2014-30095

Table of Contents

Abstract.....	i
Table of Contents.....	iv
List of Figures	vii
List of Tables	xiii
1. General introduction.....	1
1.1. Background	1
1.2. Purpose of study.....	6
2. Enhanced internal waves interacting with mesoscale circulations in 2003	7
2.1. Introduction	7
2.2. Data and method	11
2.2.1. Data	11
2.2.2. Method.....	13
2.3. Results.....	23
2.3.1. Temporal variations of ehnanced internal wave energy	23
2.3.2. Changes in horizontal kinetic energy spectra	27
2.4. Discussion	29
2.4.1. NIW generation by local wind forcing.....	29
2.4.2. Interaction between mesosacle flow field and NIWs	36
2.4.3. SDIT generation at the Korea Strait	39
2.4.4. Interaction between mesoscale field and SDITs.....	41
2.4.5. CFW enhancement by interaction between NIWs and SDITs.....	43
2.5. Conclusion	45
3. NIWs of typhoon origin observed in 2015.....	47
3.1. Introduction	47
3.2. Data and method	50
3.2.1. Data	50
3.2.2. Method.....	52
3.3. Results.....	54
3.3.1. Wind forced periods	54
3.3.2. Temporal and vertical variations of observed NIWs	57
3.4. Discussion.....	60

3.4.1. Unfavorable wind conditions for NIWs under the local typhoon passage	60
3.4.2. Favorable wind conditions for NIWs induced by local and remote passage of typhoon.....	61
3.4.3. Favorable and unfavorable mesoscale conditions for NIWs modulated by relative vorticity.....	65
3.5. Conclusion	68
4. Nonseasonal variability of near-inertial kinetic energy from 21-year-long observations	70
4.1. Introduction	70
4.2. Data and method	73
4.2.1. Data	73
4.2.2. Method.....	76
4.3. Results.....	82
4.3.1. Intraseasonal, interannual, and decadal variations of KE _{NIW} at 400 m and NIWs in mixed layer.....	82
4.3.2. Composite analysis of KE _{NIW} at 400 m and mesoscale conditions ...	85
4.4. Discussion	90
4.4.1. Comparision between observed and modelled NIWs.....	90
4.4.2. Effects of surface wind forcing on KE _{NIW} below the mixed layer....	92
4.4.3. Effects of mesoscale flow fields on KE _{NIW} below the mixed layer ...	94
4.5. Conclusion	97
5. Nonseasonal variability of semidiurnal kinetic energy from 21-year-long observations	98
5.1. Introduction	98
5.2. Data and method	100
5.2.1. Data	100
5.2.2. Method.....	102
5.3. Results.....	104
5.4. Discussion	107
5.4.1. Surface tidal forcing	107
5.4.2. Conditions for SDIT generation	109
5.4.3. Conditions for SDIT refraction.....	111

5.5. Conclusion	115
6. Conclusion.....	117
References	120
Abstract in Korean.....	128
Appendix	131

List of Figures

Figure 1.1. Schematic of internal wave generation and internal wave-driven mixing process in the ocean.	1
Figure 1.2. Global energy budget of internal waves.....	3
Figure 1.3. Global mode-1 M_2 internal tide models from satellite altimetry.....	4
Figure 2.1. Geographic map of the southwestern East Sea with bathymetry (color). Location of a subsurface mooring named EC1 is marked by the red square. Grey circles and dotted line indicate the path of the center of typhoon Maemi. The red hatched area represents location where SDITs can be generate. Wind stress data averaged over the area are denoted with the blue rectangle.	12
Figure 2.2. (a) Time-depth contour of Buoyance frequency N derived using Lim et al. (2012). Vertical profiles of (b) buoyance frequency and (c) WKB factor for Events (color) in 2003	15
Figure 2.3. Monthly mean Ekman currents and wind in June 2003.....	20
Figure 2.4. Aliasing sensitivity test for CFW band.	22
Figure 2.5. Time-depth contours of WKB-scaled (a) KE_{NIW} , (b) KE_{SDIT} , (c) KE_{CFW} , (d) $KE_{NIW}+KE_{SDIT}$, and (e) $KE_{NIW+SDIT}$ are plotted, respectively. The KE_{CFW} , $KE_{NIW}+KE_{SDIT}$, and $KE_{NIW+SDIT}$ were 40-hour low-passed. Here, the $KE_{NIW}+KE_{SDIT}$ and $KE_{NIW+SDIT}$ represent summation and interaction of NIWs and SDITs, respectively, whereas KE_{NIW} , KE_{SDIT} , and KE_{CFW} are directly estimated from NIWs, SDITs, and CFWs, respectively. Five events are denoted by grey boxes. Each color box in (a)–(e) represents enhanced NIWs only with no enhancements of SDITs or CFWs (purple), enhanced CFWs only with no enhancements of NIWs or SDITs (green), enhanced NIWs and CFWs with no SDIT enhancement (black), enhanced SDITs and CFWs with no NIW enhancement (red), and enhanced NIWs, SDITs, and CFWs (blue). Timings of spring tide at the nearby tide-gauge station (Ulleungdo) are denoted by triangles in (b)	25
Figure 2.6. Frequency spectra of horizontal kinetic energy observed at 77 m (purple), 153 m (red), 200 m (orange), and 360 m (blue) during (a) Event 1, (b) Event 2, (c) Event 3, (d) Event 4, and (e) Event 5, respectively.	

Diagonal lines in bottom-left corners show fall-off rates or spectral slopes of -1, -2, and -3. Three internal wave bands of NIW (yellow), SDIT (red), and CFW (grey) are shaded with colors.....28

Figure 2.7. Time series of (a) wind stress in N m^{-2} averaged over the area shown in Fig. 2.1, (b) rate of work done by the surface wind at location nearest to EC1 (black) and averaged over the area (red) in W m^{-2} , (c) amplitude of NIWs observed at 53 m, (d) amplitude of NIWs calculated using the damped slab model for four cases. (e) Hovmöller diagram of the energy transfer efficiency in logged colour scale shown in the right at 131.43°E (longitude of EC1) as functions of time and latitude where dashed lines indicate the effective Coriolis frequency normalised by f at the surface (contour interval: $0.02f$).....31

Figure 2.8. Time-depth contour of meridional component of NIW during (a) Event 1, (b) Event 2, (c) Event 3–4, and (d) Event 5.....32

Figure 2.9. Maps of surface geostrophic currents derived from satellite altimetry (vectors) and vertical relative vorticity (color). (h) October 22 and (k) November 20 corresponding to early Event 3 and late Event 4, respectively. The EC1 location is demarcated by the red square. The geostrophic currents over the 0.3 m s^{-1} are shown in red arrows.....33

Figure 2.10. Maps total strain (colors) and Okubo-Weiss parameters α^2 (dotted contours) at -2×10^{-11} (blue), -1×10^{-11} (cyan), 0.0 (black), 1×10^{-11} (orange), and 2×10^{-11} (red). (h) October 22 and (k) November 20 corresponding to early Event 3 and late Event 4, respectively. The EC1 location is demarcated by the red square.....34

Figure 2.11. Time series of (a) 15-days low-passed subinertial zonal and (b) meridional currents. The absolute vertical shear of (a) and (b) are shown in (c). The horizontal shear of density estimated from thermal wind are shown in (d) and (e).35

Figure 2.12. Time series of (a) total strain (red, left axis) and vertical relative vorticity (blue, left axis) normalized to f , and Okubo-Weiss parameter α^2 (thick grey, right axis) normalized to f^2 at the EC1 location. (b) Subinertial kinetic energy averaged from 53 to 360 m. (c) rate of energy transfer from mesoscale fields to internal waves. Red (blue) colour denotes positive

(negative) Okubo-Weiss parameter α^2 . (d) Energy level (E_{fit}) and (e) slope (S_{fit}) fitted to observed frequency spectrum of horizontal kinetic energy shown in Fig. 2.2. Horizontal bars in (e) indicate the slope averaged over period when $E_{fit} > 7 \times 10^{-5} \text{ m}^2 \text{ s}^{-2} \text{ cph}^{-1}$ and $S_{fit} > -2$. Periods of five events are grey shaded in (a)–(e).....	38
Figure 2.13. Schematics of SDIT propagation from the generation site (the northern slope of the Korea Strait) following the background condition.....	42
Figure 2.14. Hovmöller diagram (longitude and time plot) of the sea surface height (SSH) at the northern slope of the Korea Strait. Timings of spring tide at nearby tide-gauge station (Busan) are denoted by triangles.....	42
Figure 3.1. Track of typhoons with the central pressure (colored circles) superimposed on the absolute dynamic topography averaged from 15 March to 2 September 2015 (color shading) with the surface geostrophic currents (grey arrows). The EC1 is marked by red square.	51
Figure 3.2. Time series of (a) wind stress amplitude $\sqrt{\tau_x^2 + \tau_y^2}$, (b) near-inertial wind stress, (c) rate of work done by wind, (d) temporal integral of (c), (e) KE _{NIW} estimated by damped slab model (black line, left y-axis) and observed at uppermost 22 m (red line, right y-axis). Time-depth contours of observed (f) KE _{NIW} in log scale, (g) zonal and (h) meridional components of subinertial currents. In (b), red and blue lines indicate τ_x and τ_y	56
Figure 3.3. Meridional components of NIWs during (a) Event 1, (b) Event 2, (c) Event 3, and (d) Event 4.	58
Figure 3.4. Vertical structure of KE _{NIW} and NIW frequencies during (a) Event 1, (b) Event 2, (c) Event 3, (d) Event 4, and (e) typhoon passing period in July.	59
Figure 3.5. Geopotential height and wind (vectors) at 850 hPa. The dashed lines indicate typhoon track and red square represent the EC1.	63
Figure 3.6. Time series of wind stress amplitude (red thick line), wind direction (blue dots), and near-inertial wind direction (grey dots).	64
Figure 3.7. Time series of relative vorticity (red), total strain (blue), and Okubo-Weiss parameter (black) near the EC1. Each term is normalized by f or f2.	

Shaded boxes indicate event periods.	65
Figure 3.8. Maps of geostrophic currents (grey arrows) and relative vorticity (colour shading). Red and blue dotted lines indicate the boundaries of anticyclonic and cyclonic eddies which are detected by eddy tracking method. Black dot indicates the center of eddy. The EC1 is marked by green square.	67
Figure 4.1. Location of subsurface mooring EC1 (red square) with bathymetry (color) in the southwestern East Sea off the east coast of Korea. Green dotted line indicates meridional line where sea surface wind data are extracted. Black dashed lines indicate trajectories of typhoon Maemi (2003-14), Megi (2004-15), and Maysak (2020-09). The yellow circles indicate 30, 100 and 200 km radius centered at EC1, respectively.	75
Figure 4.2. A flow chart for processing of horizontal current data.....	78
Figure 4.3. Monthly MLD estimated from EN4 (black line) compared to that from Lim et al. (2012) (yellow dot).	79
Figure 4.4. Time-series of normalized intraseasonal variations of KENIW at 400 m ($KE_{NIW_obs_int}$) from 2000 to 2020. Red (blue) shaded boxes indicate Period High (Period Low) and gray shaded area indicates Period Neutral. White area represents the data gap (no data available). The Events 2–4 in Noh and Nam (2020) are marked at the top of H2 (pink).	83
Figure 4.5. Time-series of (a) wind stress amplitude, (b) near-inertial wind stress, (c) Π (left axis) and time integral of Π showing cumulative energy input from surface wind to MLD currents (green solid line, right axis), and (d) near-inertial amplitude in MLD, $\sqrt{u_{ML}^2 + v_{ML}^2}$, calculated from damped slab model results, and (e) intraseasonal variations of (d). Pink line in (e) indicates intraseasonal variations $\sqrt{u_{ML}^2 + v_{ML}^2} - \sqrt{u_{ML}^2 + v_{ML}^2}$ averaged over 38–40 °N. Red (blue) shaded boxes indicate Period High (Period Low). Gray shaded area indicates Period Neutral. Green triangle in (d) indicates the period when the near-inertial amplitude in MLD is larger than 1 m s ⁻¹	84
Figure 4.6. Time-series of (a) S^2 normalized by f, (b) ζ normalized by f, and (c) α^2 normalized by f2. Red (blue) shaded boxes indicate Period High	

(Period Low). Gray shaded area indicates Period Neutral.	86
Figure 4.7. Ray path of NIWs (thick white solid line) in the spatially varying stratification in March 2018 corresponding H8. Yellow solid line indicates ray path that can reach a depth of 400 m at EC1 (yellow star). Background color indicates potential temperature, and dashed line indicates potential density.	93
Figure 4.8. Time-series of (a) monthly Buoyancy frequency at 50 m (gray line, right y-axis) and 400 m (black line, left y-axis) derived from EN4, (b) WKB scale factor at 400 m with reference density, 0.0046 rad s-1, (c) and (d) indicate annual mean of (a) and (b). Dashed lines in (a) – (d) indicate temporal mean. Blue thick line in (c) and (d) represent linear trend from 2000 to 2020.	96
Figure 5.1. Geographic map of the southwestern East Sea with topography (color). Location of subsurface mooring, EC1, is marked by yellow square. The NIFS stations and KHOA tidal gauge are shown by blue circles and red triangle. Red hatched area represents SDIT generation site.	101
Figure 5.2. Wavelet power spectrum and global power spectrum of (a) η_{SD}^2 at Busan and (b) KESDIT at 400 m. Time series of (c) intraseasonal KESDIT averaged (b) for 3~100 days band. In (c), Red (blue) shaded area indicate Period High (Period Low). Gray shaded area indicates Period Neutral. In (b) and (c), white area represents data gap (no available data). (d) Annual mean of (c) with standard deviation (gray shading). Red thick line in (d) indicate mean over the period that detected by STARS.	105
Figure 5.3. Annual mean of η_{SD}^2 in 3–100 days band. Red line indicates mean values during the periods that detected by STARS. Gray shading indicates standard deviation. Red and blue square markers represent maximum and minimum.	106
Figure 5.4. Nodal factor for M2 (left y-axis) and S2 (right y-axis) near the tidal-gauge station.	108
Figure 5.5. Time-series of (a) buoyancy frequency at 175 and 200 m in 209-08 station, (b) γ , (c)–(d) $\gamma - s$, (e) annual mean of (a), and (f) annual mean of (b). In (b), dashed lines represent possible topographic slope (s) near the SDIT generation site. In (a)–(d), red (blue) shaded area indicate Period	108

High (Period Low). Gray shaded area indicates Period Neutral. White area represents data gap (no available data).	110
Figure 5.6. Time-series of (a) ΔADT and (b) $ \gamma - s $. In (a), positive value means the possibility of eastward refraction, and vice versa. In(a), red and blue circles represent positive and negative steric height anomaly between 209-07 and 209-08 station. In (b), dotted line indicates the threshold with 0.01. Red (blue) shaded area indicate Period High (Period Low). Gray shaded area indicates Period Neutral. White area represents data gap (no available data).	113
Figure 5.7. Composite maps of ADT (color shading, unit: m) and satellite altimetry-derived geostrophic currents (gray vectors) for (a) Case 1, (b) Case 2, (c) Case 3, and (d) Case 4. The yellow square indicates the EC1, and red hatched area represent SDIT generation site.	114
Figure 5.8. Same as Figure 5.5, but for (a) before 2011, and (b) after 2011. ...	114
Figure 6.1. Schematic illustration of mechanisms underlying observed enhancements of internal waves in the southwestern East Sea. The SDIT, NIWs, and CFWs are shown in red, orange, and blue, respectively. The mechanisms relevant to observed enhancements of internal waves discussed in this (solid arrows) and previous (dashed arrows with colored label) studies (Park and Watts, 2006; Nam and Park, 2008; Byun et al., 2010, Jeon et al., 2014; 2019).	118
Figure 6.2. Schematics for (a) category I, (b) category II, (c) category III, and (d) category IV.	119

List of Tables

Table 2.1. Periods of internal wave events identified by 3-day low-passed, WKB-scaled CFW kinetic energy (KE_{CFW}) observed at the EC1 in 2003	16
Table 2.2. Selected wave-wave interaction frequencies for $KE_{NIW+SDIT}$	16
Table 2.3. Correlation coefficients between KE_{CFW} and $KE_{NIW} + KE_{SDIT}$ (top), KE_{CFW} and $KE_{NIW+SDIT}$ (middle), and $KE_{NIW} + KE_{SDIT}$ and $KE_{NIW+SDIT}$ (bottom). Coefficients where $p < 0.05$ are underlined.....	17
Table 3.1. Event periods and typhoons related to the events	55
Table 4.1. Mean and (bracket) standard deviation of five conditions during Period High.....	87
Table 4.2. Mean and (bracket) standard deviation of five conditions during Period Low	88
Table 4.3. Categories of the intraseasonal variations of KE_{NIW} by relative vorticity, total strain, and Okubo-Weiss parameter.....	89
Table 5.1. Annual mean of nonseasonal KE_{SDIT} at 400 m and data acquisition rate in each year.	106
Table 5.2. Cases depending on generation and refraction conditions, and KE_{SDIT} and $ \gamma - s $ averaged over the cases.....	113

1. General introduction

1.1. Background

Oceanic internal waves are ubiquitous in the stratified, rotating ocean, and play a key role in providing a significant portion of energy to induce turbulent mixing, and redistributing energy and materials in the ocean (Garrett and Munk, 1979; Munk and Wunsch, 1998; Müller and Briscoe, 2000; Alford, 2003; Ferrari and Wunsch, 2009). Flows over rough topography, perturbations at the base of mixed layer or fluctuation of mesoscale currents can generate internal waves (Figure 1.1). Internal waves at time scales from near-inertial to near-buoyancy periods are not always amplified at the same time, nor are their energies spatially homogeneous. They therefore have a potentially important spatio-temporal influence on distribute and redistribute of energy and materials and it plays important role in shaping the circulation, marine ecosystem and climate system (Jochum et al., 2013; Muacho et al., 2013; Melet et al., 2016; Villamaña et al., 21017; MacKinnon et al., 2017; Whalen et al., 2020).

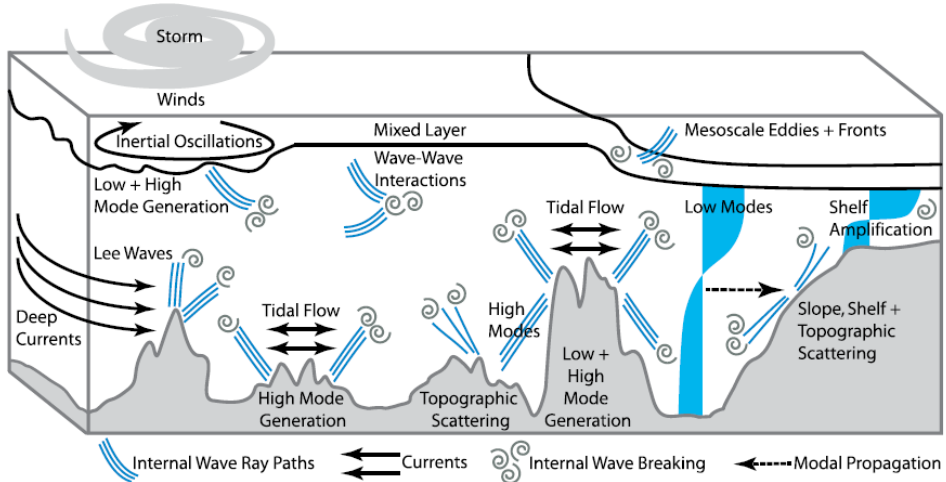


Figure 1.1. Schematic of internal wave generation and internal wave-driven mixing process in the ocean (MacKinnon et al., 2017).

Near-inertial waves (NIWs; internal waves at a frequency near the local inertial frequency, f) are often generated by storm passages, predominantly propagate equatorward (Alford, 2003; Garrett, 2001; Simmons and Alford, 2012; Alford, 2016). It is known that the wind rotates clockwise with time for a fixed location on the right side of typhoon in the Northern Hemisphere, permitting the resonance between wind and NIWs (Price, 1981; Chen et al., 2015). The range of work done by wind on inertial oscillation in mixed layer is known as from 0.3 to 1.3 TW which is comparable to converted power from barotropic to baroclinic tide (Jiang et al., 2005). They are significantly modified through interactions with mesoscale flows, and the energy exchange between NIWs and mesoscale eddies is believed to be important for the energy budget (Figure 1.2) (Kunze 1985; Ferrari and Wunsch, 2009; Byun et al., 2010; Danioux et al., 2011; Thomas, 2017; Vanneste, 2013; Whitt and Thomas, 2015; Jing et al., 2017; 2018), but the forcing mechanisms responsible for the process under the wind forcing are not always clear. According to recent studies analyzing the energy exchange using a modified slab model (including geostrophic flow) and realistic numerical simulations, a permanent energy transfer from mesoscale eddies to NIWs exists in the presence of strain with a transfer efficiency proportional to the total strain variance during the wind forcing stage (Whitt and Thomas, 2015; Jing et al., 2017). Relative vorticity has been suggested to not only induce the permanent energy transfer, but also affect the transfer efficiency in the presence of strain (Whitt and Thomas, 2015; Jing et al., 2017; Thomas, 2017). Recent studies noted that the strain of mesoscale flow fields plays an important role in NIW and mesoscale energy exchange via the wave capture process, allowing nonlinear interaction between NIWs and the mesoscale field, e.g., drawing NIW energy from the mesoscale flow (Bühler and McIntyre, 2005; Polzin, 2008; 2010). However, such interaction

between NIWs and the mesoscale field is not always clear in many seas due to a lack of in-situ observations.

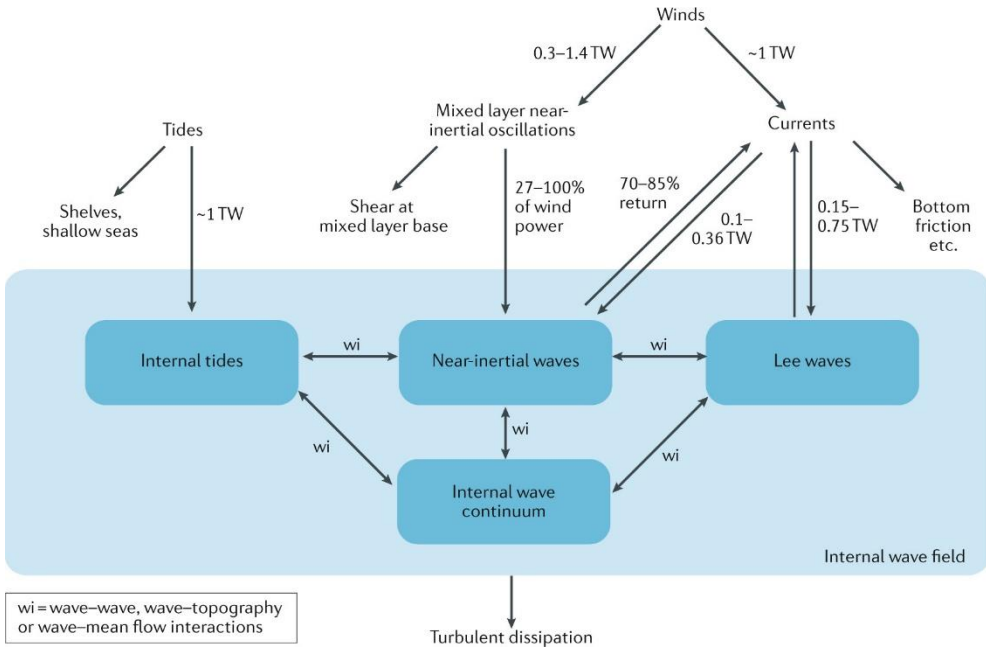


Figure 1.2. Global energy budget of internal waves (Whalen et al., 2020)

Ocean tides generate internal tide (also referred as baroclinic tides) as barotropic tidal flow (flow associated with surface tides) interacts with bottom topography (Wunsch, 1975; Garrett and Kunze, 2007). Diurnal and semidiurnal (SD) internal tides (ITs) are generated when and where their characteristic slope matches the bottom slope, propagate via interaction with background mesoscale conditions, and ultimately dissipate (Figures 1.1 and 1.3) (Baines, 1982; Park and Watts, 2006; Rainville and Pinkel, 2006; Dunphy and Lamb, 2014). In spite of the tremendous progress on SDITs and diurnal ITs, including global time averaged maps of barotropic to baroclinic conversion and internal tidal beams (Simmons et al., 2004; Niwa and Hibiya, 2014; Zhao et al., 2016; Zhao, 2019), spatio-temporal variability

of local generation, propagation, refraction, and dissipation (or damping) of SDITs and diurnal ITs in many seas, and their interactions are still poorly understood (Figure 1.3).

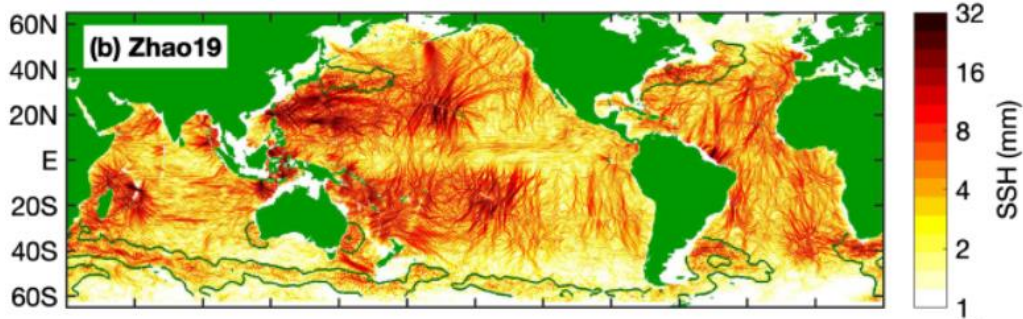


Figure 1.3. Global mode-1 M_2 internal tide models from satellite altimetry (Zhao et al., 2019)

Internal waves at higher frequencies (here, not corresponding internal solitary waves or nonlinear internal waves), have long been described by the classical Garrett-Munk (GM) spectrum (Garrett and Munk, 1975) and believed to arise from nonlinear wave-wave interactions transferring energy out of the NIWs and ITs into the broadband continuum (Figures 1.1 and 1.2) (Müller and Briscoe, 2000; Hibiya et al., 2002; Alford et al., 2017). As the level of the continuum or CFW (continuum frequency waves) energy is closely related to small-scale turbulent mixing, many works have been dedicated to better understand the processes underlying the variations of CFW energy and spectral departure from the GM spectrum. Recent studies suggested the relationship between observed mixing rates and internal wave generations along with lee-waves over rough topography, hypothesizing that the CFW energy comes only from the wind, tides, and mesoscale turbulence (Nikurashin et al., 2014; Clément et al., 2016; Hibiya et al., 2017). However, our understanding

on processes underlying the CFW energy variations in space and time are largely limited due to rare relevant observations.

In the southwestern East Sea off the east coast of Korea, the NIWs generated by local surface wind forcing have widely been observed and simulated in the region, yet their interactions with mesoscale field were examined in only few studies (Lee and Niiler, 1998; Shcherbina et al., 2003; Park and Watts, 2005; Nam et al., 2007; Nam and Park, 2013; Jeon et al., 2019). A semi-permanent anticyclonic eddy named Ulleung Warm Eddy (UWE) was found to affect the distribution of NIW energy in the region as discussed by Jeon et al. (2019). In addition, upward propagating NIWs due to the reflection of downward propagating NIWs back to the surface from the UWE thermostad were observed (Byun et al., 2010). However, the role of mesoscale strain in exchanging energy between NIWs and the mesoscale field has not been investigated thus far. Moreover, the mechanism of NIWs interacting with ITs and enhancing CFWs remained unanswered. Although diurnal ITs are mostly trapped in the southern Ulleung Basin near the generation area, northern slope of the Korea Strait, SDITs generated in the same area easily propagate poleward as located in the north of diurnal and south of SD critical latitudes (Simmons et al., 2004; Simmons, 2008), interacting with mesoscale circulation (Park and Watts, 2006; Nam and Park, 2008; Seo et al., 2006).

1.2. Purpose of study

This study aims at (1) characterizing the time and location of the enhancement of three kinds of internal waves (NIWs, SDITs, and CFWs) in the southwestern East Sea, and (2) addressing possible mechanisms to explain the enhanced CFWs in relation to those of NIWs, SDITs, their interactions, and interactions with the mesoscale field, and suggesting the comprehensive conditions that can affect (3) the enhancement of near-inertial internal waves, and (4) the generation and refraction of semidiurnal internal tides through statistical analysis.

2. Enhanced internal waves interacting with mesoscale circulations in 2003

2.1. Introduction

Internal waves are ubiquitous in the stratified, rotating ocean, and play a key role in providing a significant portion of energy to induce turbulent mixing, and redistributing energy and materials in the ocean (Garrett and Munk, 1979; Munk and Wunsch, 1998; Muller and Briscoe, 2000; Alford, 2003; Ferrari and Wunsch, 2009; MacKinnon et al., 2017). Internal waves at time scales from near-inertial to near-buoyancy periods are not always amplified at the same time, nor are their energies spatially homogeneous. They therefore have a potentially important spatio-temporal influence on the distribution and redistribution of energy and materials, and marine ecosystems (Lucas et al., 2011; Pan et al., 2012; Muacho et al., 2013; Villamana et al., 2017; Li et al., 2018).

Internal waves at a frequency near the local inertial frequency or near-inertial waves (NIWs) are often generated by storm passages, predominantly propagate equatorward (Alford, 2003; Garrett, 2001; Simmons and Alford, 2012; Alford et al., 2016), and are significantly modified through interactions with mesoscale flows (Kunze, 1985; Bühler and McIntyre, 2005; Polzin, 2008; 2010; Byun et al., 2010; Elipot et al., 2010; Xie and Vanneste, 2015). The energy exchange between NIWs and mesoscale eddies is believed to be important for the energy budget (Ferrari and Wunsch, 2009; Byun et al., 2010; Danioux et al., 2011; Thomas, 2017; Vanneste, 2013; Whitt and Thomas, 2015; Jing et al., 2017), but the forcing mechanisms responsible for the process under the wind forcing are not always clear. According to recent studies analysing the energy exchange using a modified slab model

(including geostrophic flow) and realistic numerical simulations, a permanent energy transfer from mesoscale eddies to NIWs exists in the presence of strain with a transfer efficiency proportional to the total strain variance during the wind forcing stage (Whitt and Thomas, 2015; Jing et al., 2017). Relative vorticity has been suggested to not only induce the permanent energy transfer, but also affect the transfer efficiency in the presence of strain (Thomas, 2017; Whitt and Thomas, 2015; Jing et al., 2017). Recent studies noted that the strain of mesoscale flow fields plays an important role in NIW and mesoscale energy exchange via the wave capture process, allowing nonlinear interaction between NIWs and the mesoscale field, e.g., drawing NIW energy from the mesoscale flow (Polzin, 2008; Polzin, 2010; Byun et al., 2010; Jing et al., 2018). However, such interaction between NIWs and the mesoscale field is not always clear in many seas due to a lack of in-situ observations.

Ocean tides generate another type of low-frequency internal wave or internal tide (also referred as baroclinic tides) as barotropic tidal flow (flow associated with surface tides) interacts with bottom topography (Wunsch, 1975; Garrett and Kunze, 2007; Banies, 1982). Diurnal and semidiurnal (SD) internal tides (ITs) are generated when and where their characteristic slope matches the bottom slope, propagate via interaction with background mesoscale conditions, and ultimately dissipate (Banies, 1982; Park and Watts, 2006; Rainville and Pinkel, 2006; Dunphy and Lamb, 2014). In spite of the tremendous progress on SDITs and diurnal ITs, including global time averaged maps of barotropic to baroclinic conversion and internal tidal beams (Simmons et al., 2004; Niwa and Hibiya, 2014; Zhao et al., 2016), spatio-temporal variability of local generation, propagation, refraction, and dissipation (or damping) of SDITs and diurnal ITs in many seas, and their interactions are still poorly understood.

Internal waves at higher frequencies (0.09–0.50 cph), defined here as continuum frequency waves (CFWs), have long been described by the classical Garrett-Munk (GM) spectrum (Garret and Munk, 1975) and believed to arise from nonlinear wave-wave interactions transferring energy out of the NIWs and ITs into the broadband continuum (Müller and Briscoe, 2000; Hibiya et al., 2002; Alford et al., 2017). As the level of the continuum or CFW energy is closely related to small-scale turbulent mixing, many works have been dedicated to better understand the processes underlying the variations of CFW energy and spectral departure from the GM spectrum. Recent studies suggested the relationship between observed mixing rates and internal wave generations along with lee-waves over rough topography, hypothesising that the CFW energy comes only from the wind, tides, and mesoscale turbulence (Nikurashin et al., 2014; Clément et al., 2016; Hibiya et al., 2017). However, our understanding on processes underlying the CFW energy variations in space and time are largely limited due to rare relevant observations.

In the southwestern East Sea off the east coast of Korea, the NIWs generated by local surface wind forcing have widely been observed and simulated in the region, yet their interactions with mesoscale field were examined in only few studies (Lee and Niiler, 1998; Shcherbina et al., 2003; Park and Watts, 2005; Nam et al., 2007; Nam and Park, 2013; Jeon et al., 2019). A semi-permanent anticyclonic eddy named Ulleung Warm Eddy (UWE) was found to affect the distribution of NIW energy in the region as discussed by Jeon et al. (2019). In addition, upward propagating NIWs due to the reflection of downward propagating NIWs back to the surface from the UWE thermostad were observed (Byun et al., 2010). However, the role of mesoscale strain in exchanging energy between NIWs and the mesoscale field has not been investigated thus far. Moreover, the mechanism of NIWs interacting with ITs and

enhancing CFWs remained unanswered. Although diurnal ITs are mostly trapped in the southern Ulleung Basin near the generation area, northern slope of the Korea Strait, SDITs generated in the same area easily propagate poleward as located in the north of diurnal and south of SD critical latitudes (Simmons et al., 2004; Simmons, 2008), interacting with mesoscale circulation (Park and Watts, 2006; Nam and Park, 2008; Seo et al., 2016).

2.2. Data and Method

2.2.1. Data

A subsurface mooring was deployed at an observational site (EC1, 37°19.13'N, 131°25.62'E) located between Ulleungdo and Dokdo in a water depth of 2200 m from November 2002 to April 2004 (Figure 2.1). The mooring was equipped with six single-point rotary-type current meters (RCMs) at 200, 360, 1000, 1365, 1685 and 2235 m, and an upward-looking acoustic Doppler current profiler (ADCP) of four 300 kHz beams at 160 m. Water temperature at 160 m and vertical profiles of horizontal currents at the upper 160 m were measured every hour with a depth interval (bin size) of 4 m (35 bins totally) using the ADCP. The current data collected at shallower than 53 m were not used here because they were presumably contaminated by the diurnal migration of marine biota (Plueddemann and Pinkel, 1989). Horizontal currents measured every 30 min at the RCMs were subsampled at a 1 h interval. Details on the moored time-series measurements are provided by Kim *et al.* (2009) and Noh and Nam (2018). This study was used the time-series data collected at the upper 360 m from June 15 to December 31 in 2003.

Surface mixed layer depth (MLD) and buoyancy frequency N were estimated using Lim *et al.* (2012) that were based on the World Ocean Database 2005 and multi-source hydrographic data. The MLD averaged over the observation period is 34 m having seasonal variation with a typical amplitude of ~20 m. To supplement the EC1 mooring observation, surface geostrophic currents calculated by satellite altimetry-derived SSH of gridded level 4 data were used where horizontal and temporal resolutions are 0.25° and 1 day, respectively. Sea surface wind data derived from spatial blending of QuikSCAT satellite and NCEP reanalysis surface wind data

with an interval of 6 h and horizontal resolution of 0.5° were used to estimate wind stress; $\vec{\tau} = (\tau_x, \tau_y)$. This study used hydrography data collected every second month in 2003 in the generation area of ITs in the north of the Korea Strait.

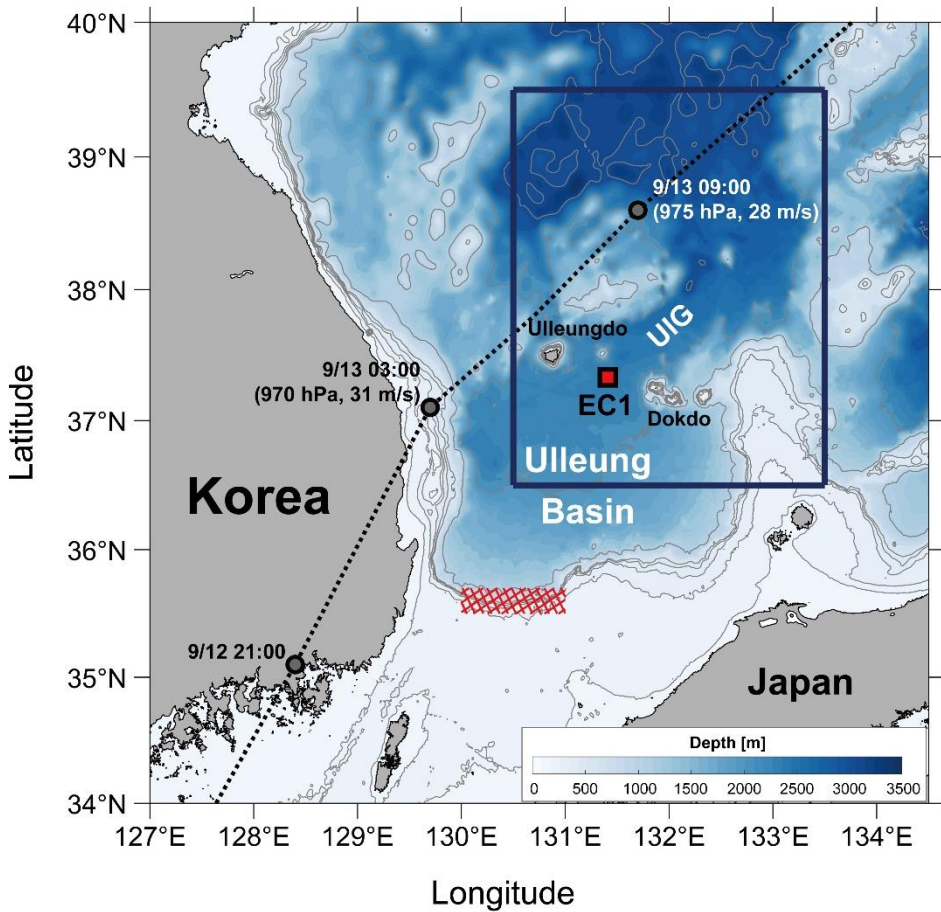


Figure 2.1. Geographic map of the southwestern East Sea with bathymetry (color). Location of a subsurface mooring named EC1 is marked by the red square. Grey circles and dotted line indicate the path of the center of typhoon Maemi in 2003. The red hatched area represents location where SDITs can be generate. Wind stress data averaged over the area are denoted with the blue rectangle.

2.2.2. Method

Three types of internal waves, NIWs (u_{NIW}, v_{NIW}), SDITs (u_{SDIT}, v_{SDIT}), and CFWs (u_{CFW}, v_{CFW}), were defined with cut-off frequencies as $[0.85f, 1.15f]$, $[0.95M_2, 1.05M_2]$ and $[1.8f, 8.5f]$, respectively, where the square brackets [] represent lower and upper limits of the waves; f and M_2 are local inertial frequency (~ 0.0505 cph) and SD tidal frequency (~ 0.0805 cph); u and v represent zonal and meridional components of horizontal current and subscripts of NIW, SDIT, and CFW denote corresponding waves. To extract three frequency bands, fourth-order Butterworth filters were applied to the hourly time series of the observed horizontal currents (u, v) at each depth. To preserve the phase, the filter was applied forward and backward, and the defined bands were not overlapped. The CFW, representing the high-frequency band of internal waves towards the buoyancy frequency, includes interaction frequencies between NIWs and SDITs and among higher tidal harmonics.

Horizontal kinetic energies of these waves (KE_{NIW} , KE_{SDIT} , and KE_{CFW}) were computed as $0.5\rho_0(u_{NIW}^2 + v_{NIW}^2)$, $0.5\rho_0(u_{SDIT}^2 + v_{SDIT}^2)$, and $0.5\rho_0(u_{CFW}^2 + v_{CFW}^2)$ in joules per cubic metre ($J \text{ m}^{-3}$), where ρ_0 is the reference density ($= 1024.0 \text{ kg m}^{-3}$). To minimise the effects of stratification on the kinetic energy, the WKB-scaled (Leaman and Sanford, 1975) band-passed currents were used by applying $u_{WKB} = u(z, t)\{N(z, t)/N_0\}^{-1/2}$, where buoyancy frequency $N = \{-(g/\rho_0)/(d\rho/dz)\}^{1/2}$, and z, t, N_0, g , and ρ are the vertical coordinate, time, reference buoyancy frequency (set to 2.86 cph based on regional observation at the upper 500 m), gravity constant (set to 9.83 m s^{-2}) and density, respectively. The WKB factor $\{N(z, t)/N_0\}^{-1/2}$ is less (greater) than unity when and where stratification is stronger (weaker) than the reference (Figures. 2.2b and 2.2c). In this study, five

events (Events 1–5) were defined as periods when the 3-day low-passed, WKB-scaled kinetic energy averaged over five depths of 53, 101, 153, 200, and 360 m exceeds 1.0 J m^{-3} (Table 2.1). The linear sum of the kinetic energies of NIWs and SDITs ($\text{KE}_{\text{NIW}} + \text{KE}_{\text{SDIT}}$), and their nonlinear interaction ($\text{KE}_{\text{NIW+SDIT}}$), were calculated from KE_{NIW} and KE_{SDIT} , as were the kinetic energies at wave-wave interaction frequencies including higher tidal harmonics within CFW range, such as $M_2 + f$ (see Table 2.2). Each frequency component was defined with cut-off frequencies within 5%, e.g., $[0.95(M_2 + f), 1.05(M_2 + f)]$, and only components that do not overlap each other were selected to calculate the $\text{KE}_{\text{NIW+SDIT}}$. The $\text{KE}_{\text{NIW_harmonics}}$ were calculated from harmonics of NIWs ($2f$, $3f$, and $4f$) after de-tide. The uTide Matlab toolbox (<http://www.po.gso.uri.edu/~codiga/utide/utide.htm>) were used for de-tide. The $\text{KE}_{\text{NIW}} + \text{KE}_{\text{SDIT}}$, $\text{KE}_{\text{NIW+SDIT}}$, $\text{KE}_{\text{NIW_harmonics}}$ and KE_{CFW} were all 40-hour low-pass filtered to compute the correlation (Table 2.3).

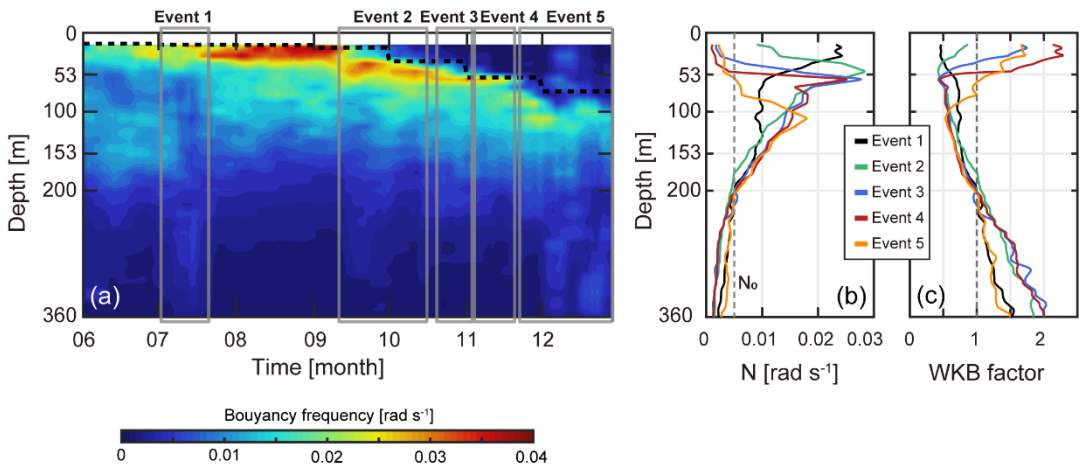


Figure 2.2. (a) Time-depth contour of Buoyance frequency N derived using Lim et al. (2012). Vertical profiles of (b) buoyance frequency and (c) WKB factor for Events (color) in 2003.

Table 2.1. Periods of internal wave events identified by 3-day low-passed, WKB-scaled CFW kinetic energy (KE_{CFW}) observed at the EC1 in 2003.

Event Number	Period (Month/Day in 2003)
1	July 2 – July 21
2	September 11 – October 16
3	October 20 – November 3
4	November 4 – November 20
5	November 22 – December 31

Table 2.2. Selected wave-wave interaction frequencies used to reconstruct $KE_{NIW+SDIT}$.

	Frequency	Period (hour)
$2f$	$2.00f$	9.89
M_2+f	$2.60f$	7.62
$3f$	$3.00f$	6.60
M_4	$3.19f$	6.21
M_3+f	$3.39f$	5.84
$2f+M_2$	$3.60f$	5.50
$4f$	$4.00f$	4.95
$3f+M_2$	$4.60f$	4.31
$2f+M_4$	$5.19f$	3.82
$3f+M_4$	$6.19f$	3.20

Table 2.3. Correlation coefficients between KE_{CFW} and KE_{NIW}+KE_{SDIT} (top), KE_{CFW} and KE_{NIW+SDIT} (middle), and KE_{NIW}+KE_{SDIT} and KE_{NIW+SDIT} (bottom). Coefficients where p<0.05 are underlined.

	Depth	Event 1	Event 2	Event 3	Event 4	Event 5	Total
KE _{CFW}	53 m	<u>0.47</u>	<u>0.30</u>	<u>0.37</u>	-0.05	<u>0.25</u>	<u>0.31</u>
	77 m	<u>0.88</u>	<u>0.43</u>	<u>0.32</u>	<u>0.21</u>	-0.18	<u>0.41</u>
	vs.	153 m	0.06	<u>0.18</u>	-0.09	<u>0.73</u>	<u>0.22</u>
	KE _{NIW} +KE _{SDIT}	200 m	<u>0.80</u>	-0.04	<u>0.35</u>	<u>0.64</u>	<u>0.31</u>
		360 m	-0.38	<u>0.65</u>	<u>0.66</u>	-0.12	<u>0.28</u>
							<u>0.54</u>
KE _{CFW}	53 m	<u>0.65</u>	<u>0.93</u>	<u>0.62</u>	<u>0.79</u>	<u>0.42</u>	<u>0.74</u>
	77 m	<u>0.92</u>	<u>0.84</u>	<u>0.78</u>	-0.01	<u>0.69</u>	<u>0.83</u>
	vs.	153 m	<u>0.74</u>	<u>0.78</u>	<u>0.82</u>	<u>0.66</u>	<u>0.76</u>
	KE _{NIW+SDIT}	200 m	<u>0.85</u>	<u>0.80</u>	<u>0.78</u>	<u>0.82</u>	<u>0.84</u>
		360 m	<u>0.79</u>	<u>0.78</u>	<u>0.85</u>	<u>0.70</u>	<u>0.83</u>
							<u>0.87</u>
KE _{NIW} +KE _{SDIT}	53 m	<u>0.74</u>	<u>0.34</u>	<u>0.77</u>	-0.19	<u>0.16</u>	<u>0.36</u>
	77 m	<u>0.93</u>	<u>0.35</u>	<u>0.52</u>	<u>0.52</u>	-0.19	<u>0.47</u>
	vs.	153 m	-0.03	<u>0.09</u>	-0.27	<u>0.67</u>	<u>0.14</u>
	KE _{NIW+SDIT}	200 m	<u>0.92</u>	<u>0.11</u>	<u>0.53</u>	<u>0.79</u>	<u>0.60</u>
		360 m	-0.41	<u>0.87</u>	<u>0.77</u>	0.06	<u>0.50</u>
							<u>0.57</u>
KE _{CFW}	53 m	<u>0.42</u>	<u>0.79</u>	<u>0.47</u>	<u>0.58</u>	<u>0.16</u>	<u>0.57</u>
	77 m	<u>0.51</u>	<u>0.69</u>	<u>0.34</u>	-0.16	<u>0.36</u>	<u>0.51</u>
	vs.	153 m	<u>0.36</u>	<u>0.66</u>	<u>0.46</u>	<u>0.44</u>	<u>0.33</u>
	KE _{NIW} _harmonics	200 m	<u>0.57</u>	<u>0.63</u>	<u>0.47</u>	<u>0.53</u>	<u>0.30</u>
		360 m	<u>0.50</u>	<u>0.49</u>	<u>0.64</u>	<u>0.24</u>	<u>0.45</u>
							<u>0.71</u>

To examine wind and current resonance at near-inertial frequency, the rate of wind work was calculated as (Jeon et al., 2019)

$$\tau_{x_{NIW}} u_{NIW_{53m}} + \tau_{y_{NIW}} v_{NIW_{53m}}$$

where $(\tau_{x_{NIW}}, \tau_{y_{NIW}})$ and $(u_{NIW_{53m}}, v_{NIW_{53m}})$ were near-inertial band-passed, zonal and meridional wind stresses at location nearest to the EC1 and averaged over the area shown in Figure. 2.1, and zonal and meridional current observed at 53 m, respectively.

To examine the inertial response of the mixed layer to surface wind forcing, a damped slab model was used (Pollard and Millard, 1970; D'Asaro, 1985):

$$\begin{aligned}\frac{\partial u_{ML}}{\partial t} &= f v_{ML} + \frac{\tau_x}{\rho_0 H_{ML}} - r u_{ML}, \\ \frac{\partial v_{ML}}{\partial t} &= -f u_{ML} + \frac{\tau_y}{\rho_0 H_{ML}} - r v_{ML}\end{aligned}$$

where H_{ML} , r and (u_{ML}, v_{ML}) are the MLD, inverse damping time scale, and zonal and meridional currents in the mixed layer, respectively. To test the sensitivity of the slab model results to H_{ML} and r , applications with four different cases were compared (Cases 1–4). The MLD was fixed to 20 and 60 m for Cases 1 and 2 (e.g., $H_{ML} = 20, 60$), respectively, whereas time-varying MLD was used for Cases 3 and 4 based on the observations (Lim et al., 2012). The damping time scale r^{-1} was set to 3 days for Cases 1, 2, and 4, and 6 days for Case 3 based on previous works (Kim et al., 2005; Nam, 2006; Nam and Park, 2013; Jeon et al., 2019). Among the modelled results, the modelled amplitudes of NIWs with time-varying H_{ML} (Cases 3

and 4) were more similar to the observed amplitudes at 53 m than those with constant H_{ML} (Cases 1 and 2). While the modelled amplitudes of NIWs are sensitive to both MLD and damping time scale, the timing of enhanced NIWs is consistent among the cases.

Since the mixed layer NIWs can be amplified by the energy transfer from mesoscale flow fields (Whitt and Thomas, 2015; Jing et al., 2017), a modified slab model as below incorporating background geostrophic currents, $\vec{U} = (U, V)$ was used to compare the order of magnitude of the advection terms (second and third terms in the left-hand-side) with other terms:

$$\begin{aligned}\frac{\partial u_{ML}}{\partial t} + u_{ML} \frac{\partial U}{\partial x} + v_{ML} \frac{\partial U}{\partial y} &= f v_{ML} + \frac{\tau_x}{\rho_0 H_{ML}} - r u_{ML}, \\ \frac{\partial v_{ML}}{\partial t} + u_{ML} \frac{\partial V}{\partial x} + v_{ML} \frac{\partial V}{\partial y} &= -f u_{ML} + \frac{\tau_y}{\rho_0 H_{ML}} - r v_{ML}\end{aligned}$$

Horizontal velocity gradient tensors were calculated from the satellite altimetry-derived surface geostrophic currents $\vec{U} = (U, V)$ where the normal and shear components of the rate of strain tensor, S_n and S_s , and vertical component of the relative vorticity, ζ were defined as:

$$\text{Normal strain: } S_n = \frac{\partial U}{\partial x} - \frac{\partial V}{\partial y};$$

$$\text{Shear strain: } S_s = \frac{\partial V}{\partial x} + \frac{\partial U}{\partial y};$$

$$\text{Relative vorticity: } \zeta = \frac{\partial V}{\partial x} - \frac{\partial U}{\partial y};$$

where the subscripts of U and V represented partial derivatives. Then, the relative importance of total strain and relative vorticity was diagnosed with the Okubo-Weiss parameter (Okubo, 1970), defined as $\alpha^2 = (S_n^2 + S_s^2 - \zeta^2)/4$. The efficiency of energy transfer from mesoscale field to NIWs (Jing et al., 2017) is proportional to total strain variance $\sqrt{(S_n^2 + S_s^2)}$ and inverse of the effective Coriolis frequency $f_{eff} = \sqrt{(f + \zeta/2)^2 - (S_n^2 + S_s^2)/4}$. The order of magnitude of total strain and relative vorticity ($O(10^{-5})$) derived from geostrophic currents was much larger than that of horizontal shear of the Ekman currents ($O(10^{-6}) \sim O(10^{-7})$) ($u_{Ekman} = \tau_y/f\rho_0, v_{Ekman} = -\tau_x/f\rho_0$) which derived from sea surface wind stress (Figure 2.3). Thus, the ageostrophic currents induced by wind was not considered as background flow fields in this study. The rate of energy transfer from the mesoscale field to NIWs was estimated following Jing et al. (2018), $P = -0.5(\langle uu \rangle - \langle vv \rangle)S_n - \langle uv \rangle S_s$, where the angle brackets $\langle \rangle$ represent the running mean over three inertial periods.

The characteristic slope of internal waves was calculated as (Baines, 1982):

$$\gamma = \pm \sqrt{(\omega^2 - f^2)/(N^2 - \omega^2)}$$

where wave frequency ω is set to M_2 to compare the characteristic slope of SDITs with the bottom slope at the shelf break in the north of the Korea Strait. Herein, the hydrographic data collected in the northern Korea Strait are used to estimate the time-varying buoyancy frequency.

The frequency spectrum of horizontal kinetic energy was fitted to $E_{fit}\omega^{S_{fit}}$ considering the conventional GM internal wave spectrum, where E_{fit} , S_{fit} , and ω

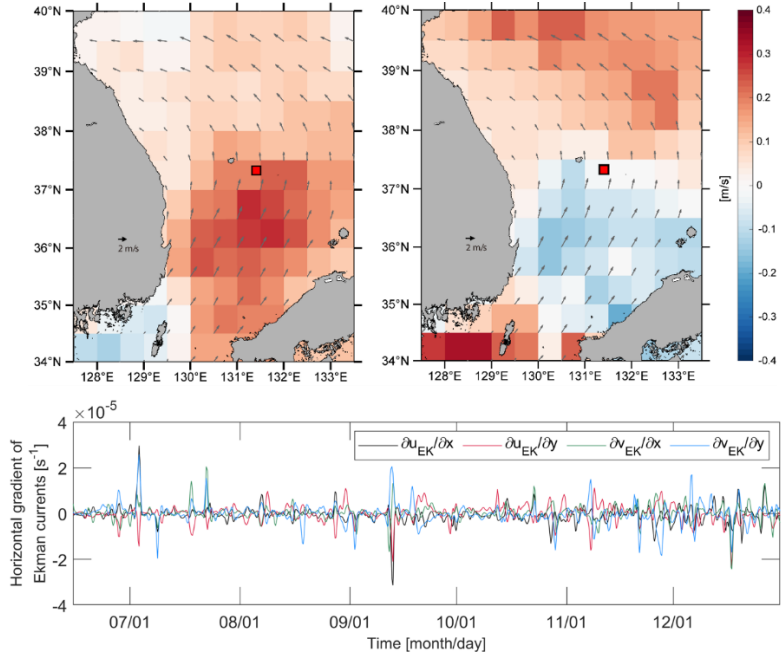


Figure 2.3. (Top) monthly mean Ekman currents (color) and wind (vector) in June 2003. Zonal and meridional Ekman currents were shown in left and right panel. The EC1 was marked by red square. (Bottom) Time-series of horizontal gradient of 40-hour low-passed Ekman currents

are fitted energy level, slope, and frequencies (Garrett and Kunze, 2007; Polzin and Lvov, 2011). To estimate temporal variations of the energy level E_{fit} and slope S_{fit} , a least-square fit of the spectrum for ranging from 0.09 cph and the Nyquist frequency (~ 0.5 cph) was applied to 20-day-long segment time series of horizontal kinetic energy at given depth. Deviations from the conventional GM internal wave spectrum ($S_{fit} = -2.0$) were used to quantify time-depth variations of CFWs. The E_{fit} or S_{fit} could be contaminated at folded frequencies by aliasing, since the Nyquist frequency (0.5 cph) was lower than the Buoyancy frequency (Figures 2.2 and 2.4). The higher buoyancy frequency, the more internal waves could exist, so the mean buoyancy frequency for each depth during the Events was considered.

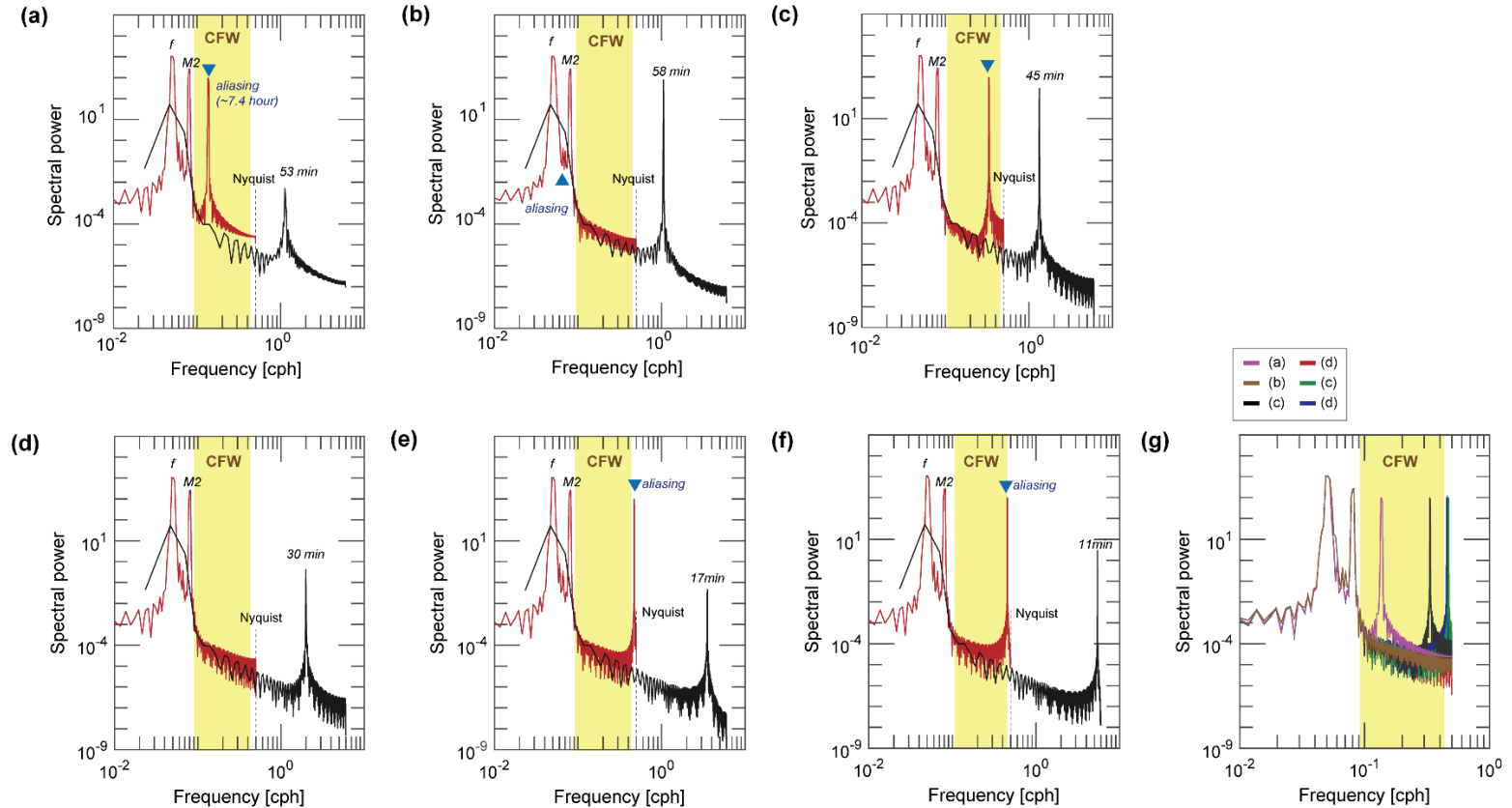


Figure 2.4. Aliasing sensitivity test for CFW band. Sample time series were made of inertial, semidiurnal, and buoyancy frequencies and their sampling period was set to 5 minutes (black lines in (a) – (f)). Hourly subsampled FFT was plotted by red color. All spectrum of subsampled time series is shown in (g).

2.3. Results

2.3.1. Temporal variations of enhanced internal wave energy

Five episodic CFW enhancements (Events 1–5) were observed along with those of NIWs or SDITs between 53 and 360 m at a subsurface mooring named EC1 located in the northern Ulleung Basin from July to December 2003 (Figure 2.1, and Table 2.1). NIW horizontal kinetic energy (KE_{NIW}) varies drastically with depth and time after removing stratification effects (see Figure 2.2) and yields different temporal and vertical structures during the events with the highest KE_{NIW} found during Event 2 (Figure 2.5a). In contrast to the NIWs intensified between 53 and 360 m during Events 1, 2, and 5, high KE_{NIW} was rarely observed between 100 and 200 m during Events 3 and 4. Temporal variations of SDIT kinetic energy (KE_{SDIT}) basically followed a noticeable fortnightly spring-neap tidal cycle (Figure 2.5b). However, vertical KE_{SDIT} structures significantly vary with time, yielding surface intensified features during Events 1 and 5 in contrast to spreading features during Events 2–4 and early Event 5. High KE_{SDIT} was rarely found below 153 m during Event 1 and between 53 and 360 m in August between Events 1 and 2. Not surprisingly, the time-depth pattern of CFW energy (KE_{CFW}) was generally similar to those of NIWs, SDITs, their summations ($KE_{NIW}+KE_{SDIT}$), and their interactions ($KE_{NIW+SDIT}$), including the energies at higher tidal harmonics as well as interaction frequencies (Figure 2.5).

High KE_{CFW} in Event 1 was found between 53 and 100 m, and 200 m where high KE_{NIW} or KE_{SDIT} were observed with significantly ($p < 0.05$) high correlation coefficients between KE_{CFW} and $KE_{NIW}+KE_{SDIT}$ and between KE_{CFW} and $KE_{NIW+SDIT}$ (Figures 2.5a–2.5d, and Table 2.3). The time-depth pattern of KE_{CFW} during Event 2

was generally more similar to those of KE_{NIW} than KE_{SDIT} , but it was complicated by the periods and depths where KE_{CFW} was high without enhanced NIWs or SDITs (green boxes in Figures 2.5c–2.5e). Conversely, CFWs at a depth between 53 and 100 m during the early part of Event 2 were not enhanced in spite of high KE_{NIW} (purple box in Figures 2.5c–2.5e). During Events 3–4, enhanced CFWs were accompanied by high KE_{NIW} , KE_{SDIT} , $KE_{NIW+KE_{SDIT}}$, and $KE_{NIW+SDIT}$, with significantly high correlations between KE_{CFW} and $KE_{NIW+KE_{SDIT}}$ except at 153 m for Event 3 and 53 and 360 m for Event 4. Significantly high correlations were also found between KE_{CFW} and $KE_{NIW+SDIT}$ except 77 m for Event 4. But high correlation between KE_{CFW} and $KE_{NIW_harmonics}$ at 360 m was only found in Event 3, not Event 4 (Figure 2.5, and Table 2.3). During Event 5, correlations were significant between KE_{CFW} and $KE_{NIW+KE_{SDIT}}$ and between KE_{CFW} and $KE_{NIW+SDIT}$ except 77 m, although the KE_{CFW} at 200 m was high on December 20 without enhanced NIWs or SDITs (green boxes in Figures 2.5c–2.5e). Since $KE_{NIW+KE_{SDIT}}$ is highly correlated with KE_{CFW} at all selected depths, there are events and depths where correlations between $KE_{NIW+KE_{SDIT}}$ and $KE_{NIW+SDIT}$ were also significant. However, the correlation between $KE_{NIW_harmonics}$ and KE_{CFW} at all selected depths was significantly low (Figures 2.5d–2.5e, and Table 2.3).

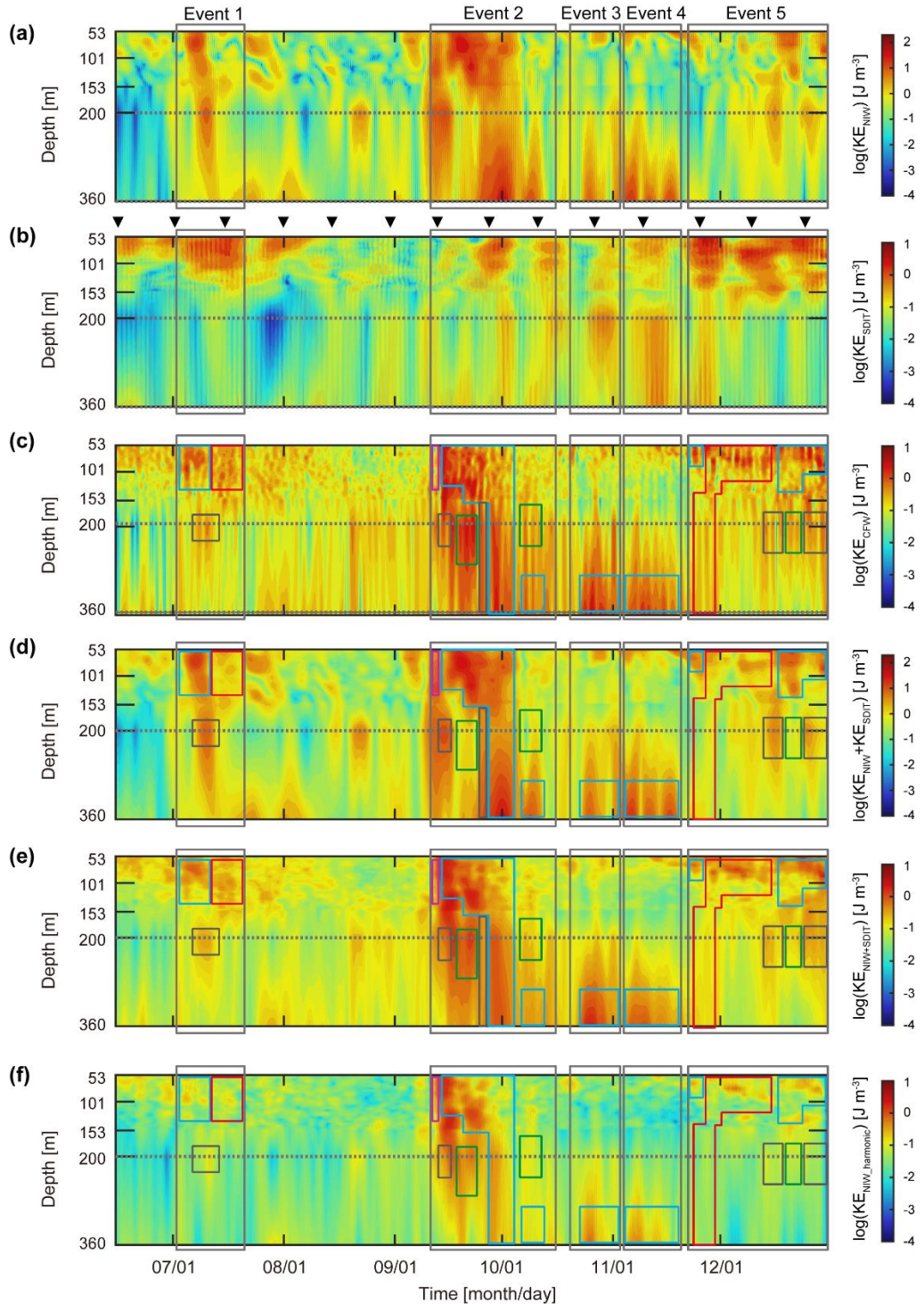


Figure 2.5. Time-depth contours of WKB-scaled (a) KE_{NIW} , (b) KE_{SDIT} , (c) KE_{CFW} , (d) $KE_{NIW}+KE_{SDIT}$, (e) $KE_{NIW+SDIT}$ and (f) $KE_{NIW, \text{harmonic}}$ are plotted, respectively. The KE_{CFW} , $KE_{NIW}+KE_{SDIT}$, and $KE_{NIW+SDIT}$ were 40-hour low-passed. Here, the $KE_{NIW}+KE_{SDIT}$ and

$KE_{NIW+SDIT}$ represent summation and interaction (see Table 2.1.) of NIWs and SDITs, respectively, whereas KE_{NIW} , KE_{SDIT} , and KE_{CFW} are directly estimated from NIWs, SDITs, and CFWs, respectively. $KE_{NIW_harmonics}$ represent summation of harmonics of NIW. Five events are denoted by grey boxes. Each color box in (a)–(f) represents enhanced NIWs only with no enhancements of SDITs or CFWs (purple), enhanced CFWs only with no enhancements of NIWs or SDITs (green), enhanced NIWs and CFWs with no SDIT enhancement (black), enhanced SDITs and CFWs with no NIW enhancement (red), and enhanced NIWs, SDITs, and CFWs (blue). Timings of spring tide at the nearby tide-gauge station (Ulleungdo) are denoted by triangles in (b).

2.3.2. Changes in horizontal kinetic energy spectra

The frequency spectra of horizontal kinetic energy at four depths consistently demonstrate temporal variations over the verticals of NIWs, SDITs, and CFWs during the five events (Figures 2.5a–2.5e). Spectral peaks at near-inertial (f) and SD (M_2) frequencies and their interaction frequencies (e.g., M_2+f , see Table 2.1) were significant. The spectral energy of the broad near-inertial peak decreased with depth during Event 1, whereas narrower near-inertial peaks had nearly the same spectral energy over depths during Event 2 (Figures 2.5a and 2.5b). During Events 3 and 4, much broader near-inertial peaks were found with maximum spectral energy at 360 m (Figures 2.5c and 2.5d). Two spectral peaks at near-inertial and SD frequencies with higher spectral energy at the upper depths found during Event 5 are similar to those during Event 1 (Figures 2.5a and 2.5e).

In these spectra, higher energies at the continuum frequency band were found at deeper depths during Events 3 and 4 but at shallower depths during Events 1, 2, and 5, which is consistent with the time-depth patterns of KE_{CFW} (Figures 2.5c and 2.6a–2.6e). The spectral energies integrated over the continuum frequency band were 2.13×10^{-4} and $1.14 \times 10^{-4} \text{ m}^2 \text{ s}^{-2}$ (corresponding to ~ 0.96 and 0.76 J m^{-3} of KE_{CFW}) at 360 m during Events 3 and 4, and 3.74×10^{-5} , 2.50×10^{-5} , and $4.94 \times 10^{-5} \text{ m}^2 \text{ s}^{-2}$ (corresponding to ~ 0.35 , 0.34 , and 0.51 J m^{-3} of KE_{CFW}) at 77 m during Events 1, 2, and 5, respectively. Considering the bandwidth between Nyquist frequency and buoyancy frequency (12.6 cph) at 360 during the Event 3, the increased spectral energies at 360 m than that at 200 m needed 0.06 J m^{-3} in higher frequency band. However, this was not taken into account because aliasing cannot raise the overall energy of the CFW band. Spectral slopes at 360 m during the periods

of high KE_{CFW} (spectral energy higher than $7 \times 10^{-5} \text{ m}^2 \text{ s}^{-2} \text{ cph}^{-1}$) were more gentle than the conventional GM spectral slope of -2.00, yielding -1.75, -1.80, -1.86, and -1.40 during late Event 2, Events 3–4, and early Event 5, respectively, while those at 77 m during Events 1, 2, and 5 (-2.27, -2.50, and -2.33) were steeper than the GM spectral slope (Figures 2.5 and 2.6e). However, During Events 3 and 4, spectral peaks at M_2+f frequency were also significant at 360 m though not significant at 95% confidence interval (Figures 2.6c and 2.6d). Here, In Event 3, the spectral slope at 360 m suddenly became gentler with the spectral peak at 0.45 cph, which might be came from aliasing. If there were internal waves with 0.55 or 1.95 cph, it could contaminate the spectral peak at 0.45 cph.

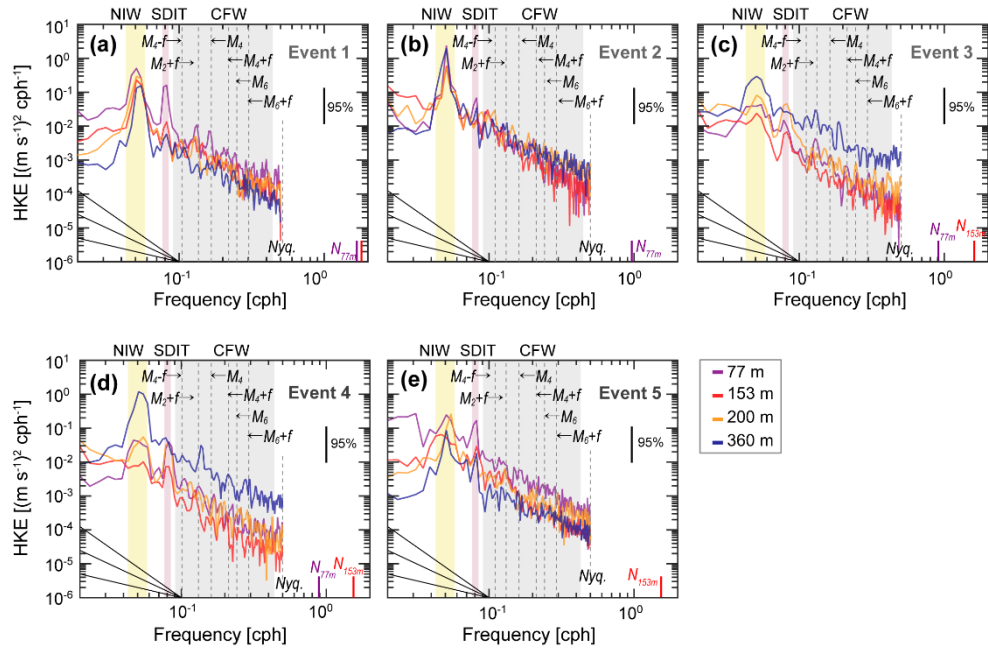


Figure 2.6. Frequency spectra of horizontal kinetic energy observed at 77 m (purple), 153 m (red), 200 m (orange), and 360 m (blue) during (a) Event 1, (b) Event 2, (c) Event 3, (d) Event 4, and (e) Event 5, respectively. Diagonal lines in bottom-left corners show fall-off rates or spectral slopes of -1, -2, and -3. Three internal wave bands of NIW (yellow), SDIT (red), and CFW (grey) are shaded with colors. Colored solid lines in right-bottom corners show mean buoyancy frequencies during the Events. The buoyancy frequencies of 200 and 360 m were much higher than sampling frequency (1cph).

2.4. Discussion

2.4.1. NIW generation by local wind forcing

Although a simple wind-forced, damped slab model cannot guarantee reproduction of all observed NIWs of surface wind origin, it is useful to identify the episodes of enhanced mixed layer NIWs, e.g., NIWs observed at 53 m (Figure 2.5c). Here, the model was not used to reproduce realistic kinetic energy nor its temporal structure but only to identify the events. In particular, it is obvious that the NIWs observed at the upper depths during early Event 2 were triggered by strong wind stress fluctuations (peaked to 1.15 N m^{-2}) due to the passage of Typhoon Maemi nearby the observation site (Figures 2.1 and 2.7a). At that time, rate of wind work significantly fluctuated regardless of using local or regional (averaged over the area denoted with the blue rectangle) wind stress (Figure 2.7b). The NIWs generated during this particular event were reported by *Nam et al.* (2007), and most (88%) of mixed layer NIWs observed in the region from 1999 to 2004 were suggested to be of wind origin as well reproduced by the wind-forced slab model although the amplitude was systematically over-estimated (*Nam and Park*, 2013). Slab model applications with four different cases of input parameters along with the rate of wind work confirmed the surface wind-generated NIWs, at least, during Events 1, 2, and 5 (Figures 2.7a–2.7d). Note that the vertical direction of NIW energy propagation was downward (or upward phase propagation) based on the time-depth pattern of zonal components of near-inertial currents (Figure 2.8) during the Events, consistently indicative of surface energy source.

Since the mixed layer NIWs can be amplified by surface background flow field during the generation stage, as recently suggested by *Whitt and Thomas* (2015) and

Jing et al. (2017), a modified slab model incorporating the effect of background mesoscale flow into the simple model was used to identify the time at which this effect becomes significant. The advection terms in the modified slab model representing nonlinear interaction terms between NIWs and mesoscale flow at the observation site (EC1) were two orders of magnitude lower than the other terms for all events except Event 4. During Event 4, the total strain of surface mesoscale flow consistently increased at EC1 as anticyclonic UWE which existed during Event 3 was vague and EC1 was located between two cyclonic circulations (Figures 2.9 and 2.10). The fact that EC1 was located at the rim of the UWE can also be confirmed by the horizontal shear of density estimated by the thermal wind equation (Figure 2.11). The two cyclonic circulations were meandering branching of the EKWC. The southwestern cyclonic circulation separated from EKWC below the 35.5 °N and the northeastern cyclonic circulation separated from EKWC upper the 40 °N. The latter cyclonic circulation might be related to Dok Cold Eddy (Mitchell et al., 2005). Consistently, the efficiency of energy transfer from mesoscale field to NIWs increased during Event 4 (Figure 2.7e), supporting the possibility of mesoscale flow amplifying NIWs in spite of surface wind forcing similar to or weaker than those during Events 1, 2, and 5 (Figures 2.7a–2.7d).

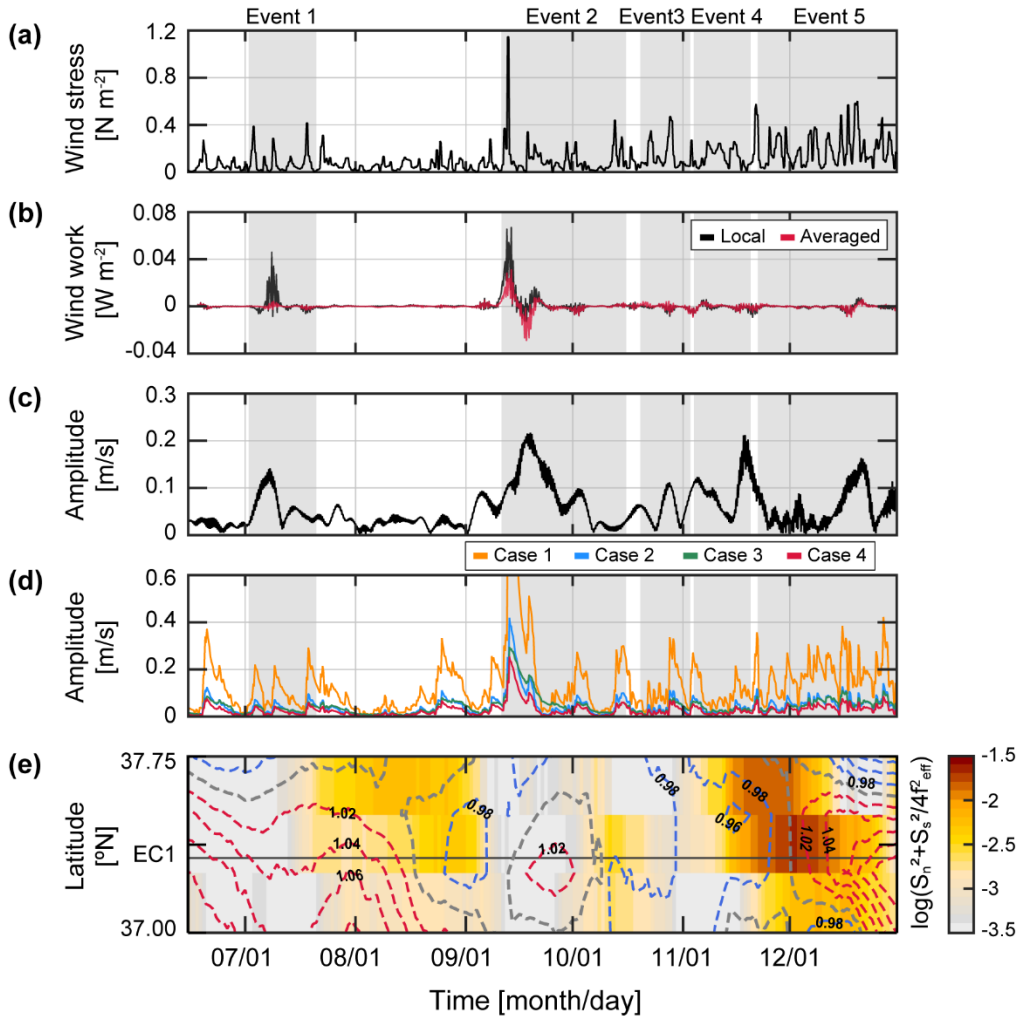


Figure 2.7. Time series of (a) wind stress in N m^{-2} averaged over the area shown in Fig. 2.1, (b) rate of work done by the surface wind at location nearest to EC1 (black) and averaged over the area (red) in W m^{-2} , (c) amplitude of NIWs observed at 53 m, (d) amplitude of NIWs calculated using the damped slab model for four cases. (e) Hovmöller diagram of the energy transfer efficiency in logged colour scale shown in the right at 131.43°E (longitude of EC1) as functions of time and latitude where dashed lines indicate the effective Coriolis frequency normalised by f at the surface (contour interval: $0.02f$).

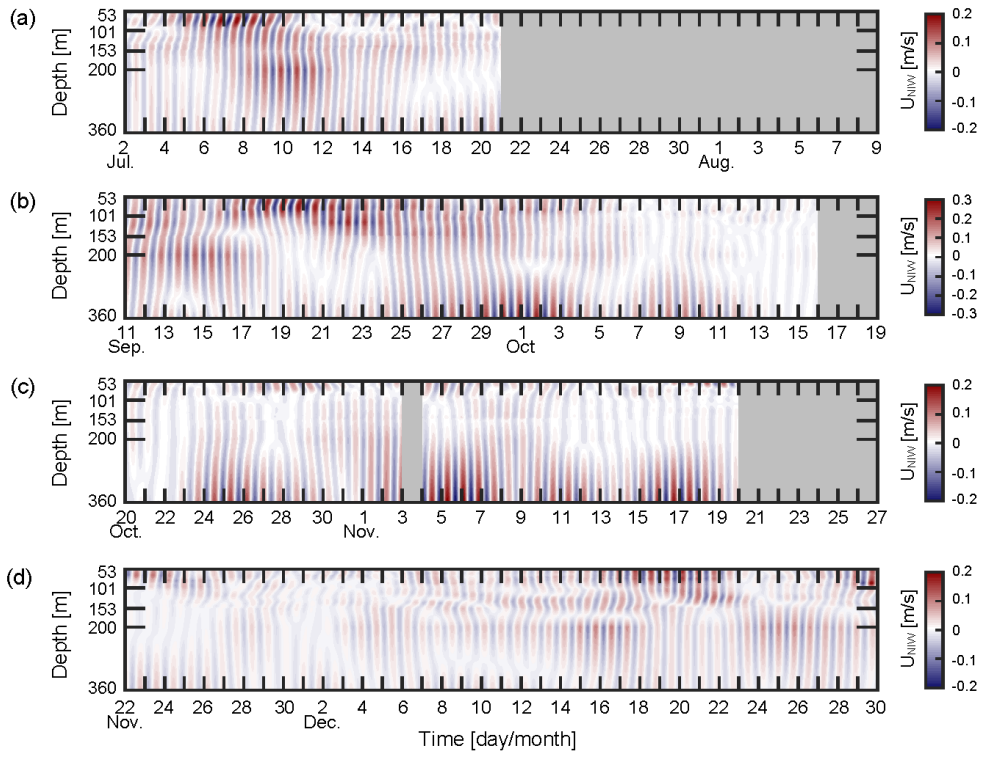


Figure 2.8. Time-depth contour of meridional component of NIW during (a) Event 1, (b) Event 2, (c) Event 3–4, and (d) Event 5.

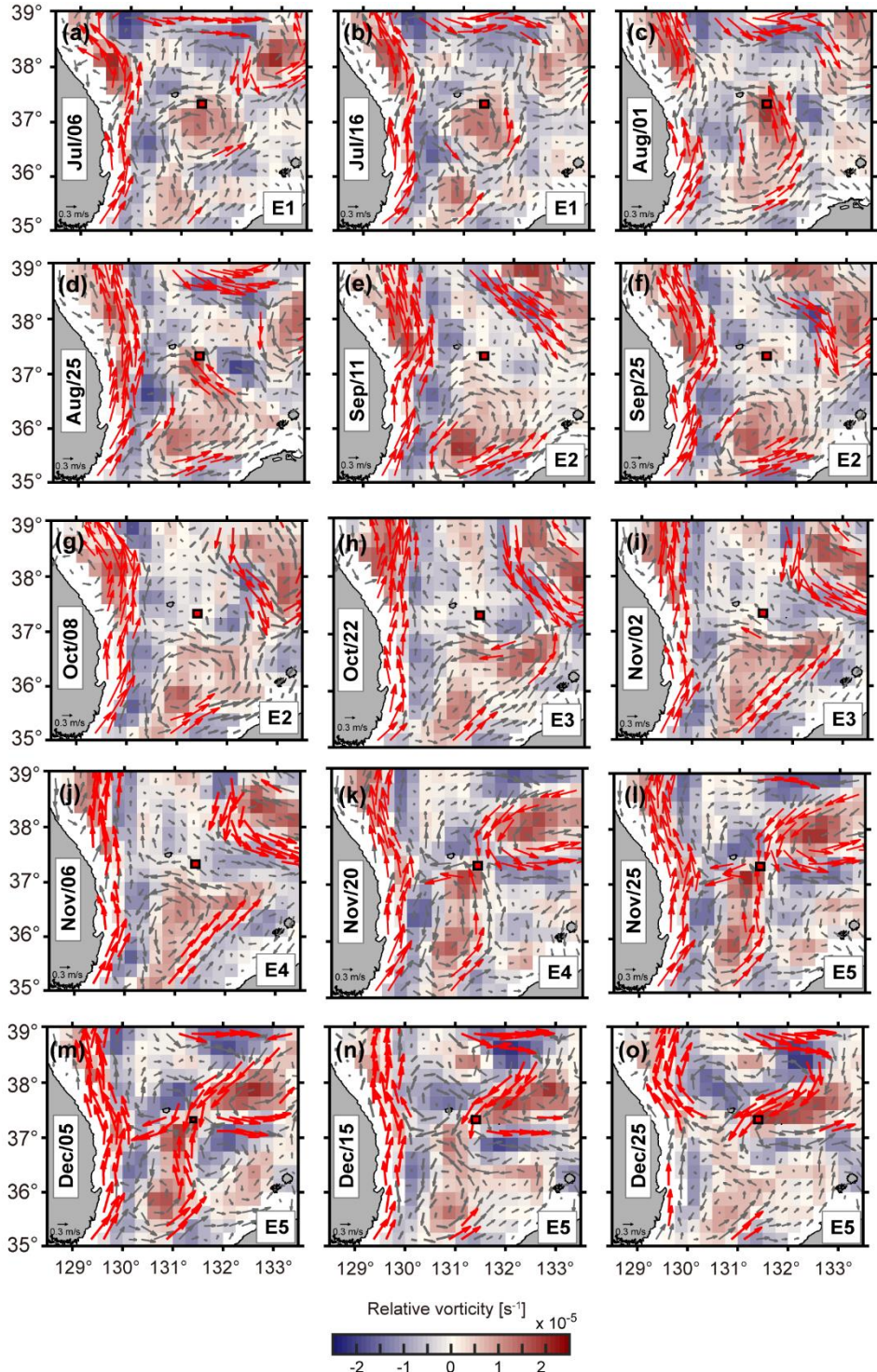


Figure 2.9. Maps of surface geostrophic currents derived from satellite altimetry (vectors) and vertical relative vorticity (color). (h) October 22 and (k) November 20 corresponding to early Event 3 and late Event 4, respectively. The EC1 location is demarcated by the red square. The geostrophic currents over the 0.3 m s^{-1} are shown in red arrows.

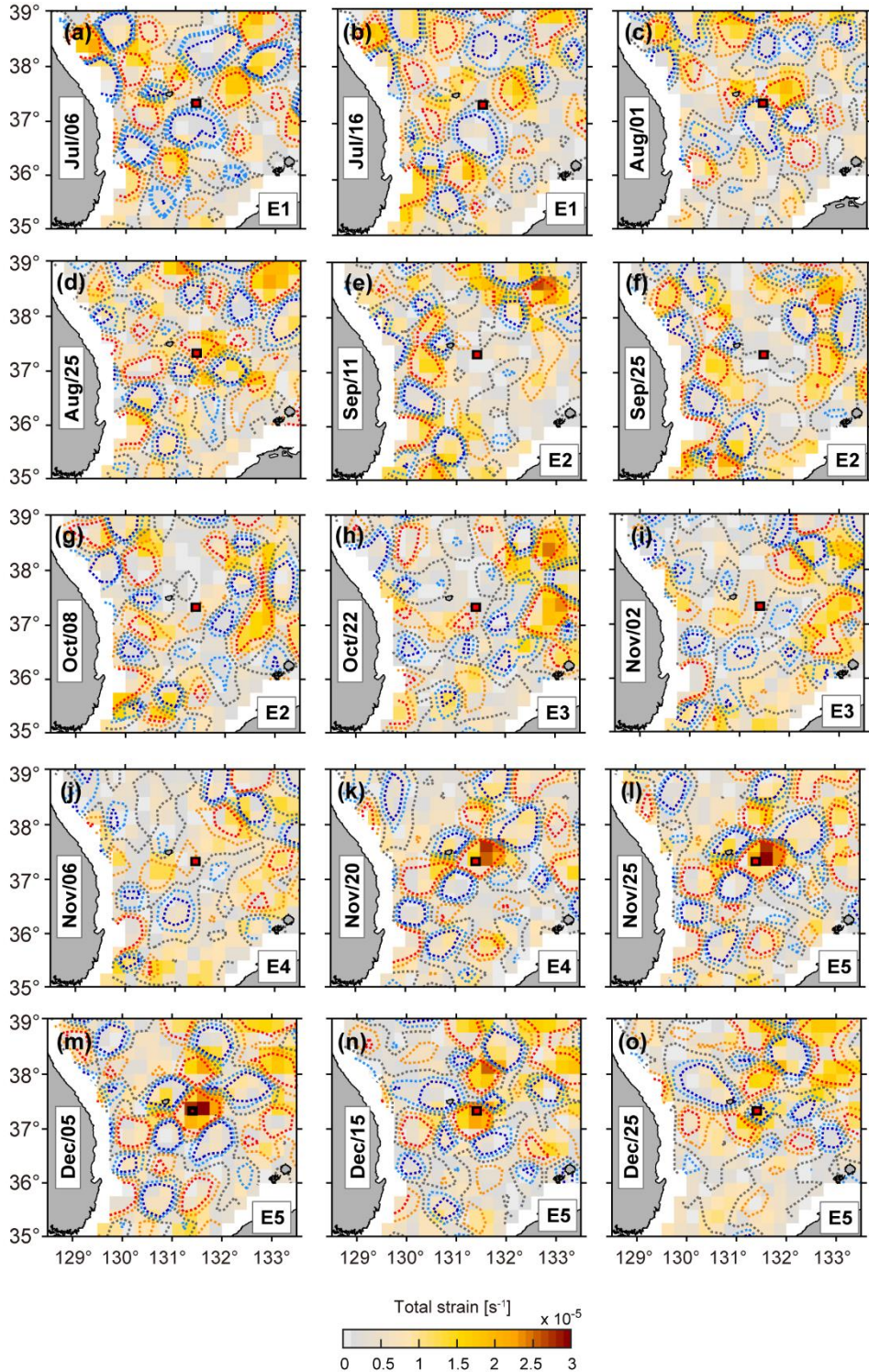


Figure 2.10. Maps total strain (colors) and Okubo-Weiss parameters α^2 (dotted contours) at -2×10^{-11} (blue), -1×10^{-11} (cyan), 0.0 (black), 1×10^{-11} (orange), and 2×10^{-11} (red). (h) October 22 and (k) November 20 corresponding to early Event 3 and late Event 4, respectively. The EC1 location is demarcated by the red square.

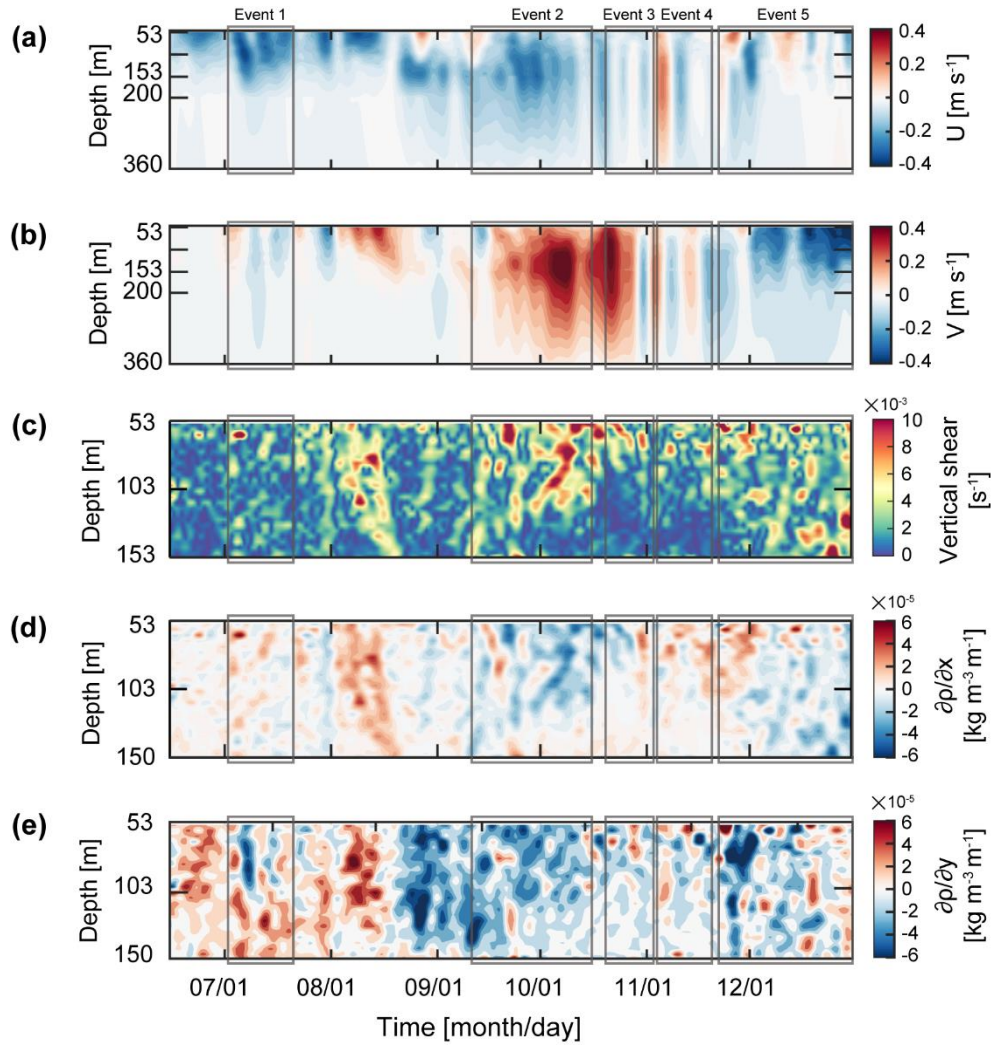


Figure 2.11. Time series of (a) 15-days low-passed subinertial zonal and (b) meridional currents. The absolute vertical shear of (a) and (b) are shown in (c). The horizontal shear of density estimated from thermal wind are shown in (d) and (e).

2.4.2. Interaction between mesoscale flow field and NIWs

The KE_{NIW} observed at 360 m of EC1 during Events 3–4 exhibited significantly higher near-inertial spectral energy with a broader peak, implying a source of energy other than the local wind forcing (Figures 2.5a, 2.6c–2.6d, 2.7d–2.7e, and 2.12a). A Doppler shift by lateral mesoscale flow fields may cause the broadening of the inertial spectral peak (Le Boyer, 2020). During Events 3–4, mesoscale (subinertial) energy averaged over the depth abruptly decreased from 90 to ~ 5 J m⁻², and the total strain of mesoscale flow increased from 0.55×10^{-5} to 1.78×10^{-5} s⁻¹ (Figures 2.13a and 2.13b). These changes are mainly due to changes of the mesoscale fields (Figures 2.9– 2.10), e.g., the EC1 was located in the western side of the UWE at early Event 3 (October 22) yielding strong geostrophic flow at the location (Figure 2.9h) whereas it became located in the middle of mesoscale circulations raising the total strain during the Event 4 (Figures 2.9k and 2.9l). The enhanced total strain supports the possibility of efficiently transferring mesoscale or subinertial energy into NIWs as further evidenced below. Based on the wave capture process suggested previously (Bühler and McIntye, 2005; Polzin, 2008; Jing et al, 2018), the NIWs undergo the Doppler shift with wavenumber changing exponentially ($\sim e^{\pm\alpha t}$ where α^2 is an Okubo-Weiss parameter defined as the difference between total strain and relative vorticity of mesoscale flow field), and extract energy from the mesoscale field when and where the strain exceeds vorticity, e.g., $\alpha^2 > 0$. The vertical-to-horizontal wavenumber ratio of captured waves would not exceed the upper bound, $m/\sqrt{k^2 + l^2} = m/k_H \leq \sqrt{(dU/dz)^2 + (dV/dz)^2}/\alpha$, where m, k, l are vertical and horizontal wavenumber (Polzin, 2008). Events 3 and 4 correspond to the period favouring wave capture at EC1 according to the definition

of *Jing et al.* (2018), yielding a positive Okubo-Weiss parameter with positive rates of energy transfer of 3.2×10^{-9} and $1.1 \times 10^{-9} \text{ m}^2 \text{ s}^{-3}$, respectively (Figures 2.12a and 2.12c). If the KE_{NIW} during Events 3–4 is enhanced by the wave capture, a sudden change in this ratio may occur through the Doppler shift. Based on the observed vertical shear of subinertial currents and the Okubo-Weiss parameter during Events 3–4, the resultant upper bound of the vertical-to-horizontal wavenumber ratio were calculated to be 1303 (Event 3) and 49 (Event 4). Here, $\vec{U} = (U, V)$ at 53 m is set to $(0, 0.40) \text{ m s}^{-1}$ for Event 3, and to $(0, 0.04) \text{ m s}^{-1}$ for Event 4, with $\vec{U} = 0$ at 360 m such that the vertical shear $\sqrt{(dU/dz)^2 + (dV/dz)^2}$ varies from $2.0 \times 10^{-3} \text{ s}^{-1}$ (Event 3) to $2.0 \times 10^{-4} \text{ s}^{-1}$ (Event 4), and $4\alpha^2$ varied from $9.0 \times 10^{-12} \text{ s}^{-2}$ (Event 3) to $6.4 \times 10^{-11} \text{ s}^{-2}$ (Event 4) (Figures 2.12a – c). The abrupt decrease of upper bound of wavenumber ratio implied the possibility of wave capture. Therefore, the NIWs enhanced at 360 m of EC1 during Events 3 and 4 can be explained by the wave capture, indicative of significant energy transfer from the mesoscale field to internal waves.

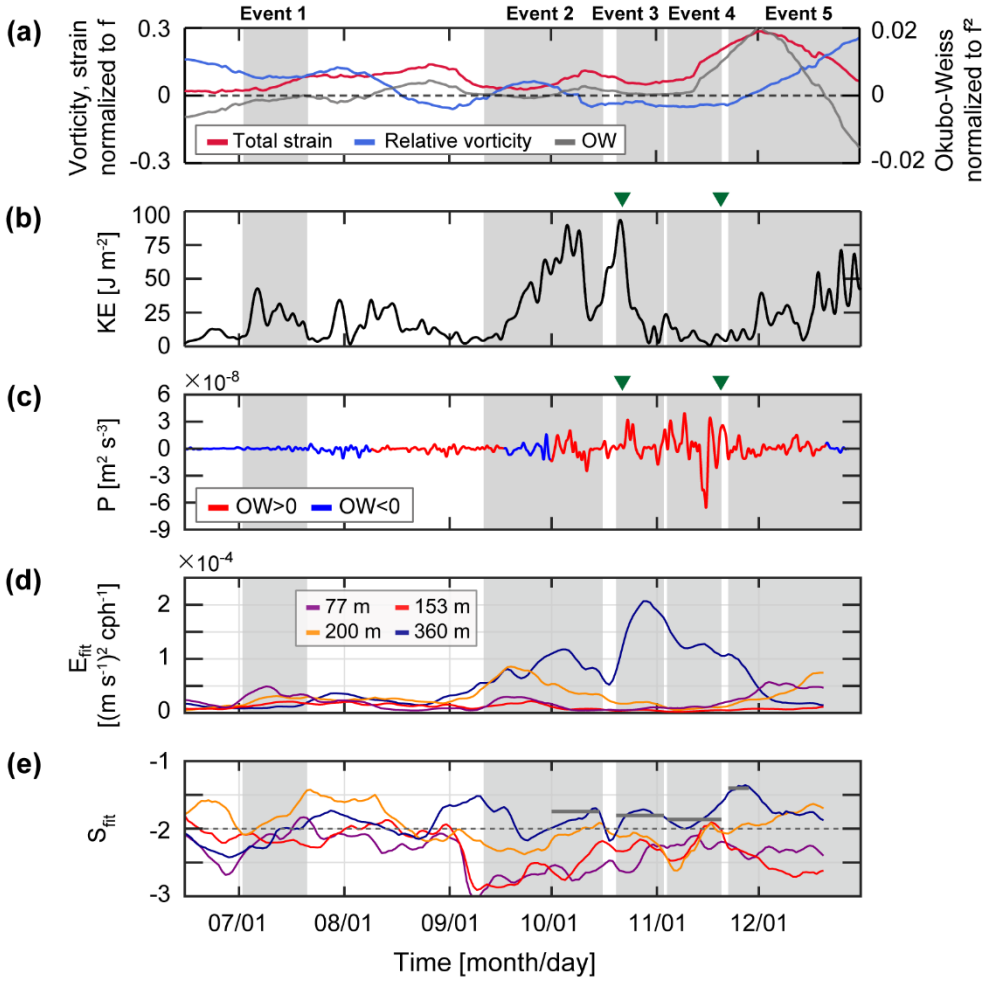


Figure 2.12. Time series of (a) total strain (red, left axis) and vertical relative vorticity (blue, left axis) normalized to f , and Okubo-Weiss parameter α^2 (thick grey, right axis) normalized to f^2 at the EC1 location. (b) Subinertial kinetic energy averaged from 53 to 360 m. (c) rate of energy transfer from mesoscale fields to internal waves. Red (blue) colour denotes positive (negative) Okubo-Weiss parameter α^2 . (d) Energy level (E_{fit}) and (e) slope (S_{fit}) fitted to observed frequency spectrum of horizontal kinetic energy shown in Fig. 2.2. Horizontal bars in (e) indicate the slope averaged over period when $E_{fit} > 7 \times 10^{-5} \text{ m}^2 \text{s}^{-2} \text{cph}^{-1}$ and $S_{fit} > -2$. Periods of five events are grey shaded in (a)–(e).

2.4.3. SDIT generation at the Korea Strait

Although EC1 is far (~ 200 km) from the generation area of ITs in the north of the Korea Strait (red hatched area in Figure 2.1), and diurnal ITs ($D1$) rarely propagate into the interior of the East Sea as $f > D1$, SDITs often propagate poleward freely as $f < M_2$. The poleward propagating SDITs can account for high KE_{SDIT} and spectral peaks at M_2 , as well as tidal subharmonic frequencies (Figures 2.5b and 2.6a–2.6e). Favorable periods for SDIT generation were found considering the bottom slope and buoyancy frequency at the shelf break in the generation region (corresponding depth of ~ 200 m) (Park and Watts, 2006). The internal wave characteristics slope is well matched to the bottom slope in August (between Events 1 and 2) and October (between Events 2 and 3), with buoyancy frequencies of 0.62 and 0.33 cph. On the other hand, the SDITs were weakly generated in June (before Event 1) and December (late Event 5) as the characteristic slope of 0.34–0.90 did not match well to the bottom slope with buoyancy frequencies of 0.04 and 0.20 cph. The summer–fall maximum and spring minimum of the barotropic-to-baroclinic conversion rate of SDITs in the area were consistent with recent numerical results presented by *Jeon et al.* (2014). The generated SDITs reached the EC1 within ~ 2.5 days, assuming the horizontal speed of mode-1 SDIT (~ 1 m s $^{-1}$) (Park and Watts, 2006) in September–November, but not in June, August, and December (as further discussed below). It is reasonable to account for the enhanced KE_{SDIT} and spectral peaks at M_2 and the tidal subharmonic frequencies, particularly below 153 m with poleward propagating SDITs. Although there were general enhancements of KE_{SDIT} following the spring-neap tidal cycle and enhancements of KE_{SDIT} above 153 m, regardless of conditions, for the generation and refraction of SDITs, the KE_{SDIT}

below 153 m is affected by the generation of SDITs modulated by the stratification conditions in the northern Korea Strait.

2.4.4. Interaction between mesoscale flow field and SDITs

Although SDITs were favourably generated in the northern Korea Strait both in August and October, those in August could not reach the EC1 except in October. The SDITs are refracted westward or eastward and are propagated poleward, or are trapped in the generation area, as the mesoscale fields act as a wave-guide (Park and Watts, 2006; Nam and Park, 2008). The eastward refraction of poleward propagating SDITs from the generation area into the EC1 is possible only when warmer water with higher sea surface height (SSH) occupies more of the western side than the eastern side of the Korea Strait, yielding faster propagation in the western than the eastern side (Figure 2.13). This condition was not satisfied before September when the observed SSH in the area was low, indicating that the cold water prevailed in the area to prohibit SDITs from propagating poleward out of the area, i.e., they were trapped in the area (Figure 2.14). During Events 2–4 and early Event 5 (September–November), the SSH in the western side became sufficiently high due to warmer water that allowed the eastward refraction of SDITs towards EC1 (Figure 2.14). Thus, high KE_{SDIT} and spectral peaks at M_2 and tidal subharmonic frequencies below 153 m during Events 2–4 and early Event 5 could be explained by remote SDITs (Figures 2.5b, 2.6b–2.6e, and 2.12e). In particular, SDITs generated at the northern Korea Strait are appropriate to explain the vertically spreading, beam-like KE_{SDIT} well. In contrast, the SDITs generated during August rarely propagate into the EC1 but are trapped within the generation area as relatively cold water (having low SSH) prevails, accounting for the low KE_{SDIT} observed below 153 m of EC1 during Event 1 and between Events 1 and 2 (Figures. 2.5b and 2.14). Nevertheless, the KE_{SDIT} observed above 153 m during same periods was still high, possibly due to long-range

propagating low-mode baroclinic (rather than beam-like) SDITs.

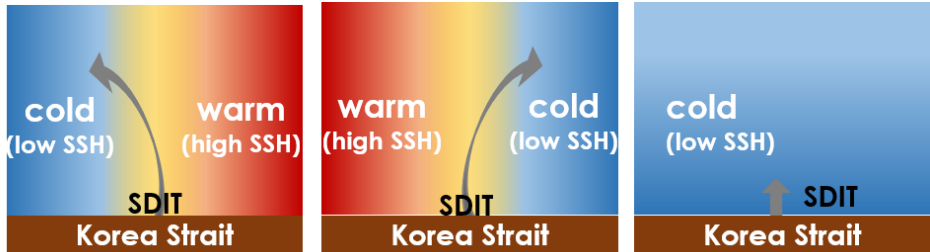


Figure 2.13. Schematics of SDIT propagation from the generation site (the northern slope of the Korea Strait) following the background condition.

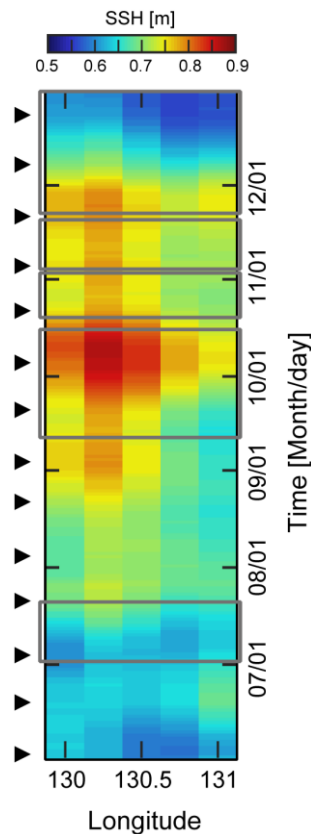


Figure 2.14. Hovmöller diagram (longitude and time plot) of the sea surface height (SSH) at the northern slope of the Korea Strait. Timings of spring tide at nearby tide-gauge station (Busan, not shown) are denoted by triangles.

2.4.5. CFW enhancement by interaction between NIWs and SDITs

There are three possible mechanisms for enhanced CFWs: one is forward cascading occurring directly from either one of the enhanced NIWs or SDITs; the second is from nonlinear interaction between NIWs and SDITs; and the third is local generation from the interaction between currents and bottom topography, e.g., Lee-waves. The Froude number, $F_r = U k_H / \omega$ (U : flow speed, k_H : horizontally dominant wavenumber of bottom topography, and ω : CFW frequency) was considered to examine the third possibility of Lee-wave generation. For a given weak tidal flow and a dominant bottom wavelength of ~ 7 km ($k_H = \sim 9.0 \times 10^{-4}$ cpm) in the vicinity of EC1 (within a degree), located in a relatively flat area (Figure 2.1), F_r was much smaller than unity. For this reason, the third possibility was ruled out. It is reasonable, considering the correlated time-depth patterns of KE_{NIW} , KE_{SDIT} , and KE_{CFW} , that the wave energy was forward cascaded into the CFWs when and where either NIWs or SDITs or both were enhanced (high $KE_{NIW} + KE_{SDIT}$ and $KE_{NIW+SDIT}$), supporting the first and second possibilities (Figure 2.5).

The two mechanisms are not simple, particularly considering the periods and depths where only NIWs were enhanced without enhancements of SDITs or CFWs (purple box in Figure 2.5) or where high KE_{CFW} was observed without enhanced NIWs or SDITs (green boxes in Figures 2.5c–2.5e). During Event 2, extreme high KE_{NIW} generated by the typhoon passage early on may propagate downward vertically, and presumably equatorward horizontally, as low-mode NIWs with a minimum energy loss into CFWs. A few days later, the CFWs enhanced via remote (rather than local) wave-wave interaction from high-mode NIWs were likely

observed in the single mooring without locally enhanced NIWs or SDITs. Note that KE_{NIW+SDIT} at 200 m remained high following high KE_{CFW} during the period when both KE_{NIW} and KE_{SDIT} (thus KE_{NIW+KE_{SDIT}}) were low (Figure 2.5), implying that wave-wave interaction processes were in action despite there being no local energy source (only remote).

The noticeable time-depth variations of the frequency spectrum of horizontal kinetic energy support different roles of multiple processes in facilitating energy transfer from NIWs and SDITs to CFWs, and potentially to turbulent mixing via forward energy cascading. Time series of energy level E_{fit} and slope S_{fit} of the frequency spectra over 20-day-segmented period demonstrates significant deviations from the conventional GM internal wave spectral slope ($S_{fit} = -2.0$), as previously recognized (Garrett and Munk, 1975; Polzin and Lvov, 2011). E_{fit} was remarkably high ($> 7 \times 10^{-5} \text{ m}^2 \text{ s}^{-2} \text{ cph}^{-1}$) at 360 m during late Event 2, Events 3–4, and early Event 5 presumably due to 1) downward propagating NIWs enhanced by local and regional wind forcing and interaction between NIWs and the mesoscale field, 2) eastward refraction of poleward propagation SDITs into EC1 from the generation area, and 3) enhanced CFWs by interaction between NIWs and SDITs. Significant interactions between NIWs and SDITs and among CFWs are also supported by low S_{fit} (less than -2.0, indicative of gentler spectral slope that deviates from the GM slope) during the entire observation period, except for Event 1 when KE_{SDIT} was low below 153 m (Figures 2.5b and 2.12d–2.12e).

2.5. Conclusion

In summary, this study is identified five episodic enhancements of CFWs observed from July to December 2003 in the southwestern East Sea, first time in the region, and discussed causes for the enhanced CFWs in relation to NIWs, SDITs, mesoscale fields, and their interactions. The findings are summarised as follows:

- 1) The local wind-forced, damped slab model well reproduced most of mixed layer NIWs supporting well-known mechanisms of surface generation and downward propagation of NIWs, particularly during typhoon passage (Event 2);
- 2) Modified slab model explained mixed layer NIWs even with weak wind forcing by considering the amplification due to interaction with the surface background flow field during the generation stage (Event 4);
- 3) Potentially evident and efficient energy transfer from mesoscale field to internal waves via wave capture accounted for enhanced NIWs at 360 m when the total strain exceeds relative vorticity and rates of energy transfer is positive (Events 3 and 4);
- 4) Remarkable time-depth variations of SDITs in addition to noticeable spring-neap tide cycles were found largely following mesoscale conditions favourable for generating the SDITs at the shelf break in the north of the Korea Strait and eastward refracting of the poleward propagating SDITs toward the observation site in the northern Ulleung Basin (Events 2–4 and early Event 5);
- 5) Importance of local and remote wave-wave interaction processes and forward energy cascading from NIWs and SDITs into CFWs was emphasised to account for time-depth patterns of KE_{CFW} and the frequency spectrum of horizontal kinetic energy, ruling out the possibility of bottom generation of local CFWs under the

condition of small Froude number.

The observations reveal that CFWs and forward energy cascading from low- to high-frequency internal waves are enhanced not only by direct local and remote wind forcing or by remote tidal forcing, but also through remarkable interactions among the internal waves, and with the mesoscale field via wave capture (Doppler shift of NIWs) and wave guide (refraction of SDITs). The results support previous works, which consistently show that 1) the NIWs are affected by mesoscale strain and vorticity (Kunze, 1985; Bühler and McIntyre, 2005; Polzin, 2008; Polzin, 2010; Byun et al., 2010; Elipot et al., 2010; Whitt and Thomas, 2015; Jing et al., 2017; Jing et al., 2018; Park and Watts, 2005; Jeon et al., 2019), 2) ITs are either refracted or trapped by the background fields (Park and Watts, 2006; Nam and Park, 2008; Jeon et al., 2014; Seo et al., 2016; Kim et al., 2005), and 3) NIWs and SDITs significantly interact to shape the CFWs via forward energy cascading (Alford, 2003; Ferrari and Wunsch, 2009; MacKinnon et al., 2017; Garrett and Munk, 1975; Hibiya et al., 2002; Alford et al., 2017). More and better observations are required to further deepen our understanding on how the internal waves extract energy from the mesoscale field and transfer the energy into a smaller scale and turbulence in the ocean.

3. NIWs of typhoon origin observed in 2015

3.1. Introduction

Near-inertial internal gravity waves (NIWs) having frequencies near the local inertial frequency, f , are ubiquitous in the stratified rotating ocean and the most energetic part of the oceanic internal wave field (Garrett, 2001; Ferrari and Wunsch, 2009). The NIWs are mainly generated by surface wind forcing, propagate into the ocean interior below the surface mixed layer and generally equatorward and ultimately dissipate enhancing turbulent mixing (Alford et al., 2016; MacKinnon et al., 2017; Whalen et al., 2020). The global ocean needs energy about 2.1 TW for sustaining the abyssal stratification (Munk and Wunsch, 1998), and the rate of work done by wind on NIWs is known as to range from 0.3 to 1.3 TW (Jiang et al., 2005). The NIW-driven mixing may sustain the meridional overturning circulation (Whalen et al., 2020), and the near-inertial variations of the meridional overturning circulation was revealed by numerical simulation (Blaker et al., 2011; Xiao et al., 2016). The NIWs also affect nutrient and carbon cycles that influence primary production, and marine ecosystem (Pan et al., 2012; Muacho et al., 2013; Villamana et al., 2017; Li et al., 2018; Song et al., 2019).

Strong tropical cyclones interacting with both the atmosphere and the upper ocean commonly produce energetic inertial oscillations in the mixed layer. The NIWs are efficiently generated when the sea surface wind stress changes with the passages of tropical cyclone such as typhoon. Regarding path of typhoon, it is known that the wind is strong and rotates clockwise with time for a fixed location on the right side of cyclone in the Northern Hemisphere, permitting the resonance between wind and NIWs (Price, 1981; Chen et al., 2015). Propagation of wind-induced NIWs

is affected by spatial variations of the effective Coriolis frequency, $f_{eff} = f + \frac{1}{2}\zeta$,

where ζ is relative vorticity induced by horizontal gradient of mesoscale flow fields.

The f_{eff} shifting the NIWs frequency amount $\frac{1}{2}\zeta$ can lead trapping or reflecting the NIWs (Kunze, 1985; Whitt and Thomas, 2015; Alford et al., 2016).

The typhoons frequently pass the East Sea in summertime providing strong wind stress that generates the NIWs. In numerical model, monthly-mean horizontal kinetic energies in the mixed layer during a typhoon passing was about 2.5–2.7 times larger than those during the summer without typhoon (Song et al., 2020). The wind in this region is known to be controlled by the East Asian Monsoon (Trusenkova et al., 2007). The NIWs have annual cycle with winter intensification depending on the seasonal variation of wind stress (Mori et al., 2005; Jeon et al., 2019). In summer, the East Asian monsoon onset starts in the South China Sea, where the tropical cyclones can trigger the onset of South China Sea Summer Monsoon (Yihui and Chan, 2005; Huagnfu et al., 2017). Although it is well known that ocean-atmosphere interactions in the South China Sea are related to summer precipitation in the East Asia (Jang and Yeh, 2013), the effect of changed wind fields in the South China Sea on the oceanic response in the East Sea has been rarely studied yet.

In the southwestern East Sea, energetic mesoscale eddies associated with strong mesoscale variability such as meandering of East Korea Warm Current are frequently generated and observed (Ichiye and Takano, 1988; Shin et al., 2005). The UWE provides favourable conditions for the NIW trapping in region of negative vorticity (Lee and Niiler, 1998; Park and Watts, 2005), or the NIW reflection within upper thermostad of UWE (Byun et al., 2010). In October 2014, a semi-permanent anticyclonic eddy, called the Ulleung warm Eddy (UWE), were generated and

persisted over the 2 years in the region, while it had no common feature on the pathways (Lee et al., 2019; Jin et al., 2019). Besides, other eddies smaller than the UWE were continuously created and existed. Although the f_{eff} was varied in space and time due to the evolution and propagation of mesoscale eddies, the interaction between NIWs and mesoscale eddies (especially UWE generated in 2014) was rarely studied.

This chapter examines the NIWs generated after typhoons in the East Sea or the South China Sea, and their amplification depending on favourable wind condition and interaction with UWE. Data and methods are described in the next chapter. In chapter 3.3, results of moored observations and damped slab model are presented. This chapter will discuss the results on enhanced NIWs in terms of surface wind forcing after typhoons and the UWE in chapter 3.4, and conclude in chapter 3.5.

3.2. Data and method

3.2.1. Data

A subsurface mooring was deployed at the site EC1 ($37^{\circ}19.94'N$, $131^{\circ}27.34'E$) in the Ulleung Interplain Gap from August 2014 to September 2015 (Figure 3.1). The mooring was equipped with three single-point acoustic current meters (Nortek Aquadopp) with temperature sensors at about 390, 1400, and 2200 m, and an upward-looking acoustic Doppler current profiler (ADCP, 300 kHz) at depth of ~120 m. The water temperature at 120 m and vertical profiles of horizontal currents at the upper 120 m were measured every 10 minutes with a depth interval (bin size) of 8 m (total 12 bins) using the ADCP. Temperature and currents obtained from the Aquadopps also measured every 10 minutes. However, there were no available data at 1400 m due to the corroded main board by battery leakage. All EC1 data from 1996 to 2020 are currently provided via SEANOE (Lee and Nam, 2021). In this study, the time-series data collected at the upper 120 m from March 15 to September 2 in 2015 were used.

Hydrographic data from the Met Office Hadley Center EN4.2.1. (hereafter EN4) data are used to estimate the mixed layer depth (MLD). The EN4 data are mainly based on World Ocean Database 2009, and their spatial and temporal resolution are 1 degree and monthly, respectively (Good et al., 2013). To supplement the moored observation, surface geostrophic currents calculated by satellite altimetry-derived sea surface height were examined. The gridded level-4 sea surface height data corresponding absolute dynamic topography above geoid provided by the Copernicus Marine Environment Monitoring Service were used at the horizontal and temporal resolutions of 0.25° and 1-day, respectively. Hourly sea surface wind

with a horizontal resolution of 30 km were used to calculate wind stress, $\vec{\tau} = (\tau_x, \tau_y)$. Hourly horizontal wind and geopotential height at 850 hPa were also used to determine the typhoon and atmospheric condition in the South China Sea and East Sea. These are available on the European Center for Medium-Range Weather Forecasts Reanalysis version 5 (ERA 5). The paths of the tropical cyclones are analysed using the TC best track data (v04r00) from the International Best Track Archive for Climate Stewardship (IBTrACS).

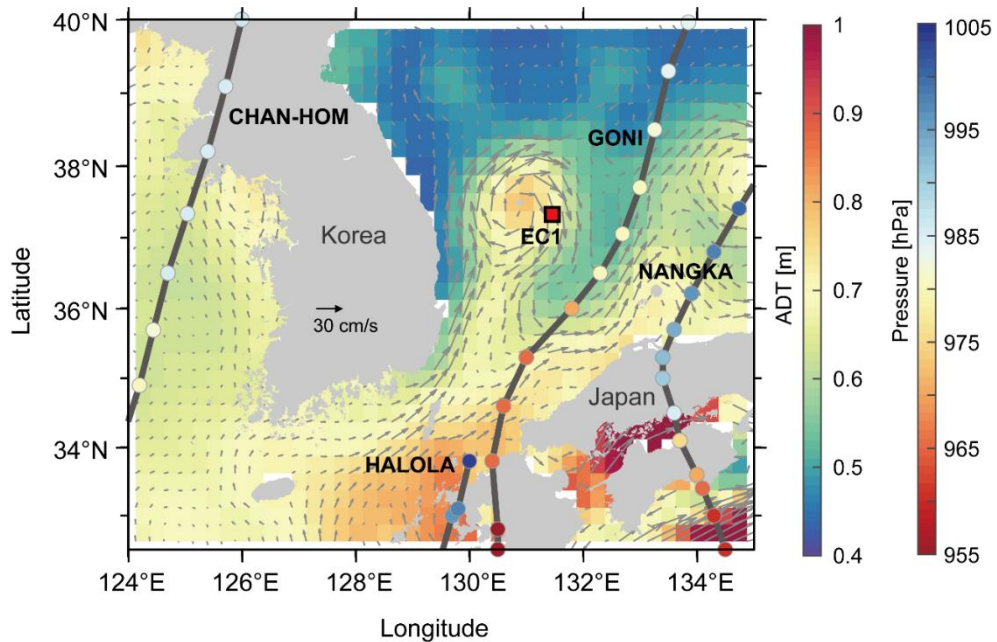


Figure 3.1. Track of typhoons with the central pressure (colored circles) superimposed on the absolute dynamic topography averaged from 15 March to 2 September 2015 (color shading) with the surface geostrophic currents (grey arrows). The EC1 is marked by red square.

3.2.2. Method

Zonal and meridional currents (u, v) observed at EC1 were quality controlled by following the global standard (IOOS, 2019; Min et al., 2020). Time-varying recorded depths due to the mooring tilting by drags of horizontal currents was corrected by vertical linear interpolation. Then, the zonal and meridional components of NIWs (u_{NIW}, v_{NIW}) were extracted from (u, v) applying phase-preserving fourth-order Butterworth bandpass filter with cut-off frequencies of $0.85f$ and $1.15f$ where f is about 0.0505 cph (cph: cycle per hour) corresponding period is 19.8 hour. The subinertial currents ($u_{subinertial}, v_{subinertial}$) were extracted applying 72-hour lowpass filter. The near-inertial amplitude and horizontal kinetic energy (KE_{NIW}) were computed as $\sqrt{u_{NIW}^2 + v_{NIW}^2}$ and $0.5\rho_0(u_{NIW}^2 + v_{NIW}^2)$ where ρ_0 is reference density ($=1025.0 \text{ kg m}^{-3}$). The NIW frequencies were extracted by applying complex demodulation to (u, v) (Thomson and Emery, 2014).

The MLD was defined as a depth where potential density (σ_θ) changed by given threshold criterion ($\Delta\sigma_\theta$) relative to that at a reference depth (de Boyer Montégut et al., 2004; Lim et al., 2012). The threshold was calculated from temperature change (ΔT) relative to that at the reference depth as below.

$$\Delta\sigma_\theta = \sigma_\theta(T_{ref} + \Delta T, S_{ref}, P_0) - \sigma_\theta(T_{ref}, S_{ref}, P_0)$$

Here, T_{ref} and S_{ref} are the temperature and salinity at the reference depth derived from the EN4 data at the nearest grid to the EC1, and P_0 is pressure at the sea surface (set to zero). The threshold and reference depth were set to $\Delta T = 0.2 \text{ }^\circ\text{C}$ and 10 m following to Lim et al. (2012). During the observation period, the mean

and standard deviation of MLD was 12.5 and 2.9 m, respectively. The maximum and minimum of 18.0 and 10.5 m were found in March and August.

Inertial response in the mixed layer to surface wind forcing was simply demonstrated using damped slab model (Pollard and Millard, 1970; D'Asaro, 1985) that was described in chapter 2.2. Here, the damping time scale r^{-1} was fixed to 4 days, and the time-varying MLD estimated from EN4 was used as H_{ML} .

The rate of work done by wind was calculated by inner product of surface wind stress and currents. Here, three cases of the rate of wind work Π were considered: (1)

$$\Pi_{slab_tot} = \tau_x u_{ML} + \tau_y v_{ML} , \quad (2) \quad \Pi_{slab_niw} = \tau_{x_{NIW}} u_{ML} + \tau_{y_{NIW}} v_{ML} , \quad \text{and}$$

$$(3) \quad \Pi_{obs_niw} = \tau_{x_{NIW}} u_{NIW} + \tau_{y_{NIW}} v_{NIW}.$$

The temporal variations of UWE were identified based on the satellite altimetry-derived sea surface height and surface geostrophic currents $\vec{U} = (U, V)$. The center and boundaries of mesoscale eddies were primarily detected and tracked by the sea surface height-based eddy detection method (Chelton et al., 2011; Faghmous et al., 2015), and were selected for the smaller ones than the Rhines scale at each latitude (Eden et al., 2007). This eddy tracking method was verified by in-situ hydrographic observations and details are provided by Lee et al., (2019). The Okubo-Weiss parameter, total strain, relative vorticity are same as in chapter 2.

3.3. Results

3.3.1. Wind forced periods

During the observation period, four energetic near-inertial wind stress ($> 0.05 \text{ N m}^{-2}$) events were found in April, May, June, and August in 2015 (Figures 3.1, and 3.2a–3.2c). The maximum amplitudes of wind stress during the events were 0.72, 0.46, 0.53, and 1.48 N m^{-2} , respectively. During Event 4, Typhoon GONI passed close to the right side of EC1 with translation speed of $\sim 5.7 \text{ m s}^{-1}$ providing the strongest wind stress, but in other events, strong wind stress ($> 0.4 \text{ N m}^{-2}$) appeared even though there was no typhoon. It was similar to or greater than those when typhoon CHAN-HOM, NANGKA, and HALOLA affected the East Sea in July (Figures 3.1, and 3.2a–3.2c). These three typhoons affected the wind fields near the EC1, sequentially increasing the wind stress from 11 to 14 by typhoon CHAN-HOM, from 15 to 17 by typhoon NANGKA, and from the 18 to 26 in July from by HALOLA (not shown). These typhoons landed in Korea and Japan, and then weakened with the central pressure over 1000 hPa. The wind stress amplitude increased during this period, but for some reason the near-inertial wind stress amplitude was less than 0.03 N m^{-2} . It was in contrast to an increase in near-inertial wind stress amplitude up to 0.15 N m^{-2} during Typhoon GONI.

High wind energy input during the events were identified in the rate of wind work and cumulative energy input to mixed layer from estimated wind energy flux (Figures 3.2c and 3.2d). Π_{slab_tot} (black line in Figure 3.2c) showed the greatest fluctuations, not only in the event periods but also in the typhoon passing in July, whereas Π_{slab_niw} (blue line in Figure 3.2c) increased in the event period not for the typhoon periods in July. It was consistent with the temporal variations of total and

near-inertial wind stress amplitude. During the events, the wind energy input increased (except the Event 4 with Π_{slab_tot}), and wind energy input due to near-inertial wind stress was about 40 % of the that from the total wind stress (Figure 3.2d). The amount of cumulative wind energy input with observed NIWs (Π_{obs_niw}) showed between Π_{slab_tot} and Π_{slab_niw} (Figure 3.2d). The Π_{obs_niw} during Event 1 was quite different from Π_{slab_tot} and Π_{slab_niw} showing decrease of wind energy input (Red in Figure 3.2c and 3.2d). Besides, there was no significant wind energy input with Π_{obs_niw} during the typhoon passing period in July.

Table 3.1. Event periods and typhoons related to the events

Events	Period in 2015	Related typhoon	
		In the East Sea	In the South China Sea
1	01 April – 07 April	-	MAYSAK
2	11 May – 18 May	-	NOUL
3	26 June – 3 July	-	KUJIRA
4	24 August – 1 September	GONI	-
-	12 July – 26 July	CHAN-HOM, NANGKA, HALOLA	

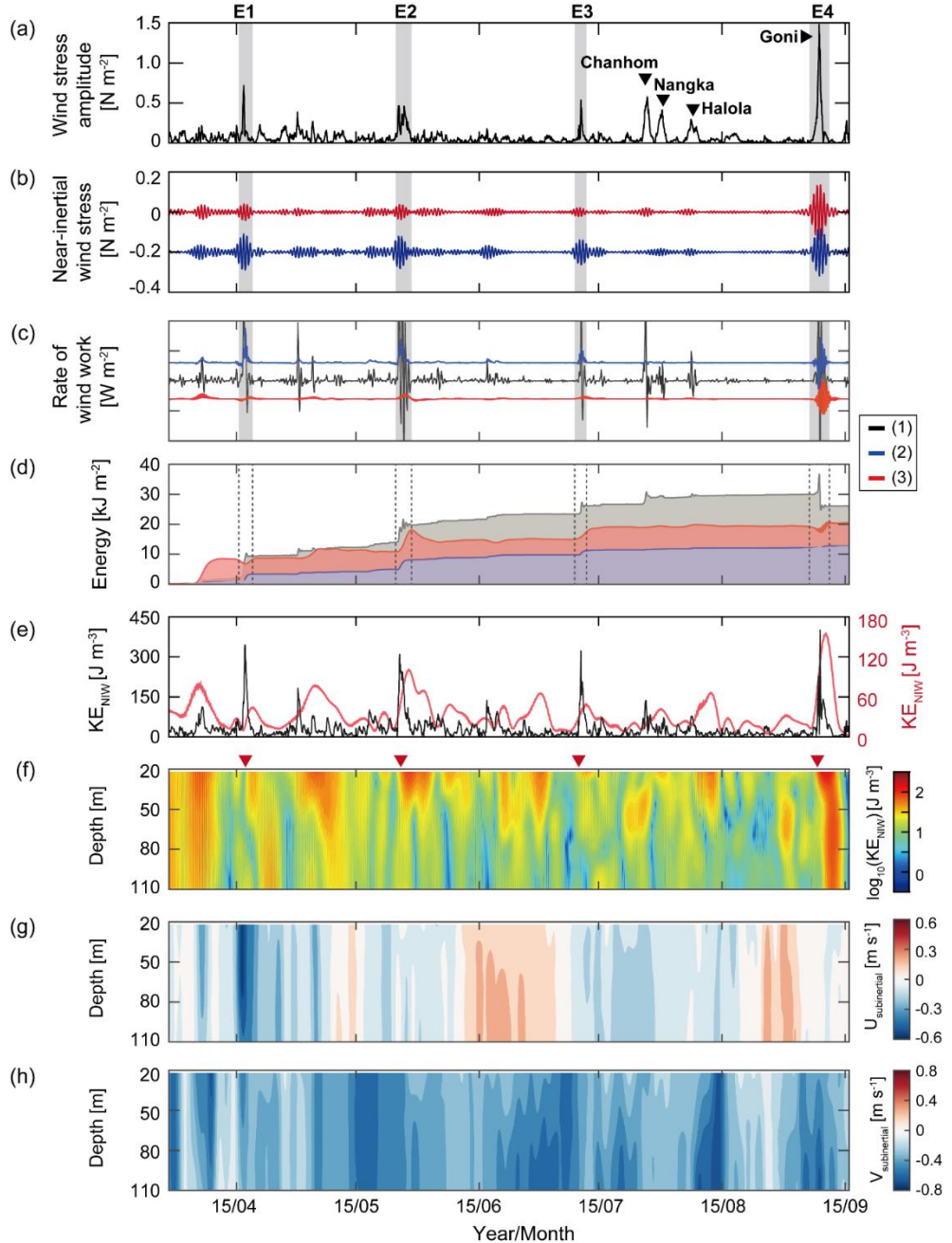


Figure 3.2. Time series of (a) wind stress amplitude $\sqrt{\tau_x^2 + \tau_y^2}$, (b) near-inertial wind stress, (c) rate of work done by wind, (d) temporal integral of (c), (e) KE_{NIW} estimated by damped slab model (black line, left y-axis) and observed at uppermost 22 m (red line, right y-axis). Time-depth contours of observed (f) KE_{NIW} in log scale, (g) zonal and (h) meridional components of subinertial currents. In (b), red and blue lines indicate τ_x and τ_y .

3.3.2. Temporal and vertical variations of observed NIWs

The increased KE_{NIW} was observed upper 110 m along with the near-inertial wind stress at the EC1, showing downward energy (upward phase) propagation (Figures 3.2a, 3.2f, and 3.3). The highest KE_{NIW} was found during Event 4, when the KE_{NIW} of the entire water column was amplified after typhoon GONI passing in 25 August (Figures 3.2e and 3.2f). At this period, the vertical phase propagation showed nearly in-phase (Figure 3.3d). In contrast to the Event 4, the KE_{NIW} during the Events 1–3 was smaller than that of Event 4, and it was almost limited to the upper 60 m. Here, the KE_{NIW} during the Events 1 and 3 was barely amplified. The KE_{NIW} after the typhoon passing in July was also amplified at 60 m above, but not as amplified as in Events 2 or 4. While the KE_{NIW} in the mixed layer reproduced by slab model was almost similar during the whole events, the observed KE_{NIW} was different for each event (Figures 3.2e and 3.2f).

Vertical structure of KE_{NIW} averaged over the events showed the NIW enhancement upper 60 m (Figure 3.4). The energetic KE_{NIW} over 60 J m^{-3} was found above 50 m in the Events 2 and 4, and the KE_{NIW} over the whole depths during Events 1 and 3 was smaller than 40 J m^{-2} , which was similar to that during the typhoons passing in July. The KE_{NIW} during the Event 3 was less than 20 J m^{-2} , except that at uppermost 22 m. The vertical structure of the NIW frequency also varied for each event. The NIW frequencies showed mostly blue shift over the depths when the wind stress near the EC1 increased directly due to the typhoon passing (e.g., Event 4 and July in 2015). In the Events 1 and 2, the NIW frequencies showed the red shift at depths where the KE_{NIW} increased more than 20 J m^{-2} .

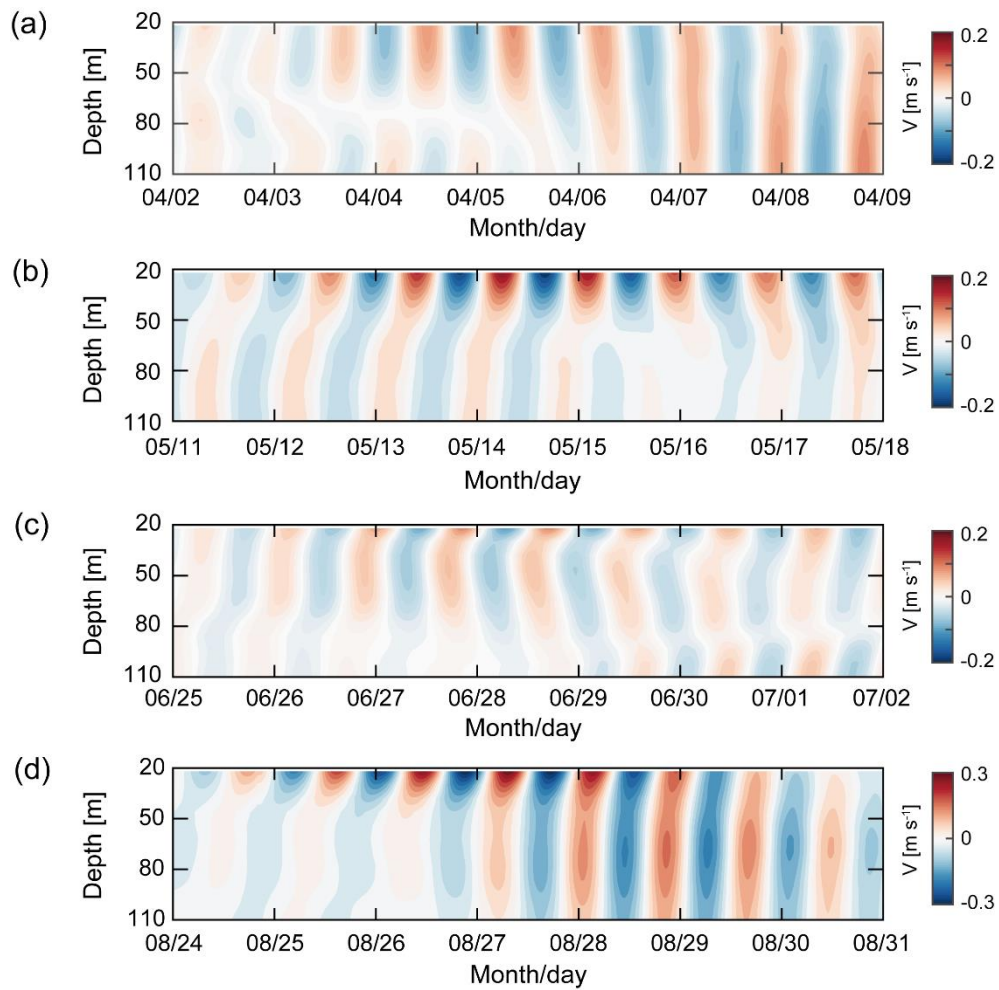


Figure 3.3. Meridional components of NIWs during (a) Event 1, (b) Event 2, (c) Event 3, and (d) Event 4.

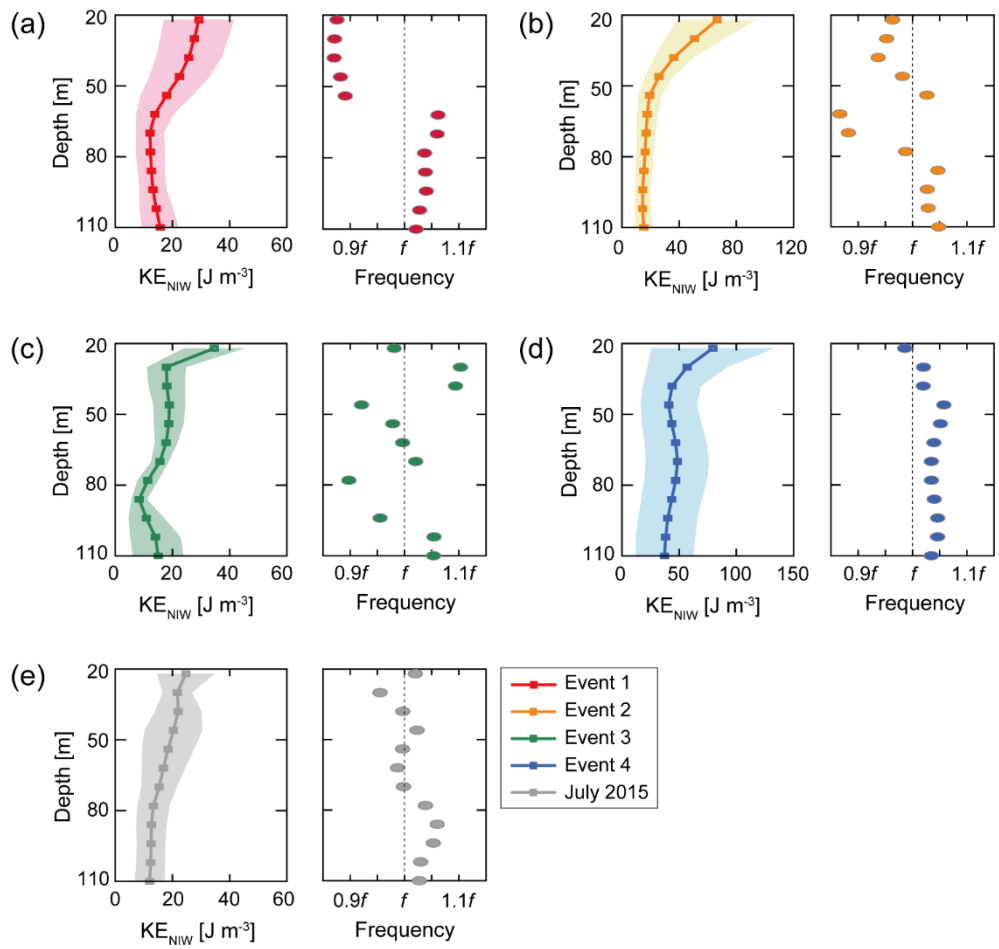


Figure 3.4. Vertical structure of KE_{NIW} and NIW frequencies during (a) Event 1, (b) Event 2, (c) Event 3, (d) Event 4, and (e) typhoon passing period in July.

3.4. Discussion

3.4.1. Unfavorable wind conditions for NIWs under the local typhoon passage

Even if there was strong wind stress as a typhoon passed near the EC1, the NIWs were not generated proportional to the wind stress amplitude (Figures 3.2a–3.2f). During four-typhoon period, the KE_{NIW} reproduced by damped slab model was proportional to the wind stress, but the observed KE_{NIW} did not follow the wind stress amplitude, except case of typhoon GONI (Figure 3.2e). The NIWs are well generated when the wind and current resonance occurs (Crawford and Large, 1996; Furuichi et al., 2008), and the duration or rotation of the wind could be key factors. For each typhoon, CHAN-HOM moved northeastward, landed on Korean Peninsula in 13 July (Figure 3.1) providing clockwise wind rotation near the EC1, and increased wind stress by CHAN-HOM lasted for more than 3 days (not shown). Typhoon NANGKA, passing the right side of EC1, permitted the counter-clockwise wind rotation and also lasted for 3 days. Typhoon HALOLA provided clockwise rotating wind stress up to 8 days and dissipated in 26 July. These typhoons were not favourable for resonance with the NIWs, since the wind stress lasted longer than f , regardless of the wind rotation. Besides, typhoon GONI (corresponding Event 4) had sustained strong wind stress for more than a day at the EC1 and rotated the wind counter-clockwise yielding unfavourable condition, but it was thought that the wind stress itself was strong that can generate the NIW.

3.4.2. Favorable wind conditions for NIWs induced by local and remote passages of typhoon

Significant wind stress was found in the Events 1–3, although there was no typhoon that affected near the EC1. The East Sea is known to be controlled by the East Asian monsoon, and strong wind stresses commonly appear in wintertime (Trusenkova et al., 2007). Therefore, it is necessary to examine the strong wind stress that does not accompany typhoons. As a possible mechanism for intermittent wind amplification, changes in the wind field caused by typhoons and atmospheric pressure pattern in the South China Sea and Northwest Pacific were considered. In 2015, the El Nino controlled the atmospheric and oceanic condition (TCC, 2015), and it is known that the tropical cyclones passed the South China Sea between April and May can trigger the onset of South China Sea summer monsoon (Huangfu et al., 2017). From the geopotential height and wind at 850 hPa before and after the wind stress near the EC1 was amplified, it was found that three typhoons (MAYSAK in April, NOUL in May, and KUJIRA in late June) passed or landed into the South China Sea during the Event 1–3 (Figure 3.5). The typhoons were affected by north Pacific High and moved northwestward to the South China Sea, as the southward shifted westerlies strengthened around 30 °N, the southwesterly or southerly wind was found in the East Sea.

The duration of intermittent wind pulse during the Events 1–3 were closed to local inertial periods accompanying clockwise rotating wind stress (Figure 3.6). For example, the winds lasted about 16 hours on April 2, about 20 hours on May 11, and about 21 hours on June 26. At this time, the rotating direction of total and near-inertial wind stress was clockwise which was favourable to resonance with NIWs in

the Northern Hemisphere. Typhoon GONI during the Event 4 had sustained strong wind stress, even though it provided unfavourable wind duration and counter-clockwise rotation for NIWs. However, typhoon GONI occurred and rapidly developed into typhoon within 24 hours in the Pacific Ocean where the sea surface temperature was high (~29 °C) under the El Nino, and transformed into an extratropical cyclone as it passed near the EC1 showing highest wind stress during whole period (JMA, 2015; KMA, 2016).

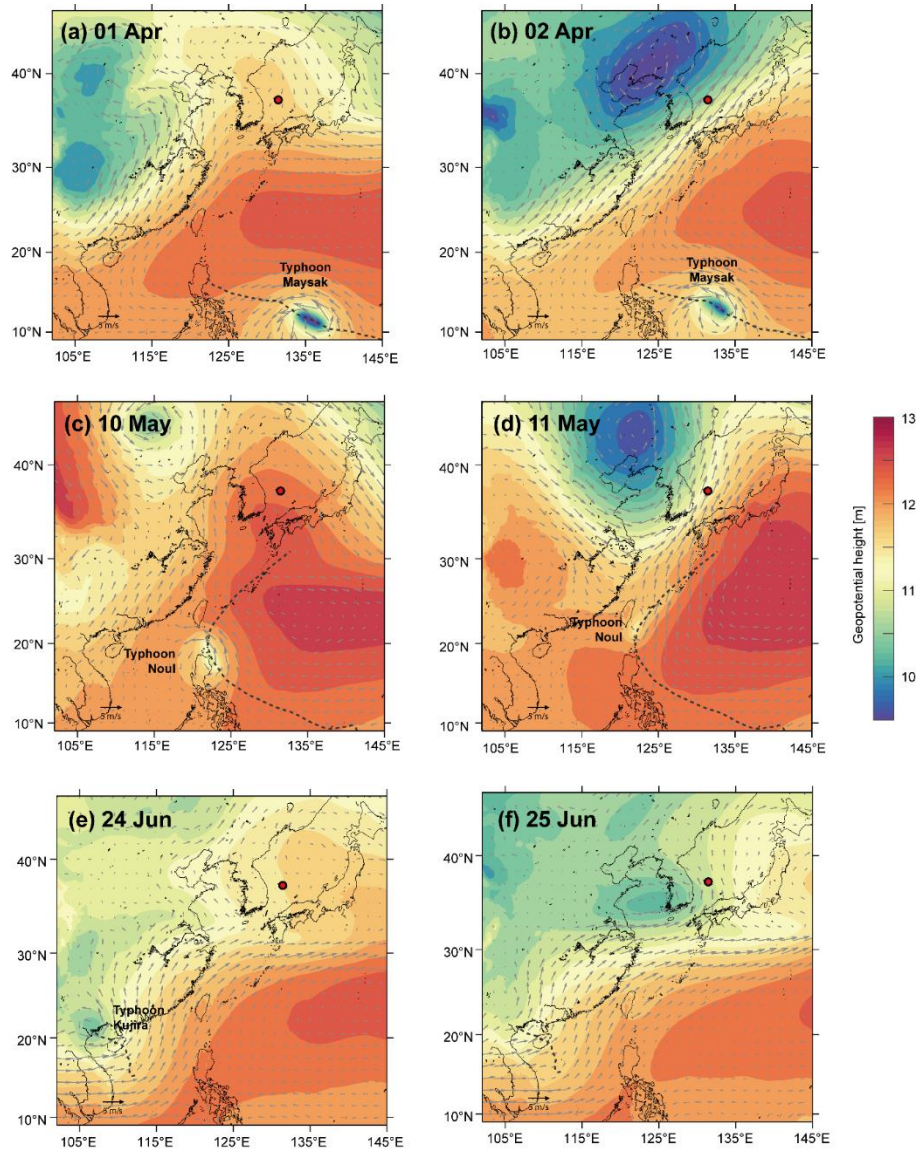


Figure 3.5. Geopotential height (colour shading) and wind (vectors) at 850 hPa. The dashed lines indicate typhoon track and red square represent the EC1.

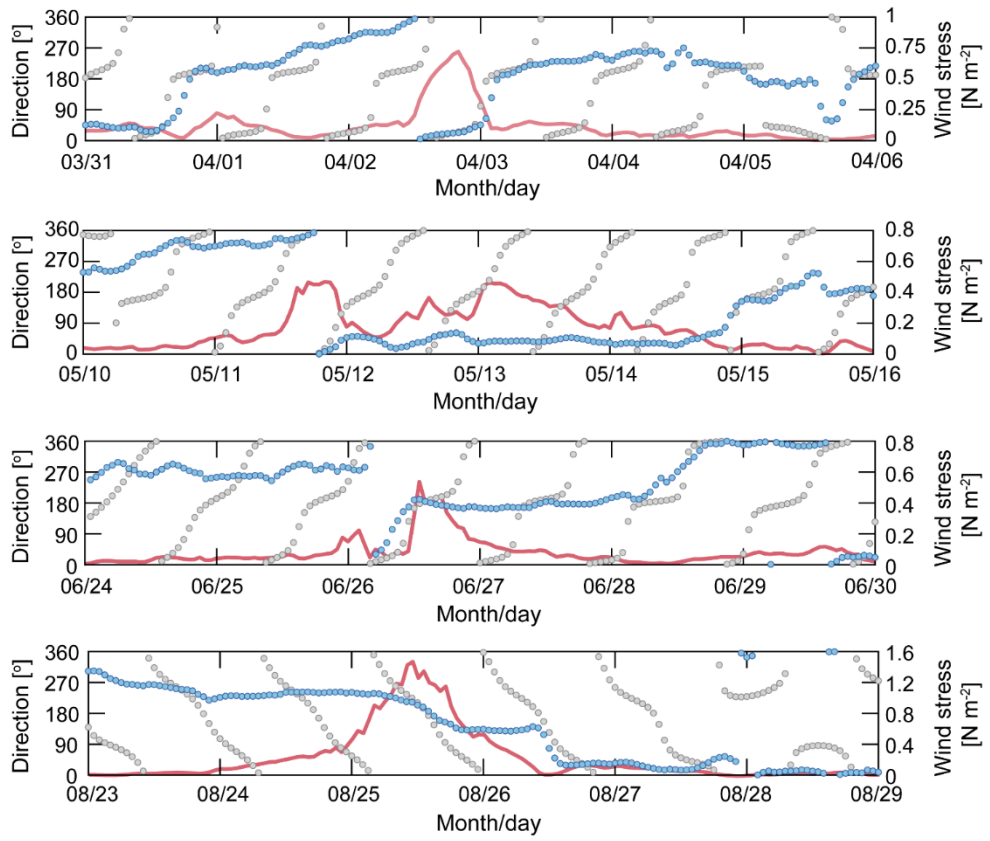


Figure 3.6. Time series of wind stress amplitude (red thick line), wind direction (blue dots), and near-inertial wind direction (grey dots).

3.4.3. Favorable and unfavorable mesoscale conditions for NIWs modulated by relative vorticity

Although the wind was favourable to the NIW generation during the Events 1–4, significant enhancement of KE_{NIW} appeared in Events 2 and 4 (Figures 3.2e, 3.2f and 3.4). The anticyclonic UWE, which persisted over the 2 years from October 2014, was located in the southwestern East Sea, and the mooring sites was located on the eastern rim of the UWE during the observation periods (Figure 3.1). The observed southward subinertial currents and negative vorticity during the periods also confirmed that the EC1 was located eastern side of the UWE (Figures 3.2h and 3.7).

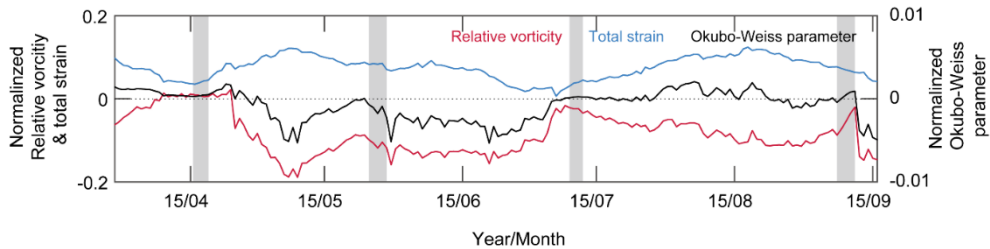


Figure 3.7. Time series of relative vorticity (red), total strain (blue), and Okubo-Weiss parameter (black) near the EC1. Each term is normalized by f or f^2 . Shaded boxes indicate event periods

This study considered the NIW trapping and downward rapid radiation in region of negative vorticity (Danioux et al., 2015; Kunze, 1985; Lee and Niller, 1998). Here, straining of NIWs was discarded since the Okubo-Weiss parameter was close to zero or had a negative sign during the events indicating dominance of vortical mesoscale circulation. Based on the eddy tracking, EC1 was located at or outside the UWE depending on the extension or shrinking of the UWE (Figure 3.8). During Events 2 and 4, the EC1 was located at the UWE boundary, and during Events 1, 3, and mid-

late July, it was located outside the UWE. Comparing the Events 2 and 3, the f_{eff} was lowered than f due to the negative vorticity of the UWE during the Event 2, which was favourable for NIW amplification, whereas in Event 3, the observed NIW frequencies showed blue shift at depths of high KE_{NIW} (Figures 3.4b and 3.4c). It was contrast to the frequency during the Event 2 that lowered than f at depths of high KE_{NIW} , suggesting that NIW trapping was effective in Event 2. In Event 4, there were no red shifts in the NIW frequencies, which was presumed to be locally generated after passing typhoon GONI and downward radiated. Considering 1st term of minimum frequency of NIWs, $\omega_m \approx f_{eff} - \frac{f}{2N^2} \left(\frac{\partial V}{\partial Z} \right)^2$ (Federiuk and Allen, 1996), the ω_m averaged over the Event 2 was $\sim 0.83f$ which was less than $\sim 0.09f$ of Event 4 supporting the favourable conditions for red shifted NIWs during Event 2. Also, the 2nd term in Event 2 was 1.42 times smaller than that of Event 4, that estimated by 40-hour low-passed observed current. During the mid-late July, the NIW frequency was mostly higher than f (blue shift), since the EC1 was located outside the UWE indicating no favourable condition for NIW trapping (Figure 3.4e).

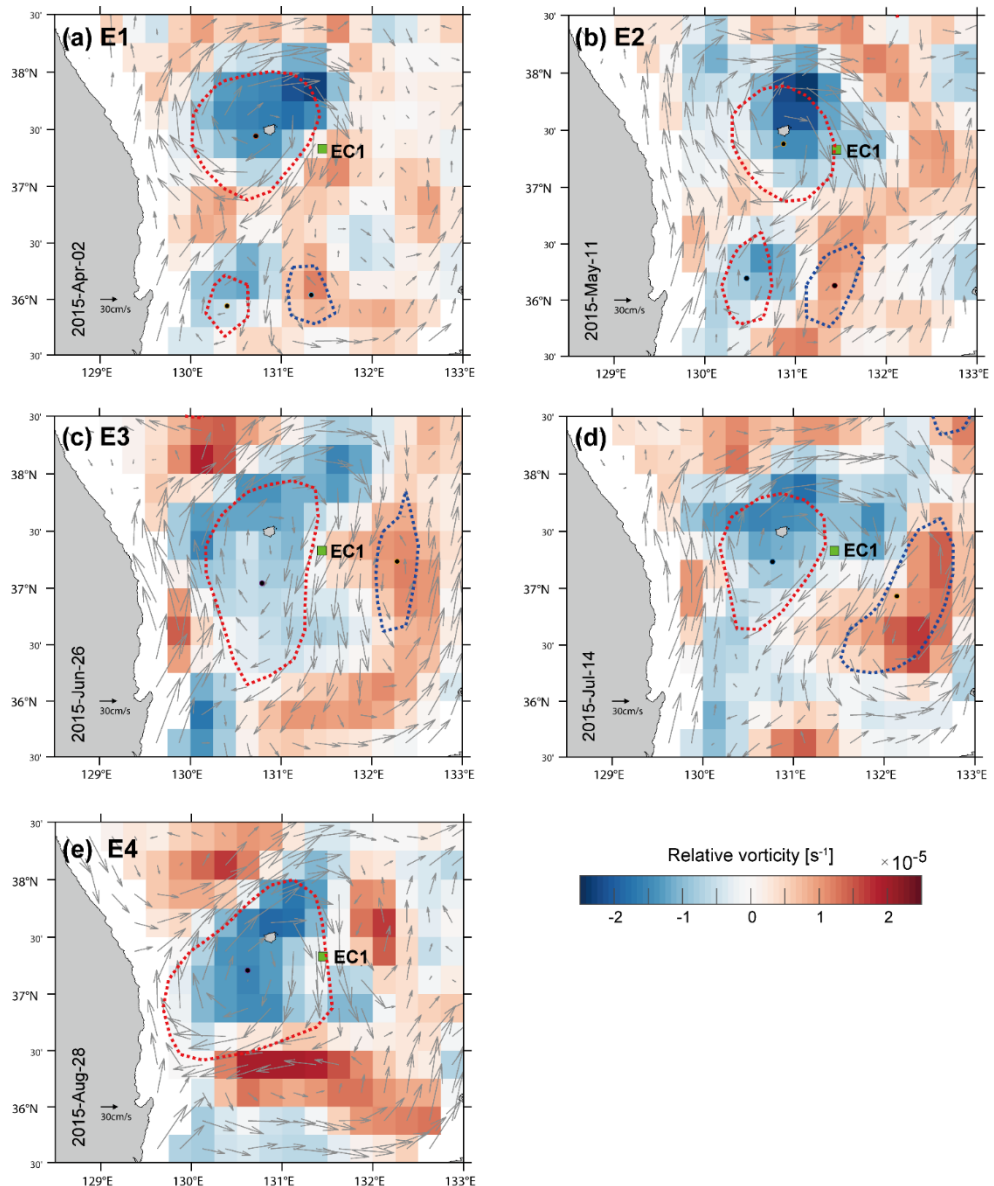


Figure 3.8. Maps of geostrophic currents (grey arrows) and relative vorticity (colour shading). Red and blue dotted lines indicate the boundaries of anticyclonic and cyclonic eddies which are detected by eddy tracking method. Black dot indicates the center of eddy. The EC1 is marked by green square.

3.5. Conclusion

The temporal variations of NIWs upper 100 m were sensitive to favourable wind condition that lasted nearly local inertial period with clockwise rotation, and negative vorticity fields provided by UWE. The wind stress amplitude significantly increased in April, May, June, and August in 2015, but there was no typhoon that could amplify the wind stress, except Event 4. The most energetic KE_{NIW} with blue shift at all depths was found in Event 4, which was generated after typhoon GONI passing. During the Events 1 and 3, the NIW was not effectively generated and amplified. In particular, in mid-late July, the KE_{NIW} was less than 20 J m^{-2} even though three typhoons sequentially passed and increased the wind near the EC1 over the 3 days. The winds that persisted similar to the local inertial period were shown to favour NIW generation such as Events 1–3. The extension and shrinking of UWE also played an important role in the NIW amplification by including or excluding the mooring site within the UWE. The wind-induced NIWs was trapped in region of anticyclonic eddy UWE due to the lowered f_{eff} , and effectively enhanced (e.g., Event 2 and 4).

In 2015, the El Niño occurred in the Pacific Ocean supports the typhoon generation, and also affects atmospheric patterns such as southward shifted westerlies. The interaction among north Pacific High, southward shifted westerlies and typhoons traveling toward South China Sea can amplify NIW in the East Sea in summertime by changing the wind field. The fact that the wind field in the East Sea changes within few days as the typhoons (e.g., MAYSAK, NOUL, KUJIRA) moved to the South China Sea that controlled by atmospheric pressure fields, and the resulting NIW propagates into the ocean interior has implications in terms of ocean-

atmosphere interaction. This implies that kinetic energies in the atmosphere can be transferred to the ocean remotely. So, further studies are needed to determine how much energy the remotely generated NIW transfers into the ocean.

4. Nonseasonal variability of near-inertial kinetic energy from 21-year-long observations

4.1. Introduction

Near-inertial internal gravity waves (NIWs), with frequencies close to the local inertial frequency f , are ubiquitous in the stratified rotating ocean. The NIWs are mainly originated from surface wind forcing, enhanced primarily within the surface mixed layer, propagate into the ocean interior below the mixed layer and equatorward in general, and ultimately dissipate enhancing turbulent mixing (Garrett, 2001; Alford et al., 2016; MacKinnon et al., 2017; Whalen et al., 2018). The rate of work done by surface wind on global mixed layer NIWs is known as to range from 0.3 to 1.3 TW which is comparable to energy power globally converting from barotropic to baroclinic tides, e.g., 1.0-1.2 TW (Egbert and Ray, 2000; Nycander, 2005; Jiang et al., 2005). Both winds and tides play a key role in providing energy to induce turbulent mixing, and redistributing energy and materials in the ocean (MacKinnon et al., 2017; Garrett and Munk, 1979; Munk and Wunsch, 1998; Müller and Briscoe, 2000; Alford, 2003; Ferrari and Wunsch, 2009; Whalen et al., 2020). Along with turbulence mixing driven by tides, the NIW-driven mixing may sustain the meridional overturning circulation (Whalen et al., 2020; Nikurashin and Ferrari, 2013; Vic et al., 2019), and the near-inertial variations of the meridional overturning circulation was suggested from numerical simulations (Blaker et al., 2012; Xiao et al., 2016). The NIWs also affect, via turbulent fluxes, nutrient and carbon cycles that influence primary production, and marine ecosystem (Lucas et al., 2011; Pan et al., 2012; Muacho et al., 2013; Villamaña et al., 2017; Li et al., 2018; Song et al., 2019).

Generation, evolution, propagation, and decay of NIWs are affected by mesoscale flow fields as well as wind forcing (Alford et al., 2016; Kunze, 1985; D'asaro, 1995; Whitt and Thomas, 2015; Jing et al., 2017). One way of interaction between the mesoscale flow fields and NIWs is a trapping (reflection) of NIWs in a region of negative (positive) relative vorticity that decreases (increases) the effective Coriolis frequency playing as a waveguide. Although the NIWs freely propagate between f and N (buoyancy frequency) in general, the relative vorticity shifts the lowest limit from f to an effective Coriolis frequency (Kunze, 1985; Lee and Niiler, 1998; Danioux et al., 2008). Thus, the NIWs entering into a region of negative relative vorticity or low effective Coriolis frequency can hardly propagate out of the region but be trapped. Another way of interaction between the mesoscale flow fields and NIWs is a process named ‘wave capture’ where the NIWs can draw energy from the mesoscale flow fields under the condition of rate of strain exceeding relative vorticity (Bühler et al., 2005; Polzin, 2008; Polzin, 2010; Jing et al., 2018). Under this condition (strain dominates vorticity), the vertical and horizontal wavenumbers of NIWs increase exponentially and those NIWs with growing wavenumber magnitude are tend to be captured within the strain field and eventually dissipate.

Previous studies on the observed and simulated NIWs interacting with the mesoscale flow fields in the East Sea have been reported. Formation, presence, and decay of mesoscale eddies are frequently observed in the East Sea, particularly off the east coast of Korea, partly associated with the strong meandering of the East Korea Warm Current. A semi-permanent anticyclonic eddy, called the Ulleung Warm Eddy (UWE), is often found off the coast where the boundary current forms and separates (Chang et al., 2004; Shin et al., 2005)). Seasonal variation of NIWs with winter intensification was reported by Mori et al. 2005 and Jeon et al. 2019 in

association to East Asian Monsoon. Year-to-year variation of NIW kinetic energy observed off the coast was suggestively related to mesoscale fields imposed by UWE and Tsushima warm current (Park and Watts, 2005). Upward reflection of downward propagating NIWs by the UWE was also observed (Byun et al., 2010). Likewise, the effects of relative vorticity imposed by mesoscale circulation on enhancement of NIWs off the coast have been examined previously. However, except Noh and Nam (2020) that reports the importance of mesoscale strain fields on enhancement of NIWs for a specific case, the effects of mesoscale flow fields on temporal variations of characteristics of NIWs in the region beyond the seasonal cycle have not been presented from the observations to date.

Thus, this study first describes intraseasonal, interannual, and decadal variations of NIW kinetic energy from 21-year-long moored time-series observations in the southwestern East Sea. Then, the statistically significant effects of mesoscale flow fields on the nonseasonal variations of NIW kinetic energy are discussed. Data used in and methods applied to this study are described in the next chapter. In chapter 4.3, results of moored observations and damped slab model are presented. This chapter will discuss the results on the nonseasonal variations of NIW kinetic energy in terms of surface wind forcing and mesoscale field variability.

4.2. Data and method

4.2.1. Data

Long time-series data of zonal and meridional currents have been collected using a subsurface mooring, named EC1, located between Ulleugdo and Dokdo at a water depth of 2300 m since 1996 (Figure 4.1). The EC1 has been turned around 23 times (as of June 2021) and equipped for most period with current-meters at three nominal depths (400, 1400, and 2200 m). Rotary-type current meters (Aanderaa RCM 7 and 8) and Doppler-type current meters (Aanderaa RCM 9 and 11; Nortek Aquadopp) were attached to the mooring and recorded continuous time series data with a sampling interval equal or less than 1 hour. An upward-looking acoustic Doppler current profiler (ADCP, 75 kHz) was mounted at 500 m with a depth interval (bin size) of 8 m instead of a single-type current meter at 400 m during March 2011 to July 2012. All the EC1 data collected from 1996 to 2020 and upgraded by quality control and quality assurance are currently available at <https://www.seanoe.org/data/00677/78916/> (Lee and Nam, 2021). In this study, the time-series data of currents collected at 400 m of the EC1 for the 21 years from January 2000 to November 2020 were used.

To supplement the moored time-series data at a horizontally fixed position, the Met Office Hadley Center EN4.2.1. (hereafter EN4) data that passed the global quality control processing were used. The EN4 data consist of temperature and salinity obtained from profiling instruments, and the main data source is World Ocean Database 2009 (Good and Martin, 2013). Their temporal and spatial resolutions are monthly and 1°, respectively. Since the spatial resolution of EN4 is coarser than first baroclinic Rossby radius of deformation of ~O(10 km) (Chelton et

al., 1998), surface mixed layer depth (MLD) estimated from EN4 was verified against MLD estimated from Lim et al. (2012) that were based on the World Ocean Database 2005 and multi-source hydrographic data. Satellite altimetry-derived daily sea surface height (absolute dynamic topography above geoid, ADT) of gridded level-4 data provided by the Copernicus Marine Environment Monitoring Service were used to calculate surface geostrophic currents at a spatial resolution of 0.25°. The ADT was obtained by adding a Mean Dynamic Topography (MDT) to the sea level anomaly field, and processed by the Data Unification and Altimeter Combination System multi-mission altimeter data processing system that merged altimeter missions. The MDT is an estimate of the mean over the 1993–2012 period of the sea surface height above geoid (Mulet et al., 2021). Hourly sea surface wind data from January 2000 to November 2020 along a meridional line at 131 °E (green dotted line in Figure 4.1) with a horizontal resolution of 30 km were used to calculate local wind stress, $\vec{\tau} = (\tau_x, \tau_y)$, which are available on the European Center for Medium-Range Weather Forecasts Reanalysis version 5 (ERA5, <https://www.ecmwf.int/en/forecasts/datasets/reanalysis-datasets/era5>).

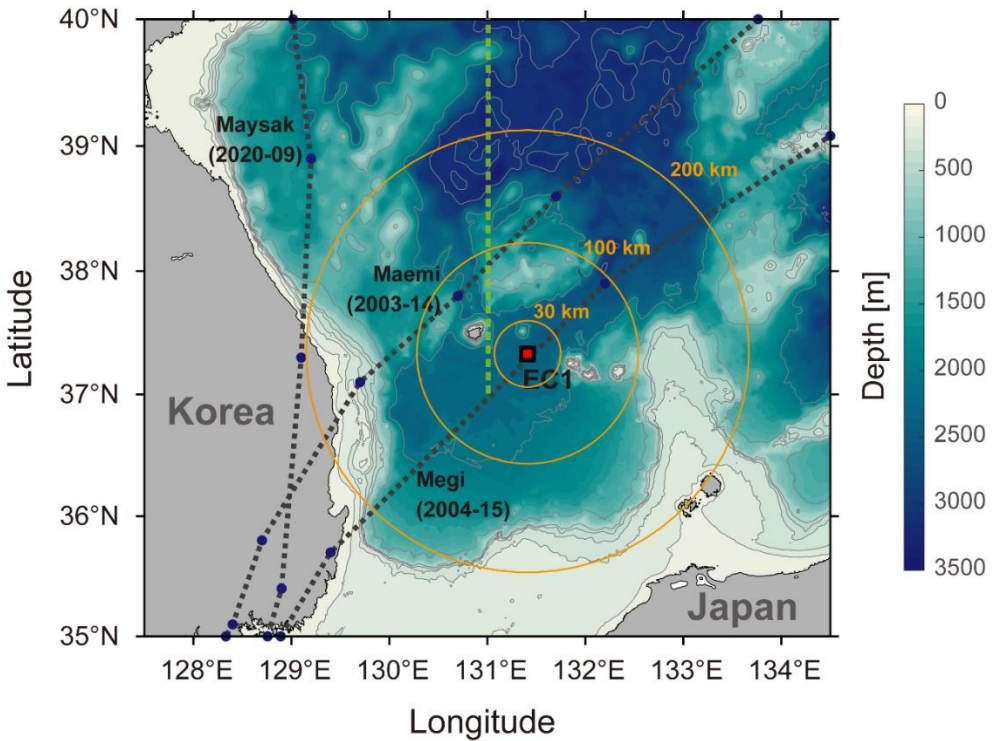


Figure 4.1. Location of subsurface mooring EC1 (red square) with bathymetry (color) in the southwestern East Sea off the east coast of Korea. Green dotted line indicates meridional line where sea surface wind data are extracted. Black dashed lines indicate trajectories of typhoon Maemi (2003-14), Megi (2004-15), and Maysak (2020-09). The yellow circles indicate 30, 100 and 200 km radius centered at EC1, respectively.

4.2.2. Method

Zonal and meridional currents (u, v) observed at 400 m of EC1 were processed following the flow chart shown in Figure 4.2. Raw data extracted from the current-meters were quality controlled by following the standard procedure for the instrument types (IOOS, 2019; Min et al., 2020), and then converted to hourly data with subsampling. The minimum current speed of 1.1 cm s^{-1} measured by rotary-type current meter RCM was treated as a stall and removed from the successive processing. Consecutive missing data less than 6 hours were linearly interpolated, and those longer than 6 hours were set as bad data to exclude from the analysis. Since the depths where the current-meters were mounted differ from the nominal depths as the mooring tilted by the drag due to horizontal currents, a linear interpolation (or extrapolation) was also performed vertically to yield the horizontal currents (u, v) at 400 m. The NIWs with zonal and meridional components of horizontal oscillations (u_{NIW}, v_{NIW}) were extracted from (u, v) applying phase-preserving fourth-order Butterworth bandpass filter with cut-off frequencies of $0.85f$ and $1.15f$ where f is about 0.0505 cph corresponding period is 19.8 hour. Amplitude and horizontal kinetic energy of NIW were computed as $\sqrt{u_{NIW}^2 + v_{NIW}^2}$ and $KE_{NIW_obs} = 0.5\sigma_{\theta_0}(u_{NIW}^2 + v_{NIW}^2)$ where σ_{θ_0} is reference density ($=1025.0 \text{ kg m}^{-3}$). Since the density in fact is not constant to the reference density but varies over time, near-inertial potential energy should also be considered to present the mechanical energy as a summation of kinetic energy and potential energy. Instead, time-varying WKB scaling factor, $[N(x, y, z, t)/N_0]^{-1/2}$ (Leaman and Sanford, 1975), at 400 m was estimated to quantify the effect of NIW potential energy variations where $N = [-(g/\sigma_{\theta})/(d\sigma_{\theta}/dz)]^{1/2}$ is a buoyancy frequency, and z, t, N_0, g , and σ_{θ} are the

vertical coordinate, time, reference buoyancy frequency, gravity acceleration (set to 9.83 m s^{-2}) and potential density, respectively. Here, N_0 is set to $0.0046 \text{ rad s}^{-1}$ based on the EN4 data at the upper 500 m in the vicinity of EC1 from 2000 to 2020 by averaging vertical profiles of buoyancy frequencies.

The intraseasonal variation of KE_{NIW} ($\text{KE}_{\text{NIW_obs_int}}$) was obtained by applying wavelet analysis to the $\text{KE}_{\text{NIW_obs}}$ and then intraseasonal scale-averaged variances were extracted from the wavelet results. Here, intraseasonal band was set to 3–100 days, considering previously reported results on the mesoscale eddies in the region, e.g., mean life time of mesoscale eddies was estimated to 95 days (Lee et al., 2019). The MATLAB version of wavelet toolbox (Torrence and Compo, 1998) was used (<http://atoc.colorado.edu/research/wavelets/>). Events for high KE_{NIW} (Period High) were defined as the criterion exceeding 1 standard deviation ($\sigma \sim 0.1$) from the mean ($\mu \sim 0.05$) of the intraseasonal KE_{NIW} normalized to its maximum over the total period (i.e., Period High $> \sigma + \mu \sim 0.15$). Events for low KE_{NIW} (Period Low) were selected to match total number of event days (505 days) same as that of Period High after sorting KE_{NIW} in order of magnitude, and the rest of periods were defined as Period Neutral (Figure 4.3). Total 9 Period High and 7 Period Low were identified, respectively.

The MLD was defined as a depth where potential density (σ_θ) changed by given threshold criterion ($\Delta\sigma_\theta$) relative to that at a reference depth (Lim et al., 2012; de Boyer Montégut, 2004). The threshold was calculated from temperature change (ΔT) relative to that at the reference depth as below.

$$\Delta\sigma_\theta = \sigma_\theta(T_{ref} + \Delta T, S_{ref}, P_0) - \sigma_\theta(T_{ref}, S_{ref}, P_0)$$

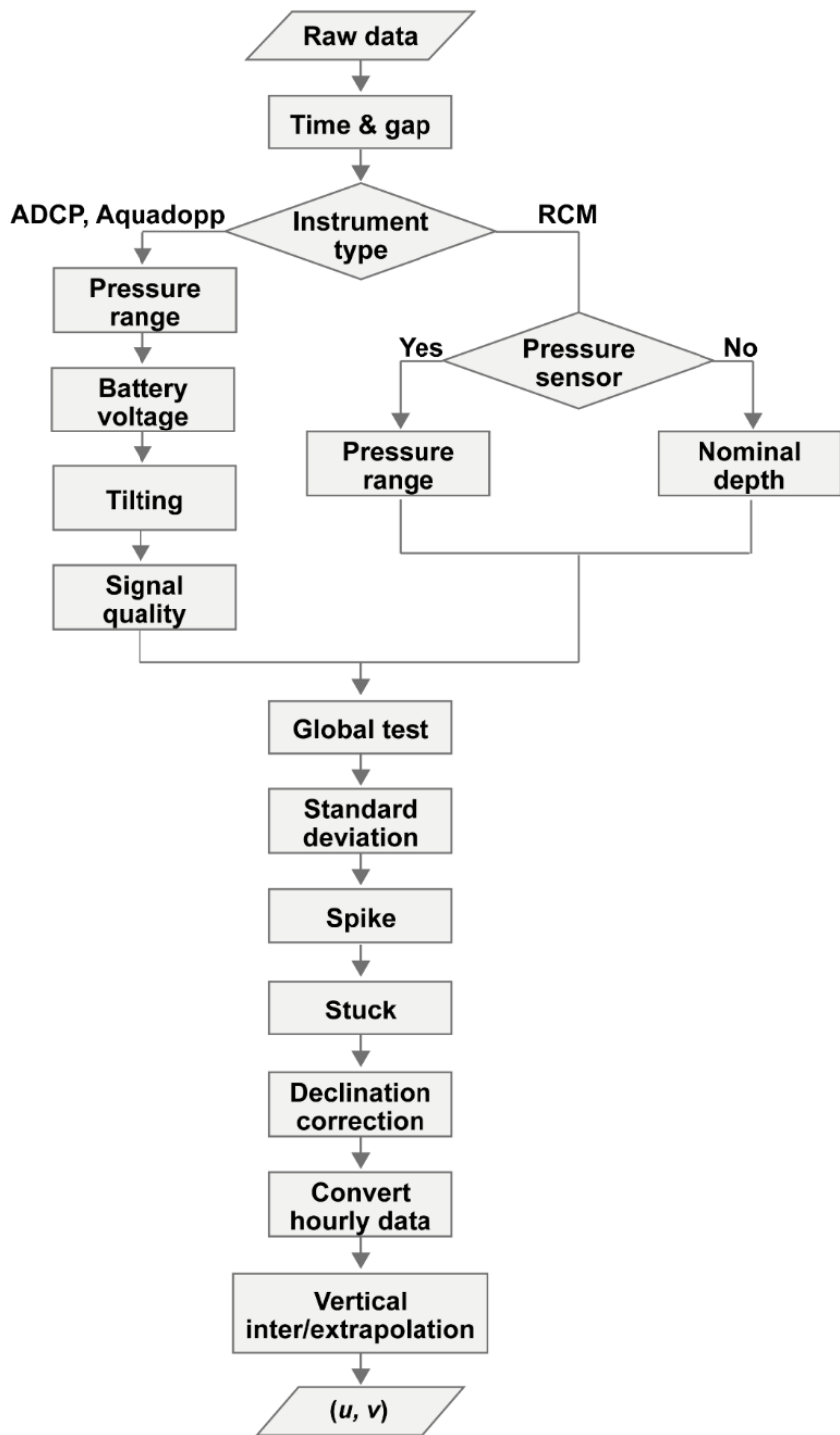


Figure 4.2. A flow chart for processing of horizontal current data collected at EC1

Here, T_{ref} and S_{ref} are the temperature and salinity at the reference depth derived from the EN4 data at the nearest grid to the EC1, and P_0 is pressure at the sea surface (set to zero). The threshold for temperature change and reference depth were set to $\Delta T = 0.2$ °C and 10 m following to Lim et al. (2012). The σ and μ of MLD averaged over the period are 23 and 17 m, respectively (maximum of 84 m in January 2011 and minimum of 10 m in August 2006). The MLD varied seasonally with its minimum reached in summer (shallow MLD) and maximum in winter (deep MLD), and interannually with less (more) deepened in winters of 2008-2009 and 2014-2015 (2002-2003, 2010-2011, and 2018-2019) compared to other years (Figure 4.3). The MLDs estimated by Lim et al. (2012) using the data collected within 1° distance from the EC1 mooring site are compared to validate the MLD estimated from the EN4 where correlation coefficient between the two MLD time series is 0.76.

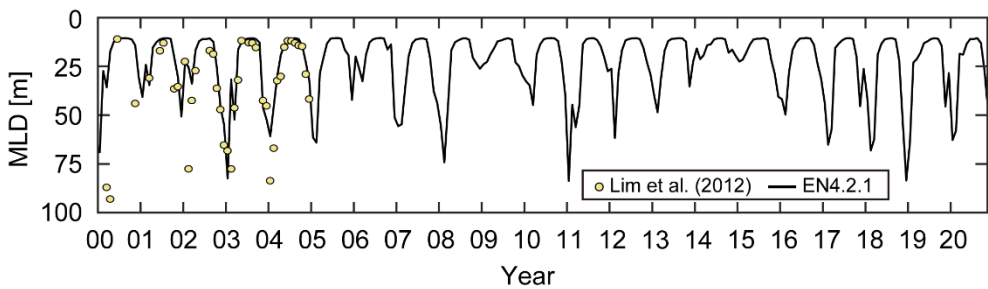


Figure 4.3. Monthly MLD estimated from EN4 (black line) compared to that from Lim et al. (2012) (yellow dot).

To estimate the inertial response of the upper ocean in the mixed layer to surface wind forcing, a damped slab model with zonal and meridional momentum equations as described in chapter 2.2. was used. The damping time scale r^{-1} was fixed to 4 days considering previous studies (Mori et al., 2005; Jeon et al., 2019; Park et al., 2009; Kawaguchi et al., 2020), and the time-varying MLD estimated from EN4 was used for H_{ML} . The amplitude and kinetic energy of modeled NIWs were calculated as $\sqrt{u_{ML}^2 + v_{ML}^2}$ and $KE_{NIW_model} = 0.5\sigma_{\theta_0}(u_{ML}^2 + v_{ML}^2)$, respectively. The intraseasonal variations of KE_{NIW_model} ($KE_{NIW_model_int}$) was calculated in the same manner as those at 400 m applying wavelet analysis. The rate of wind work (Π) was calculated using the following way (inner product of surface wind stress and modeled mixed layer currents),

$$\Pi = \tau_{x_{NIW}} u_{ML} + \tau_{y_{NIW}} v_{ML}$$

where $\tau_{x_{NIW}}$ and $\tau_{y_{NIW}}$ are near-inertial band-passed zonal and meridional wind stress along the meridional line (see Figure 4.1). Note that the mixed layer currents (u_{ML} , v_{ML}) estimated using the damped slab model represent the near-inertial currents in MLD and the NIWs at sea surface during the periods.

Ray path of NIWs in the spatially varying stratification along the 131 °E (Figure 4.1) was computed following (Chiswell, 2003),

$$\frac{2}{3}y^{3/2} = -\frac{1}{(2\omega\beta)^{1/2}} \int N(y, z, t) dz$$

where y is meridional travel distance, ω is the NIW frequency, N is the buoyancy frequency estimated using the EN4 data, and β is the meridional gradient of f ($= \partial f / \partial y$). Here, the background flow fields were not considered.

In order to examine the effect of the mesoscale flow fields on the KE_{NIW_obst} , background conditions quantified from the satellite altimetry-derived surface geostrophic currents $\vec{U} = (U, V)$. The Okubo-Weiss parameter (α^2) and effective Coriolis frequency are same as described in chapter 2.2

To investigate whether there is a statistically significant effect of mesoscale flow fields on the $KE_{NIW_obs_int}$, composite analysis was done with Π , ζ , S^2 , and α^2 for Period High, Period Neutral, and Period Low using Welch's t-test with 95 % significance level (p-value < 0.05) (Tables 4.1 and 4.2). Then, the events were classified by four categories based on the ζ and α^2 (Table 4.3). Dominance of S^2 to ζ^2 was determined by the sign of α^2 (e.g., when $\alpha^2 > 0$, the S^2 dominated ζ^2). The references for ζ and α^2 were set to zero.

4.3. Results

4.3.1. Intraseasonal, interannual, and decadal variations of KE_{NIW} at 400 m and NIWs in mixed layer

The KE_{NIW_obs_int} showed intraseasonal, interannual and decadal variations from 2000 to 2020 (Figure 4.4 and Tables 4.1–4.2). The KE_{NIW_obs_int} averaged over Period High (red shaded box) was about 12 times higher than that of Period Neural, while the KE_{NIW_obs_int} averaged over Period Low (blue shaded box) showed the kinetic energy less than 3 % of Period Neutral with 95 % significance. During the Period Low, there were almost no KE_{NIW_obs_int} at 400 m ($<0.02 \text{ (J m}^{-3}\text{)}^2$). The longest Period High (Period Low) was the H9 (L1) lasting 134 days (167 days) whereas the shortest Period High (Period Low) was H8 (L3) with 7 days (11 days). But, it is cautious to mention L3 since there was no observed current data just before and after L3. Interannual variation of the KE_{NIW_obs_int} increased in 2003, 2010, 2012–2013, 2016, and 2020 reaching the maximum in 2016 (in H5 with $15.32 \text{ (J m}^{-3}\text{)}^2$). In terms of decadal variations of KE_{NIW_obs_int}, the Period High appeared more frequently in 2010s than 2000s.

Timings of enhancement in KE_{NIW_model_int} do not well match to those of KE_{NIW_obs_int} (Figures 4.4 and 4.5d–4.5e). The KE_{NIW_model_int} (or amplitude of NIWs) greater than $1.0 \times 10^4 \text{ J}^2 \text{ m}^{-6}$ ($\sim 1 \text{ m s}^{-1}$) were found in 12 September 2003, 19 August 2004, and 3 September 2020 (green triangles in Figures 4.5d and 4.5e) whereas only the first one corresponds to the Period High (H2). The H5 was the period when the KE_{NIW_obs_int} was the largest, and the wind energy input reached during the period was about 8 kJ m^{-2} , which was in contrast to the H2 with wind energy input of about 33 kJ m^{-2} . In contrast to the KE_{NIW_obs_int} during the H5 and

H9, the $\text{KE}_{\text{NIW_model_int}}$ was less than $0.5 \times 10^4 \text{ J}^2 \text{ m}^{-6}$. Except for H2 and H5, the amplitude of modeled NIWs and the $\text{KE}_{\text{NIW_model_int}}$ among the Period High and Period Low were less than 0.2 m s^{-1} and $2.0 \times 10^3 \text{ J}^2 \text{ m}^{-6}$. Furthermore, there is no significant difference in the $\text{KE}_{\text{NIW_model_int}}$ before and after the 2010s, except the typhoon passed period.

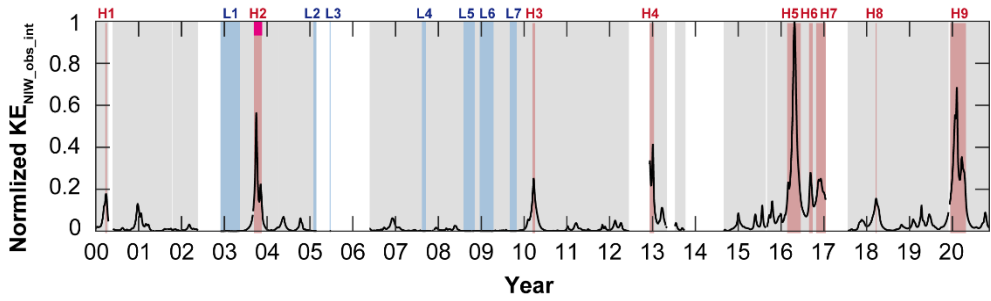


Figure 4.4. Time-series of normalized intraseasonal variations of KENIW at 400 m ($\text{KE}_{\text{NIW_obs_int}}$) from 2000 to 2020. Red (blue) shaded boxes indicate Period High (Period Low) and gray shaded area indicates Period Neutral. White area represents the data gap (no data available). The Events 2–4 in Noh and Nam (2020) are marked at the top of H2 (pink)

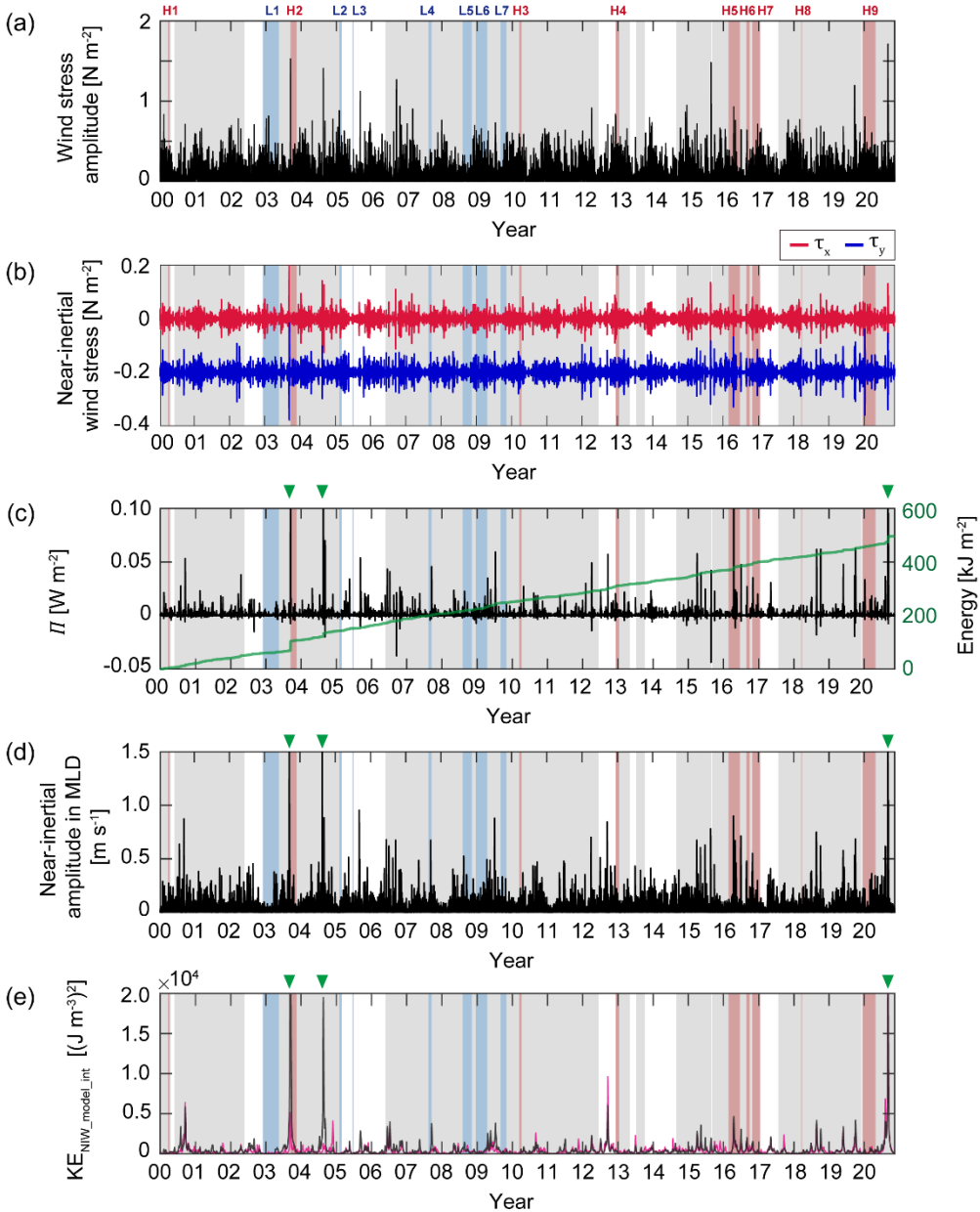


Figure 4.5. Time-series of (a) wind stress amplitude, (b) near-inertial wind stress, (c) Π (left axis) and time integral of Π showing cumulative energy input from surface wind to MLD currents (green solid line, right axis), and (d) near-inertial amplitude in MLD, $\sqrt{u_{ML}^2 + v_{ML}^2}$, calculated from damped slab model results, and (e) intraseasonal variations of (d). Pink line in (e) indicates intraseasonal variations $\sqrt{u_{ML}^2 + v_{ML}^2}$ averaged over $38-40^\circ\text{N}$. Red (blue) shaded boxes indicate Period High (Period Low). Gray shaded area indicates Period Neutral. Green triangle in (d) indicates the period when the near-inertial amplitude in MLD is larger than 1 m s^{-1} .

4.3.2. Composite analysis of KE_{NIW} at 400 m and mesoscale conditions

Magnitude of Π and S^2 composited for Period High are larger than those for Period Neutral, and the sign of α^2 and ζ were positive and negative, and these are statistically significant at 95% (Figures 4.5–4.6 and Tables 4.1–4.2). The composited conditions in total Period Low were contrary to those of total Period High. Here, the sign of ζ and α^2 in total Period Low was same to those in total Period Neutral showing positive and negative, respectively. Among the Period High, the Π was larger than that in total Period Neutral, except H1 and H8, while the Π among the Period Low was significantly smaller than that in total Period Neutral, except L6. More than half of the Period High (and Period Low) could be identified by the signs of ζ and α^2 . The role of the ζ was identified by comparing categories I and III, or categories II and VI yielding that more Period High events were found in negative ζ (Table 4.3). The role of S^2 and α^2 was found in categories I and II, or categories III and VI. Total six Period High were found when the S^2 dominated the ζ showing $\alpha^2 > 0$. Despite the positive ζ condition in category I, the H2 and H8 were existed. The KE_{NIW_obs_int} averaged each category was 1.71, 0.01, 5.28, and 4.35 ($J\ m^{-3}$)² and high KE_{NIW_obs_int} was found in $\zeta < 0$ or $\alpha^2 > 0$.

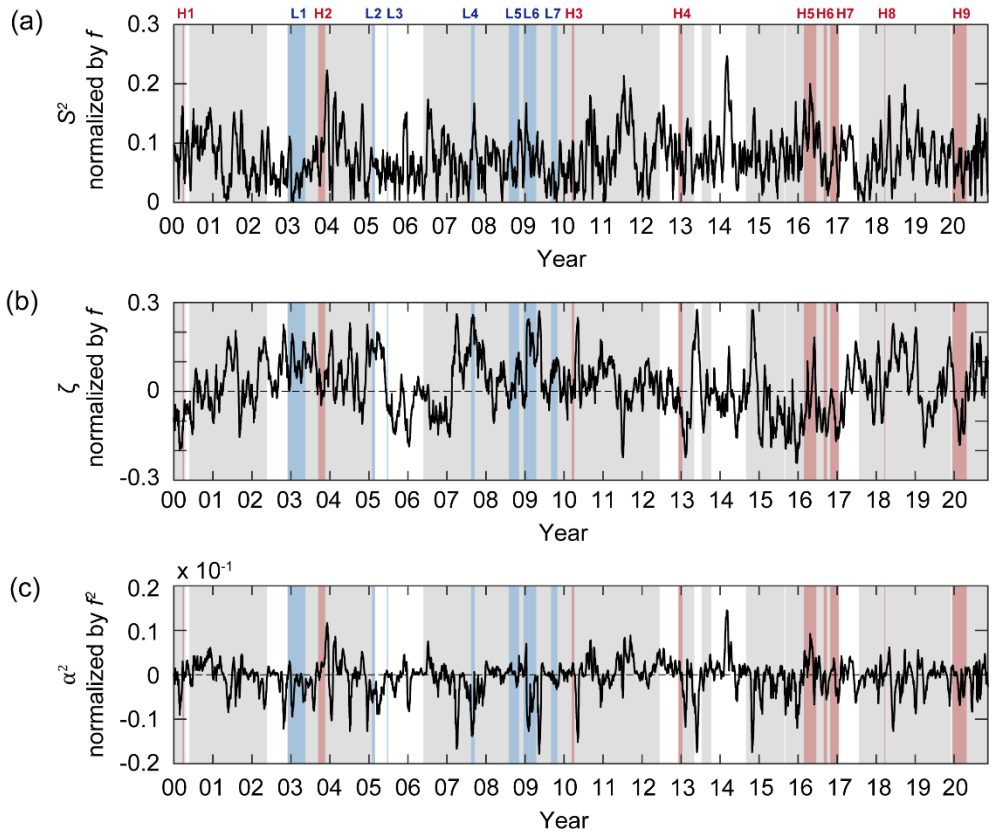


Figure 4.6. Time-series of (a) S^2 normalized by f , (b) ζ normalized by f , and (c) α^2 normalized by f^2 . Red (blue) shaded boxes indicate Period High (Period Low). Gray shaded area indicates Period Neutral.

Table 4.1. Mean and (bracket) standard deviation of four conditions during Period High (bold and underline represent 95 % significant (p-value <0.5)

Period	Π (10^{-3} W m $^{-2}$)	ζ (s $^{-1}$)	S^2 (s $^{-1}$)	α^2 (x 10 $^{-12}$ s $^{-2}$)	
H1	2000/03/22-2000/04/04	<u>0.40</u> (0.62)	<u>-0.11f</u> (0.02f)	<u>0.11f</u> (0.03f)	<u>3.10</u> (9.89)
H2	2003/09/12-2003/11/15	<u>6.66</u> (42.31)	0.01f (0.04f)	0.08f (0.03f)	<u>10.39</u> (10.92)
H3	2010/03/12-2010/04/05	<u>0.94</u> (1.90)	<u>0.00f</u> (0.02f)	0.08f (0.02f)	<u>13.29</u> (6.29)
H4	2012/12/06-2013/01/14	<u>0.80</u> (1.80)	<u>-0.06f</u> (0.03f)	0.08f (0.02f)	<u>4.50</u> (12.45)
H5	2016/02/23-2016/06/18	<u>1.35</u> (6.60)	<u>0.00f</u> (0.08f)	<u>0.13f</u> (0.03f)	<u>23.42</u> (26.68)
H6	2016/08/27-2016/09/26	<u>1.18</u> (3.57)	<u>-0.10f</u> (0.03f)	<u>0.06f</u> (0.02f)	<u>-12.89</u> (17.01)
H7	2016/10/26-2017/01/15	<u>1.22</u> (3.01)	<u>-0.08f</u> (0.06f)	0.07f (0.03f)	-5.90 (22.23)
H8	2018/03/19-2018/03/25	<u>0.10</u> (0.13)	<u>0.04f</u> (0.02f)	<u>0.04f</u> (0.01f)	<u>0.58</u> (1.77)
H9	2019/12/14-2020/04/26	<u>0.82</u> (2.37)	<u>-0.07f</u> (0.08f)	<u>0.06f</u> (0.03f)	<u>-11.16</u> (19.09)
Period High	<u>1.78</u> (15.86)	<u>-0.04f</u> (0.08f)	<u>0.08f</u> (0.04f)	<u>2.80</u> (24.01)	
Period Neutral	0.71 (3.72)	0.02f (0.10f)	0.07f (0.04f)	-4.58 (28.29)	

Table 4.2. Mean and (bracket) standard deviation of four conditions during Period Low (bold and underline represent 95 % significant (p-value <0.5)

Period	Π (10^{-3} W m$^{-2}$)	ζ (s$^{-1}$)	S^2 (s$^{-1}$)	α^2 (x 10$^{-12}$ s$^{-2}$)	
L1	2002/11/30-2003/05/15	<u>0.35</u> (0.99)	<u>0.09f</u> (0.05f)	<u>0.04f</u> (0.03f)	<u>-17.24</u> (23.45)
L2	2005/01/29-2005/02/24	<u>0.36</u> (0.84)	<u>0.15f</u> (0.01f)	<u>0.07f</u> (0.01f)	<u>-33.99</u> (6.42)
L3	2005/06/17-2005/06/28	<u>0.27</u> (0.46)	<u>-0.06f</u> (0.01f)	<u>0.07f</u> (0.01f)	<u>2.77</u> (3.47)
L4	2007/08/14-2007/09/16	<u>0.18</u> (0.61)	<u>0.23f</u> (0.02f)	<u>0.11f</u> (0.03f)	<u>-80.73</u> (25.93)
L5	2008/08/02-2008/11/05	<u>0.56</u> (1.68)	<u>0.03f</u> (0.05f)	<u>0.06f</u> (0.03f)	<u>2.41</u> (10.99)
L6	2008/12/17-2009/04/14	<u>0.78</u> (1.80)	<u>0.13f</u> (0.10f)	<u>0.08f</u> (0.03f)	<u>-33.41</u> (40.14)
L7	2009/09/01-2009/10/29	<u>0.23</u> (0.52)	<u>0.07f</u> (0.02f)	<u>0.04f</u> (0.02f)	<u>-8.59</u> (7.57)
Period Low	<u>0.47</u> (1.33)	<u>0.10f</u> (0.08f)	<u>0.06f</u> (0.03f)	<u>-20.45</u> (32.34)	
Period Neutral	0.71 (3.72)	0.02f (0.10f)	0.07f (0.04f)	-4.58 (28.29)	

Table 4.3. Categories of the KE_{NIW}_obs_int event by three conditions. The positive and negative anomaly denoted by + and -. The reference of ζ and α^2 is set to zero.

Category	ζ	α^2	Event
I	+	+	L5, H2, H8
II	+	-	L1, L2, L4, L6, L7, N1, N2
III	-	+	L3, H1, H3, H4, H5
IV	-	-	H6, H7, H9

4.4. Discussion

4.4.1. Comparison between observed and modelled NIWs

This study compared whether the $\text{KE}_{\text{NIW_obs_int}}$ in EC1 was consistent with previously known characteristics of observed and modelled NIWs in the East Sea. The Period High often corresponds to condition of $\zeta < 0$ (Categories III or IV) supporting that NIWs are trapped in a region of $\zeta < 0$ due to the lowered f_{eff} by mesoscale circulations as suggested by previous works, which affected year-to-year varying NIW hot spot (Park and Watts, 2005), and different horizontal and vertical spatial distribution of NIWs based on the subpolar front (Jeon et al., 2019). It has been reported that the instance of NIWs when $\zeta > 0$ corresponding category I or II (Noh and Nam, 2020; Shcherbina et al., 2003), the role of S^2 that increases the NIWs was only considered in Noh and Nam (2020). Since the strong S^2 can exponentially grow wavenumber along the S^2 resulting small group velocity, both ζ and S^2 are considered unlike previous studies that mainly considered ζ . The advantage of considering both ζ and S^2 is found in Category I, showing that even if unfavorable ζ condition, $\text{KE}_{\text{NIW_obs_int}}$ could increase with strong S^2 . With the positive α^2 (corresponding to increased S^2), the NIWs can draw the energy from mesoscale flows via wave capture, since the horizontal stress of NIW and strain of mesoscale fields were coupled (Polzin, 2008; Polzin, 2010). The H2 corresponds to the Events 2–4 in Noh and Nam (2020) explained by the process described above with increased S^2 (Category IV).

The wind-induced NIWs is known to radiate below the MLD (Jeon et al., 2019; Song et al., 2020). However, in spite of large Π , only $\text{KE}_{\text{NIW_model_int}}$ but not $\text{KE}_{\text{NIW_obs_int}}$ was enhanced in many periods such as 19 August 2004 and 3 September

2020 (green triangles in Figure 4.1d) when the typhoon passed by the EC1. This means nonseasonal variations of $KE_{NIW_model_int}$ could not be explained solely by surface wind forcing.

4.4.2. Effects of surface wind forcing on KE_{NIW} below the mixed layer

The role of surface wind forcing was discussed since it is known that the wind-induced NIWs penetrates down below the MLD as they dissipate over time. If the main source of KE_{NIW_obs_int} was surface wind forcing, the timing of the enhanced KE_{NIW_model_int} and events of Period High should be matched (Figures 4.4 and 4.5). The period when the KE_{NIW_model_int} exceeded the $\sigma + \mu$ ($2.5 \times 10^3 \text{ J}^2 \text{ m}^{-6}$) with positive anomaly of Π was H2 and H5. The period when the KE_{NIW_model_int} exceeded over $1.0 \times 10^4 \text{ J}^2 \text{ m}^{-6}$ (e.g., 19 August 2004, and 3 September 2020) was Period Neutral. Indeed, during the period, the wind energy input (cumulative Π) was jumped up to 133 kJ m^{-2} from 121 kJ m^{-2} and 479 kJ m^{-2} from 495 kJ m^{-2} , respectively (green solid line in Figure 4.5c), and the KE_{NIW_obs_int} was not amplified even though the typhoon passed to the left side of EC1 (Figure 4.1). At this time, the wind stress near EC1 rotated clockwise and was sufficient to amplify the NIWs in MLD, but the condition to propagate kinetic energies below the MLD does not appear to be formed. In H2, few to several days after the typhoon Maemi passed by the EC1, KE_{NIW_model_int} were amplified, accounting for the enhanced NIWs observed near and off the coast (Noh and Nam, 2020; Nam and Park, 2013), providing favorable condition for KE_{NIW_obs_int} to increase. In the Period Low, the Π showed negative anomaly (except L6), and the KE_{NIW_model_int} were less than $2.0 \times 10^3 \text{ J}^2 \text{ m}^{-6}$. It suggests that the NIWs in MLD amplified by local wind stress does not have a significant impact on enhancement KE_{NIW_obs_int} at 400 m. It is already known that the wind-induced energies are dissipated in the upper 200 m up to 70–85 % (Furuichi et al., 2008; Zhai et al., 2009). The high KE_{NIW_obs_int} contrast to small KE_{NIW_model_int} (except H2 and

H5) could be explained by the NIWs which were generated at northern region and equatorward and downward propagated. For example, the NIWs originating from high latitude (approximately 38.1 °N) could propagate and reach at 400 m near 37.3 °N (Figure 4.7), the favorable condition for NIWs such as the negative ζ can trap the NIWs. However, considering the $KE_{NIW_model_int}$ calculated by 38–40 °N along the 131 °E averaged wind stress, there was no possibility which propagate from the north to EC1 (Figure. 4.5e). Thus, in this study, the effect of local wind on the NIWs was only considered.

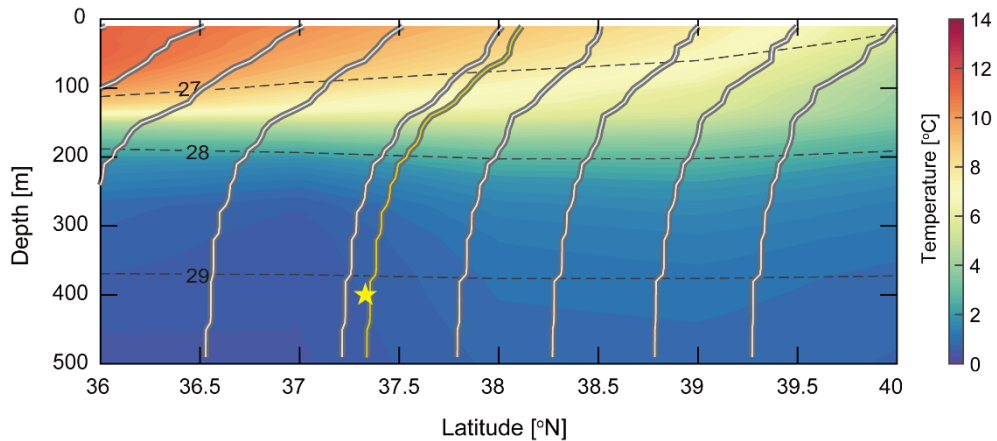


Figure 4.7. Ray path of NIWs (thick white solid line) in the spatially varying stratification in March 2018 corresponding H8. Yellow solid line indicates ray path that can reach a depth of 400 m at EC1 (yellow star). Background color indicates potential temperature, and dashed line indicates potential density.

4.4.3. Effects of mesoscale flow fields on KE_{NIW} below the mixed layer

The negative ζ , and positive α^2 conditions in the Period High (especially Category IV) theoretically support the enhancement of NIWs at 400 m providing favorable conditions for KE_{NIW_obs_int}. First of all, negative ζ (category III and IV) lower f_{eff} permitting the trapping and rapid deep propagation of NIWs (Kunze, 1985; Lee and Niiler, 1998). The horizontal wavenumber of NIW can linearly increase with time proportional to the gradient of f_{eff} . Second, the increased S^2 that simply corresponds to positive α^2 (category I and III) also stretches and rotates the wavevector, then they can change the horizontal wavenumber of NIWs with exponential growth resulting the zero group velocity (Bühler, 2005). Here, two neutral period in which the KE_{NIW_obs_int} was not amplified even though the KE_{NIW_model_int} increased by the typhoon were considered as N1 (August 2004) and N2 (September 2020). During the N1 and N2, the ζ was positive (higher than that in Period Neutral), and the sign of α^2 was negative yielding severe condition (Category II) for enhancing KE_{NIW} at 400 m.

From the classification, the change in KE_{NIW} enhancement condition after H5 was captured, and it could not be detected if only ζ was considered. It implies the variation of mesoscale flow fields affecting the KE_{NIW_obs_int}. In particular, H5 and H6, the UWE appeared in October 2014 and disappeared in August 2016, lasting for nearly two years (Jin et al., 2019). Then, another UWE newly appeared in September 2016 corresponding H7. The growth and movement of UWE could affect the KE_{NIW_obs_int} providing strong negative ζ in the vicinity of the EC1 during H5–H7. The negative ζ and α^2 in H6 and H7 suggest that the role of UWE on

KE_{NIW} was increased. Besides, the N increased with time from 2000 to 2018, yielding the strengthening of the stratification. Then, it abruptly decreased after 2019. It implied a change in the background fields affecting the stratification at 400 m near the EC1, and the N at 400 m was different from that at 50 m (Figure 4.8a). Consequently, the change of N was inversely proportional to the WKB scaling factor that decreased from 2000 to 2018 (Figure 4.8). The N (WKB scaling factor) at 400 m interannually increased (decreased) in 2003, 2006, 2011, 2013, 2015–2018. Considering WKB scaling factor that decreased by 0.1 per decade (Figure 4.8d), KE_{NIW} in the 2010s should decrease by about 19 % compared to that in 2000s, but most of Period High appears in the 2010s. It implies that the increased KE_{NIW} in the 2010s could not be explained solely by N or NIW potential energy but the mesoscale circulations. Also, notable thing is that even if the WKB scaling factor was applied, the currently defined Period High and Period Low did not change (not shown).

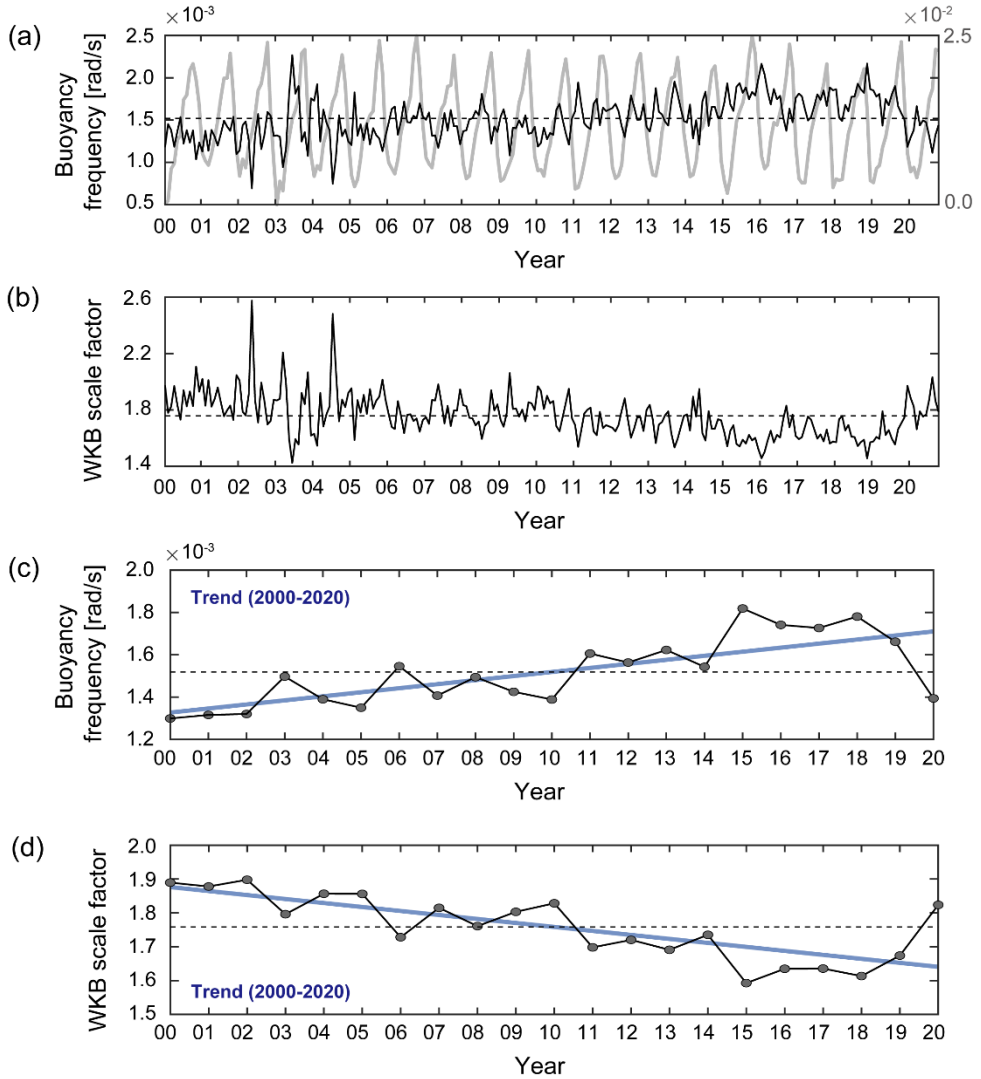


Figure 4.8. Time-series of (a) monthly Buoyancy frequency at 50 m (gray line, right y-axis) and 400 m (black line, left y-axis) derived from EN4, (b) WKB scale factor at 400 m with reference density, $0.0046 \text{ rad s}^{-1}$, (c) and (d) indicate annual mean of (a) and (b). Dashed lines in (a) – (d) indicate temporal mean. Blue thick line in (c) and (d) represent linear trend from 2000 to 2020.

4.5. Conclusion

The nonseasonal variations of KE_{NIW} at 400 m (KE_{NIW_obs_int}) were presented using long time-series observations from subsurface mooring in the southwestern East Sea from 2000 to 2020. Totally 9 periods of high (Period High) and 7 periods of low (Period Low) KE_{NIW_obs_int} at 400 m were identified and analyzed statistically (composite analysis) to reveal significant effects of mesoscale flow fields on the KE_{NIW_obs_int} of the subsurface mooring in the southwestern East Sea. The rate of wind work can increase the KE_{NIW_model_int}, but it could not explain the KE_{NIW_obs_int} alone. The KE_{NIW_obs_int} averaged over each category was high when the mesoscale condition was $\zeta < 0$ or $\alpha^2 > 0$. With the 95 % significance, the negative ζ , and positive α^2 support the increased KE_{NIW} at 400 m (Category IV). These conditions are favorable to NIWs, corresponding the trapping of NIW and wave capture process. On contrary Category V, the positive ζ , and negative α^2 (Category II) prevent the KE_{NIW} at 400 m from increasing. It prevents the amplification of KE_{NIW} at 400m even if there was a large supply of KE_{NIW} in MLD from the typhoon (N1 and N2). This result statistically implied that the KE_{NIW_obs} could be enhanced through nonlinear interaction with mesoscale flow fields as well as trapping by negative ζ . This study firstly attempts to investigate the intraseasonal variations of KE_{NIW} at 400 m for 21 years, and suggests 4 categories depending on the α^2 (included S^2), not only considering ζ . It will provide a better understanding of long-term effects of NIWs on energy transport and mixing in ocean interior, and its relation with climate change. So, further study is needed to examine the variations of mesoscale flow fields since the categories of period High in late 2010s differed from previous one.

5. Nonseasonal variability of semidiurnal kinetic energy from 21-year-long observation

5.1. Introduction

Internal tides (also referred as baroclinic tides) are internal gravity waves that generated as barotropic tidal currents (flow associated with surface tides) interacts with bottom topography in a stratified ocean (Wunsch, 1975; Garrett and Kunze, 2007). Diurnal and semidiurnal internal tides are generated when and where their characteristic slope matches the bottom slope (Baines, 1982), propagate through interaction with mesoscale circulation, and then ultimately dissipate. The global ocean is required energy budget about 2.1 TW to maintain the thermohaline circulation, and the barotropic to baroclinic tide conversion provides half of energy with \sim 1 TW (Munk & Wunsh, 1998; Egbert and Ray, 2000). Internal tides have been studied by satellite altimetry-derived sea surface height (Egbert and Ray, 2000; Morimoto et al., 2000; Zhao, 2018; Zhao, 2019; Carrere et al., 2021), numerical models (Niwa and Hibiya, 2001; Jeon et al., 2014; Ansong et al, 2017; Arbic et al., 2018), and observations (Nash et al., 2004; Park and Watts, 2006; Rainville & Pinkel, 2006). It is known that the 18.613-year cycle caused by the lunar ascending node affects long-term fluctuation of oceanic tides up to 20 % of their amplitude (Doodson, 1927; Loder and Garret, 1978), but long-term variations of the internal tides are still poorly understood.

The internal tides in the East Sea is known to be generated at northern end of the Korea Strait where the bottom slope rapidly changes in continental slope (\sim 200 m water depth near 35.5–35.7 °N and 130–131 °N) (Park and Watts, 2006; Park et al., 2006; Jeon et al., 2014). The diurnal tides are almost trapped in the southern Ulleng

Basin due to their critical latitude, whereas the semidiurnal internal tides (hereafter SDIT), propagate poleward interacting with the mesoscale circulation (Park and Watts, 2006; Nam and Park, 2008). The SDIT entering the Ulleng Basin mostly refract eastward with anticyclonic eddy (called Ulleung Warm Eddy), and westward with existence of cold water near the east coast of Korea or cold eddies along the propagation pathway (Park and Watts, 2006; Nam and Park, 2008; Noh and Nam, 2020). It is known that the SDIT have seasonal variations in barotropic-to-baroclinic conversion with maximum (minimum) in September (March) that induced by seasonal stratification. They can propagate far from the generation site from late summer to early winter (Jeon et al., 2014). Although previous studies have been conducted on the generation, propagation, and seasonal changes of SDIT, their long-term variations including intraseasonal (here, 3–100 days), interannual and decadal variations has been rarely studied in this region.

This study firstly investigates intraseasonal, interannual and decadal variations of SDIT kinetic energy from 21-year-long moored time-series observations in the southwestern East Sea. Based on the statistical analysis, possibility of generation and eastward/westward refraction were discussed with hydrography and sea surface height from satellite altimetry near the SDIT generation site. Data and methods are described in next chapter. In chapter 5.3, results of moored observations are presented. The results on enhanced SDIT in terms of generation and refraction will be discussed in chapter 5.4, and conclude in chapter 5.5.

5.2. Data and Method

5.2.1. Data

Long-term time-series data have been collected from a subsurface mooring, named EC1, located at a water depth of 2300 m since 1996 (Figure 5.1). Details are described in chapter 4.2. To determine the generation condition of SDIT, National Institute of Fisheries Science (NIFS) hydrographic data collected bi-monthly was selected from 2000 to 2020. Hourly sea surface elevation from tidal-gauge at Busan collected by Korea Hydrographic and Oceanographic Agency (KHOA) was used to investigate the barotropic tide. The tidal-gauge at Busan is ~ 320 km southwest of the SDIT generation site (triangle and red hatched area in Figure 5.1), and there were no sudden changes in the topography slope until the tidal currents enters the SDIT generation site where the continental slope exists. Satellite altimetry-derived daily sea surface height (corresponding absolute dynamic topography above geoid, ADT) of gridded level4 data provided by the Copernicus Marine Environment Monitoring Service were used, and their spatial resolution is 0.25° .

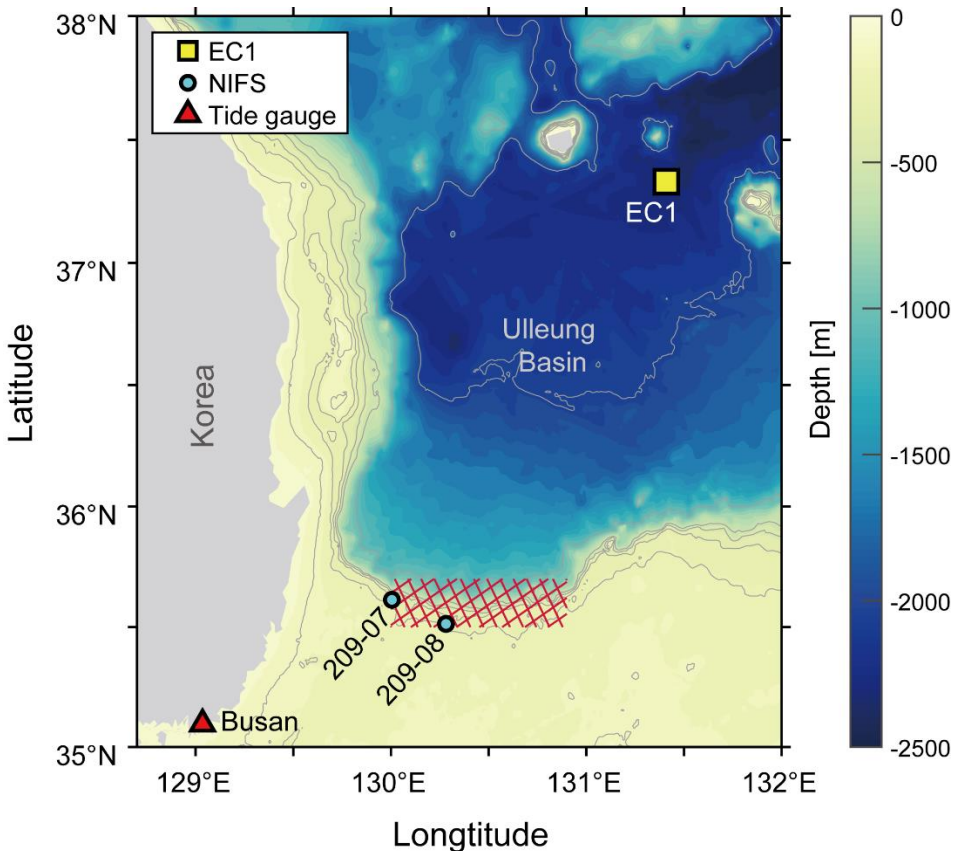


Figure 5.1. Geographic map of the southwestern East Sea with topography (color). Location of subsurface mooring, EC1, is marked by yellow square. The NIFS stations and KHOA tidal gauge are shown by blue circles and red triangle. Red hatched area represents SDIT generation site.

5.2.2. Method

Horizontal currents observed in EC1 were quality controlled by global standard following the instrument types, and then converted to hourly data with ensemble average. Details are described in chapter 4.2. The SDITs (u_{SDIT}, v_{SDIT}) were extracted from (u, v) applying phase-preserved fourth-order Butterworth bandpass filter with cut-off frequencies as $[0.9M_2, 1.1M_2]$ where M_2 is semidiurnal frequency (~ 0.0805 cycle per hour; 12.4 hour). The cut-off frequencies were set to include both M_2 and S_2 signal. Same bandpass filter was applied to sea surface elevation (η) to extract semidiurnal variation of sea surface elevation (η_{SD}). The harmonic analysis was applied to η_{SD} with Unified Tidal analysis and prediction toolbox (UTide), and the 18.6-year nodal factor of M_2 and S_2 was also calculated with this toolbox. The SDIT horizontal kinetic energy (KE_{SDIT}) was computed as $0.5\rho_0(u_{SDIT}^2 + v_{SDIT}^2)$ where ρ_0 is reference density ($= 1025.0 \text{ kg m}^{-3}$). To capture the nonseasonal variation, wavelet analysis was applied to the η_{SD}^2 and KE_{SDIT} (Torrence and Compo, 1998), and then variances in nonseasonal bands (3–100 days) were extracted. The bands were selected as including lunisolar fortnight (~ 14 days) and lunar monthly cycles (29.5 days for synodic month and 27.5 days for sidereal month). High KE_{SDIT} periods (Period High, 10th percentile) were defined as the criterion exceeding 1 standard deviation (0.10) from the mean (0.08) of the nonseasonal KE_{SDIT} normalized to the maximum over the period. Events for low KE_{SDIT} were selected to match the number of event days (624 days) same as that of Period High after sorting KE_{SDIT} in order of magnitude, and the rest of periods were defined as Period Neutral (between 10th and 90th percentiles).

The sequential *t*-test analysis of regime shifts (STARS) by Rodionov (2006) was

applied to determine regime shift in the annual mean of η_{SD}^2 and nonseasonal KE_{SDIT}.

The changes in the confidence of shifts was detected with cut-of length 10 that is the time scale for detecting the regime, and 90 % probability level (Rodionov, 2006).

The buoyancy frequency, $N = \{-(g/\rho_0)/(d\rho/dz)\}^{1/2}$, was calculated with vertically 1-m linear interpolated NIFS temperature profiles and fixed salinity value 34 psu where z , t , N_0 , g , and ρ are the vertical coordinate, time, reference buoyancy frequency. Here, the temperature profiles were quality controlled following global and regional rage test, spike test, and density inversion test (Bhaskar et al., 2011).

The characteristic slope of internal waves was calculated as $\gamma = \pm\sqrt{(\omega^2 - f^2)/(N^2 - \omega^2)}$ where wave frequency ω is set to M_2 to compare the characteristic slope of SDITs with the bottom slope at the shelf break in the north of the Korea Strait. Here, the bottom slope (s) at 200 m was set to 0.01 (Park and Watts, 2006; Nam and Park, 2008; Noh and Nam, 2020). The SDIT generation condition at 200 m was determined by $|\gamma - s| < 0.01$. Then, four conditions were defined whether the SDIT was formed at the northern end of the Korea Strait and whether there was a possibility for westward or eastward refraction. The generation conditions were estimated using NIFS hydrographic data collected from 209-08 station at 175 and 200 m. Herein, the refraction conditions were that the difference of ADT: $\Delta\text{ADT} = \text{ADT}_{130E} - \text{ADT}_{131E}$. When the ADT in the western side is higher than in the eastern side, the ΔADT shows a positive value implying possibility of eastward refraction toward mooring site. The ΔADT was compared with steric height anomalies that was calculated from NIFS temperature profiles at 209-07 and 209-08 stations using the Gibbs SeaWater toolbox of TEOS-10. The reference depth was set to 200 m which was maximum observed depth for both stations.

5.3. Result

5.3.1. Nonseasonal variations of KE_{SDIT} and η_{SD}^2

The KE_{SDIT} at 400 m showed strong variations at ~14, 28, and 56 days, whereas the η_{SD}^2 showed dominant fluctuations peaked at ~15 and 26 days (Figure 5.2a and 5.2b). In the η_{SD}^2 , the variations were mostly distributed near the fortnight cycle, and about 33% of fortnight variation appeared at 26 days. In the intraseasonal band, the KE_{SDIT} of each peak averaged over whole time was similar to each other, and low frequency signal (~56 days) that was not in η_{SD}^2 was found. The averaged KE_{SDIT} in Period High, Period Neutral, and Period Low were 6.47×10^{-3} , 1.3×10^{-3} and 0.2×10^{-3} ($J\ m^{-3}$)², and those at Period High and Period Low was significant ($p < 0.05$) comparing to Period Neutral. The maximum KE_{SDIT} was found in March 2013 with 21.1×10^{-3} ($J\ m^{-3}$)², the second largest KE_{SDIT} was found in January 2016 with 16.8×10^{-3} ($J\ m^{-3}$)². There was a significant increase ($> 2.0 \times 10^{-3}$ ($J\ m^{-3}$)²) in particular years such as 2003, 2012, 2013, 2014, and 2016 (Figure 5.2c and Table 5.1)

The annual mean of intraseasonal KE_{SDIT} showed a minimum in 2009 and a maximum in 2016, and it was fluctuated about 3~5 years (e.g., 2003, 2007, 2012, and 2016) (Figure 5.2d and Table 5.1). The year of minimum was same as annual mean of KE_{SDIT} (2009), but not for maximum (2015). The annual mean of η_{SD}^2 did not show any 3~5 years fluctuation (Figure 5.3). Based on 2011/2012, the mean value of annual mean η_{SD}^2 and KE_{SDIT} was shifted with increase of mean 3.2×10^{-3} to 3.8×10^{-3} m^2 and 1.1×10^{-3} to 2.3×10^{-3} ($J\ m^{-3}$)², which was about 1.2 times and 2 times larger than the former in 95 % significance level (red thick line in figure 2d). In the annual variations, correlation coefficients between KE_{SDIT} and η_{SD}^2 was

0.69 with 95 % significance. Period High mostly appeared in 2010s excluding 2003 and 2004, and Period Low was distributed in the 2000s with the most frequency Period Low in 2009 (Figure 5.2c).

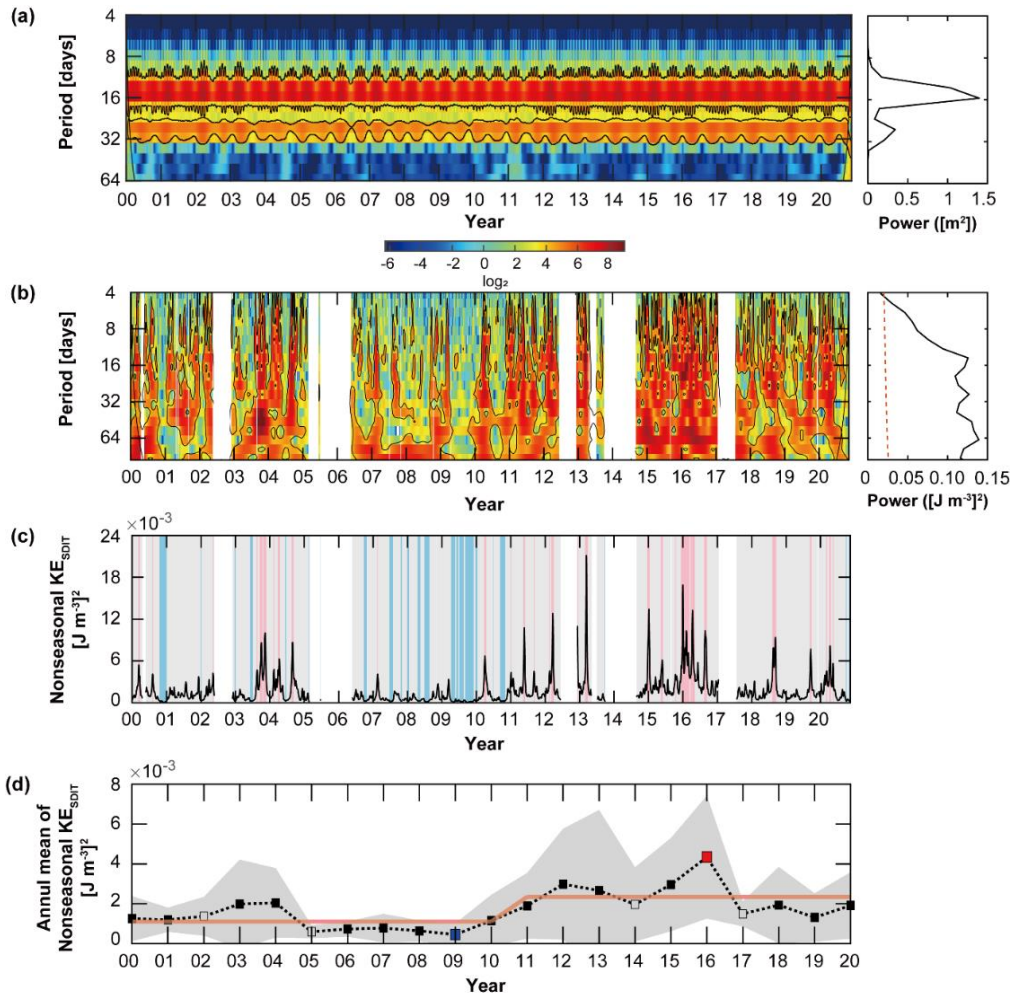


Figure 5.2. Wavelet power spectrum and global power spectrum of (a) η_{SD}^2 at Busan and (b) KESDIT at 400 m. Time series of (c) intraseasonal KESDIT averaged (b) for 3~100 days band. In (c), Red (blue) shaded area indicate Period High (Period Low). Gray shaded area indicates Period Neutral. In (b) and (c), white area represents data gap (no available data). (d) Annual mean of (c) with standard deviation (gray shading). Red thick line in (d) indicate mean over the period that detected by STARS.

Table 5.1. Annual mean of nonseasonal KE_{SDIT} at 400 m and data acquisition rate in each year.

Year	Mean ($\times 10^{-4}$ (J m $^{-2}$) 2)	Data acquisition (percentage)	Year	Mean ($\times 10^{-4}$ (J m $^{-2}$) 2)	Data acquisition (percentage)
2000	12.50	90	2011	18.96	100
2001	11.98	98	2012	29.84	52
2002	13.70	47	2013	26.62	55
2003	19.86	99	2014	19.68	34
2004	20.42	100	2015	29.61	98
2005	5.93	18	2016	43.40	100
2006	7.34	61	2017	14.94	48
2007	7.79	98	2018	19.33	100
2008	6.37	99	2019	13.12	97
2009	4.52	99	2020	19.14	86
2010	11.52	100			

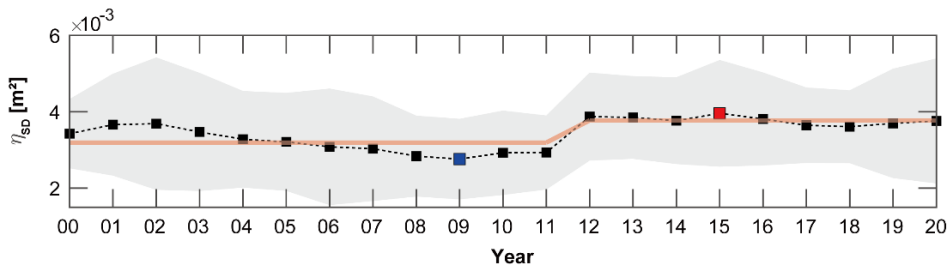


Figure 5.3. Annual mean of η^2_{SD} in 3–100 days band. Red line indicates mean values during the periods that detected by STARS. Gray shading indicates standard deviation. Red and blue square markers represent maximum and minimum.

5.4. Discussion

5.4.1. Surface tidal forcing

Although the barotropic tides is 10 times smaller than that of adjacent Yellow Sea and East China Sea, it is known that the semidiurnal M_2 tide is dominant in the Korea Strait (Morimoto et al., 2000; Park et al., 2006). The M_2 and S_2 occupied 71.9 and 16.1 % in η_{SD} , and dominant η_{SD}^2 (as a surface tide) period is related to fortnight cycle (or spring-neap, ~ 14 days) and sidereal month (or lunar month, ~27 days), yielding that the semidiurnal tides are dominant rather than diurnal tides following the previous studies. Since this study dealt with 21-year-long time series data, the 18.6-year (bi-decadal) nodal modulation should be considered. Considering the nodal factor (not nodal phase), the M_2 and S_2 can be modulated up to 2 % and 0.2 % (Figure 5.4), this is contrast to diurnal (K_1 , O_1) constituents that can be modulated by nodal factor up to 10~20 %. The M_2 nodal factor anomaly with a reference value of 1 changed its sign in year of 2000 and 2011, and the annual mean of η_{SD}^2 experienced the shift in 2011/2012 as mentioned in chapter 5.3. Although the SDIT modulation by the nodal facto is small, it implies that the 18.6-year cycle has an effect on the shift of η_{SD}^2 mean value. Since the annual mean of KE_{SDIT} also experienced shift in 2011/2012 and significant correlation coefficient (~0.69) between annual η_{SDIT}^2 and KE_{SDIT} , the decadal variation of KE_{SDIT} is also related to the surface tidal forcing (η_{SDIT}^2). However, unlike the fact that annual mean KE_{SDIT} increased in 2003, 2004, and 2016, η_{SD}^2 did not amplified (Figures 5.2d and 5.3), and η_{SD}^2 was suddenly increased in 2011/2012 whereas the nodal factors change sinusoidal. Thus, even with surface tidal forcing, it is hard to explain KE_{SDIT} if the

conditions for SDIT generation and refraction toward mooring site are not met. Thus, the conditions for generation and refraction will be discussed.

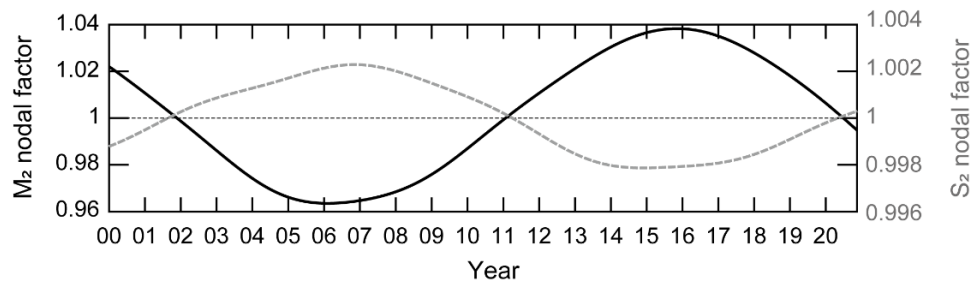


Figure 5.4. Nodal factor for M2 (left y-axis) and S2 (right y-axis) near the tidal-gauge station.

5.4.2. Conditions for SDIT generation

For past 21 year, the SDIT was generated at the northern end of the Korea Strait with a 65% probability (set to $|\gamma - s| < 0.01$, $s=0.01$), and the KE_{SDIT} at 400 m was significantly increased about 1.6 times higher ($\sim 20.9 \times 10^{-4}$ ($J\ m^{-3}$)²) compared to the non-generated condition ($\sim 13.4 \times 10^{-4}$ ($J\ m^{-3}$)²) with 95 % significance. Since the SDIT generation is affected by N and s , statistically significant N and s were selected by considering s that can come from N at 175 and 200 m and s at the Korea Strait (Figure 5.5). A statistically significant difference in N between the Period High and Period Low appeared when the N at 200 m was selected. Here, the M_2 frequency was selected for γ calculation, but it can make an error of γ as order of magnitude about $O(\sim 10^{-3})$ comparing the characteristic slope using M_2 and S_2 frequencies. The composited $|\gamma - s|$ during the Period High, Period Neutral, and Period Low was not significant, yielding increased KE_{SDIT} at EC1 is hard to explain by $|\gamma - s|$ solely. Annual mean of N had a maximum (minimum) in year of 2004 (2019), and annual mean of γ showed a maximum (minimum) in year of 2000 (2004) (Figures 5.5e and 5.5f). Stratification strengthened in 2004 could be favorable for SDIT generation and may be related to the increase in KE_{SDIT} in 2004. However, it was difficult to link with KE_{SDIT} in annual mean N and γ , and no shift of annual mean was found in the decadal variations.

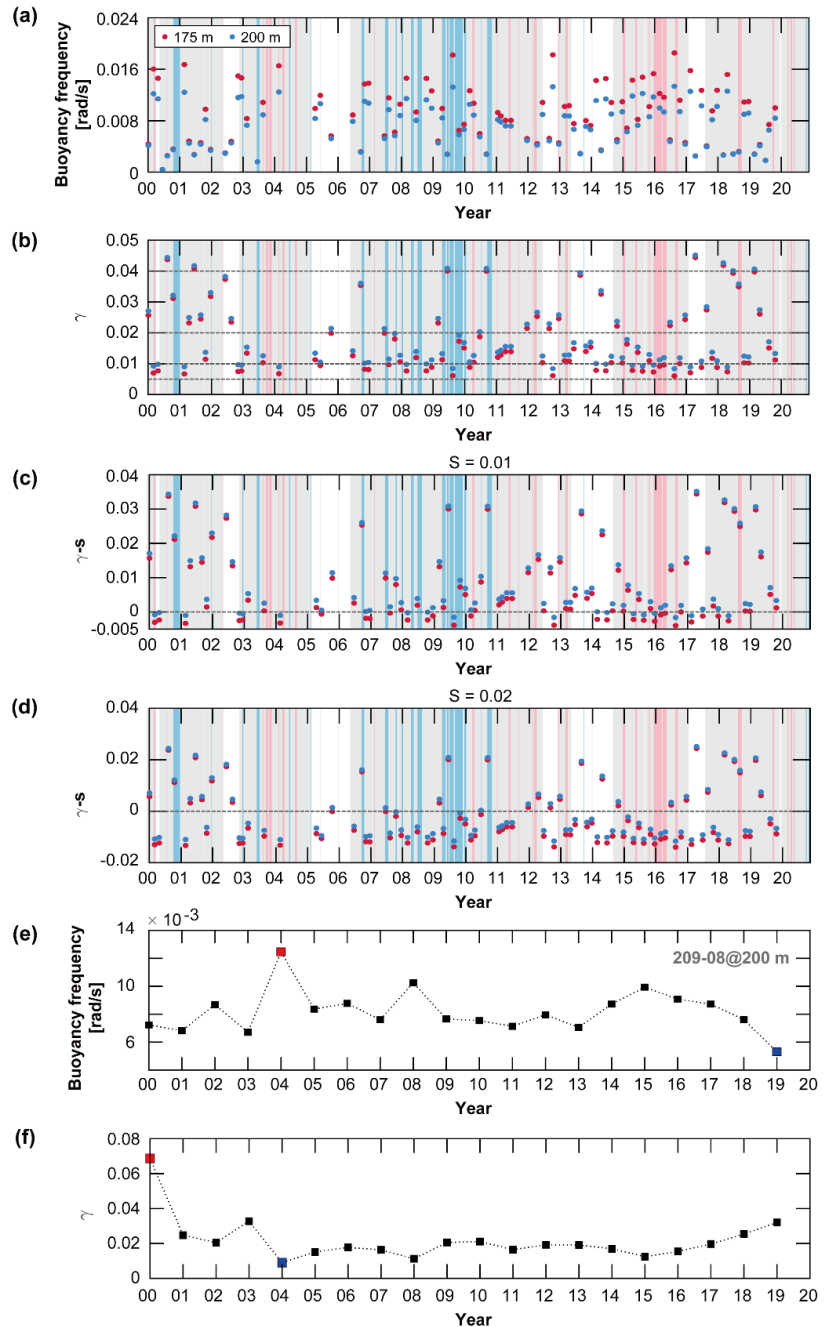


Figure 5.5. Time-series of (a) buoyancy frequency at 175 and 200 m in 209-08 station, (b) γ , (c)–(d) $\gamma - s$, (e) annual mean of (a), and (f) annual mean of (b). In (b), dashed lines represent possible topographic slope (s) near the SDIT generation site. In (a)–(d), red (blue) shaded area indicate Period High (Period Low). Gray shaded area indicates Period Neutral. White area represents data gap (no available data).

5.4.3. Conditions for SDIT refraction

Even if the SDIT is generated, their propagation can be modulated by background circulation along their pathways (Park and Watts, 2006; Jeon et al., 2014). The generated SDIT had a northeastward refraction with 61 % probability and northwestward refraction with 39 % probability from the composite of each cases (Figure 5.6 and Table 5.2). For the Period High, Period Neutral, and Period Low, the composited ΔADT was 0.005, 0.004, and 0.000, and it was statistically significant supporting the eastward refraction during Period High.

From the Case classification, Case 1 showed the highest KE_{SDIT} ($\sim 22.0 \times 10^{-4} (\text{J m}^{-3})^2$) compared to Case 3 under the 95 % significance, but there was no significance between Case 1 and Case 2 corresponding refraction direction. Also, Cases 3 and 4 had no significant difference implying the refraction condition at the northern slope of Korea Strait is not sufficient to diagnose the increased KE_{SDIT} at 400 m. Although Cases 1 and 4 were opposite for generation and refraction condition, there was no statistically significant difference, which was due to the amplified KE_{SDIT} in Case 4 in August 2018. Excluding this period, comparing Cases 1 and 4 again revealed that there was a statistically significant difference. The reason that August 2018 was classified as Case 4 despite the high KE_{SDIT} was due to the negative ΔADT (Figure 5.5). However, the steric height anomaly observed in March 2018 was positive, applying this condition, this period is changed to Case 3. It implies that if $|\gamma - s|$ and ΔADT in the SDIT generation site are known, the SDIT propagation could be discriminated with ~65 % probability. The monthly average KE_{SDIT} at 400 m for 21-year showed a minimum in July and then gradually increased, showed a maximum in March, and then decreased again (not shown). It is similar to the

previous study that SDIT can propagate far from the generation site from late summer to early winter (Jeon et al., 2014). During the Period High, Period Natural, and Period Low, $|\gamma - s|$ was 0.005, 0.015, 0.002, but only Period High was statistically significant compared to Period Neutral. It means that the SDIT propagation toward the EC1 can be estimated with the conditions in the SDIT generating area, but the generation and refraction of SDIT cannot be determined by the amount of KE_{SDIT} in the EC1. This is because the SDIT is modulated by the background circulations as it propagates (Park and Watts, 2006).

In Cases 1 and 3, the ADT in the western side appeared slightly higher than that in the eastern side suggesting eastward refraction, and the presence of UWE in the SDIT propagation path enables refraction toward EC1 (Figure 5.7, also see Figure 8d in Park and Watts, 2006). Case2 showed little difference in ADT in SDIT generation site suggesting weak propagation of SDIT, and UWE located near EC1 was thought to have played a role in western refraction such as Figure 8c in Park and Watts (2006). Case 4 is hard to generate the SDIT and with the northeastward flowing Tsushima Warm Currents, the high ADT appeared in the southeastern part of East Sea yielding western refraction condition.

As mentioned in chapter 5.3, interannual variations of KE_{SDIT} changed at 2011/2012, and the background circulation field was also different at this time (Figure 5.8). Before 2012, the background fields were similar to case 4, and after 2012, the that was similar to case 1. In statistics, after year of 2012, the KE_{SDIT} increased by almost two times compared to that of before 2012, and the difference in ADT was also increased. Besides, the $|\gamma - s|$ before 2012 was 0.015 indicating unfavorable condition for SDIT generation, after 2012, it was decreased to 0.010 showing favorable condition for SDIT generation. The difference between before

2012 and after 2012 among the conditions for generation and refraction, and KE_{SDIT} were significant at 95% confidence, suggesting that the η_{SD} that might be modulated by 18-year nodal factor, stratification near the generation site and mesoscale circulations in the interior of the East Sea had a significant effect on the KE_{SDIT} increase in the EC1. This suggests that the change in KE_{SDIT} at 400 m has influenced or might have influenced the East Sea circulation.

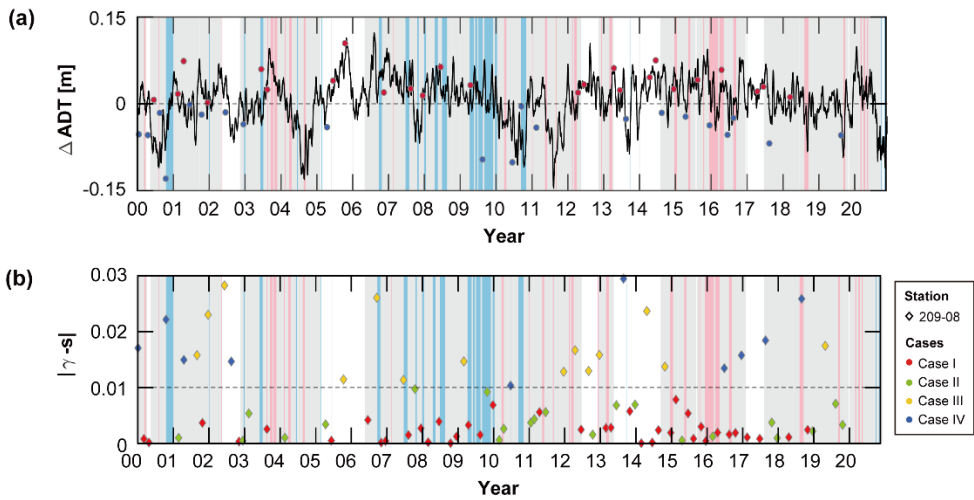


Figure 5.6. Time-series of (a) ΔADT and (b) $|\gamma - s|$. In (a), positive value means the possibility of eastward refraction, and vice versa. In (a), red and blue circles represent positive and negative steric height anomaly between 209-07 and 209-08 station. In (b), dotted line indicates the threshold with 0.01. Red (blue) shaded area indicate Period High (Period Low). Gray shaded area indicates Period Neutral. White area represents data gap (no available data).

Table 5.2. Cases depending on generation and refraction conditions, and KE_{SDIT} and $|\gamma - s|$ averaged over the cases. In table, Y, N, E, and W are acronyms of Yes, No, Eastward, and Westward. Condition for SDIT generation was determined by 209-08 station

Generation	Refraction	Nonseasonal		$ \gamma - s $	Data number
		KE _{SDIT} ($\times 10^{-4} \text{ J m}^{-3}$) ²)			
Case 1	Y	E	22.0	0.002	39
Case 2	Y	W	19.1	0.004	22
Case 3	N	E	10.4	0.023	20
Case 4	N	W	16.5 (12.9)	0.041	15 (14)

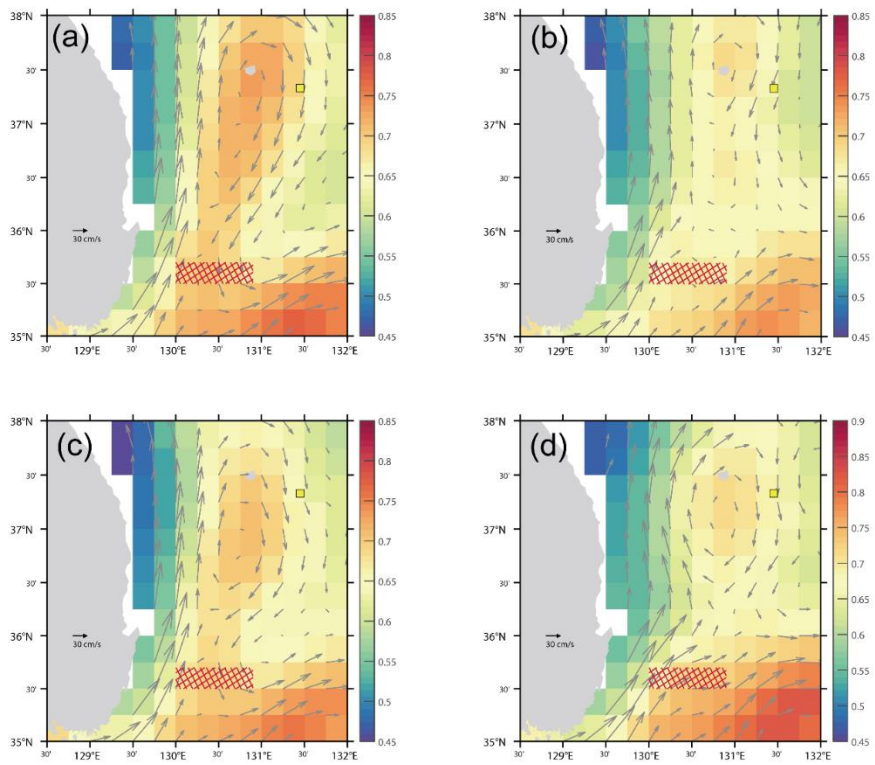


Figure 5.7. Composite maps of ADT (color shading, unit: m) and satellite altimetry-derived geostrophic currents (gray vectors) for (a) Case 1, (b) Case 2, (c) Case 3, and (d) Case 4. The yellow square indicates the EC1, and red hatched area represent SDIT generation site.

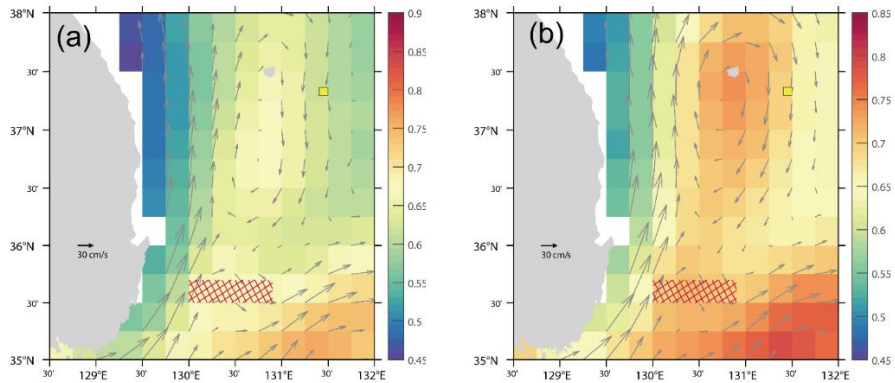


Figure 5.8. Same as Figure 5.5, but for (a) before 2011, and (b) after 2011.

5.5. Conclusion

Nonseasonal variations of KE_{SDIT} at 400 m were investigated using 21-year-long time-series moored observations in the southwestern East Sea from 2000 to 2020. The η_{SD} , ~300 km away from the SDIT generation site (correspond to northern end of Korea Strait), had fortnight and lunar month variations, and the variations of KE_{SDIT} had another low frequency peak at 56 days. Due to the long-term observation period, the M₂ and S₂ nodal factor can modulate the semidiurnal internal tides up to 2 %, and M₂ nodal factor anomaly changed in 2011/2012. Decadal variation of KE_{SDIT} showed the regime shift in 2011/2012 with increasing of the mean energy, and same as η_{SD} . Based on the statistics, the possibility of SDIT which were generated and propagated northeastward was ~64 % with high KE_{SDIT} at EC1. The conditions for the generation and refraction near the generation site were statistically significant to determine the KE_{SDIT} that reached toward EC1. On the other hand, there was no significant difference among the generation and refraction conditions during Period High, Period Neutral and Period Low. It is because the SDIT was modulated by a background circulation such as mesoscale eddy while propagating. The cell structure of ES MOC was different in the 2000s and 2010s implying different circulation pattern that affects SDIT propagation (Han et al., 2020). Besides, the UWE, which was generated in October 2014, is known to have lasted for more than two years in the Ulleung Basin (Jin et al., 2019). In the global ocean, there have been many previous studies on long-term variations of SDIT using satellite altimetry data. But, the long-term variation of SDIT including nonseasonal, interannual, and decadal time scales have been rarely studied. This result highlights the nonseasonal variations of KE_{SDIT} at 400 m (intermediate depth) and conditions for generation and

refraction with statistical analysis. It provides the insight to interaction between SDIT and mesoscale circulation beyond the seasonal variations.

6. Conclusion

The episodic and nonseasonal variations including intraseasonal, interannual and decadal timescales of NIWs and SDITs are investigated using 21-year-long moored time-series data in the southwestern East Sea. The NIWs or SDITs interacting with mesoscale flow fields and themselves caused the enhancements of CFW, and the observations on CFW enhancements was first time in the region. The schematic depicts the impact of the mesoscale circulation on enhanced internal waves from near-inertial to buoyancy frequencies in several different ways. The NIWs are well generated when the surface wind forcing persisted close to inertial period with clockwise rotation, and it allows the wind-current resonance in Northern Hemisphere. When the total strain exceeds relative vorticity and rates of energy transfer is positive, potentially evident and efficient energy transfer from mesoscale field to internal waves via wave capture accounted for enhanced NIW.

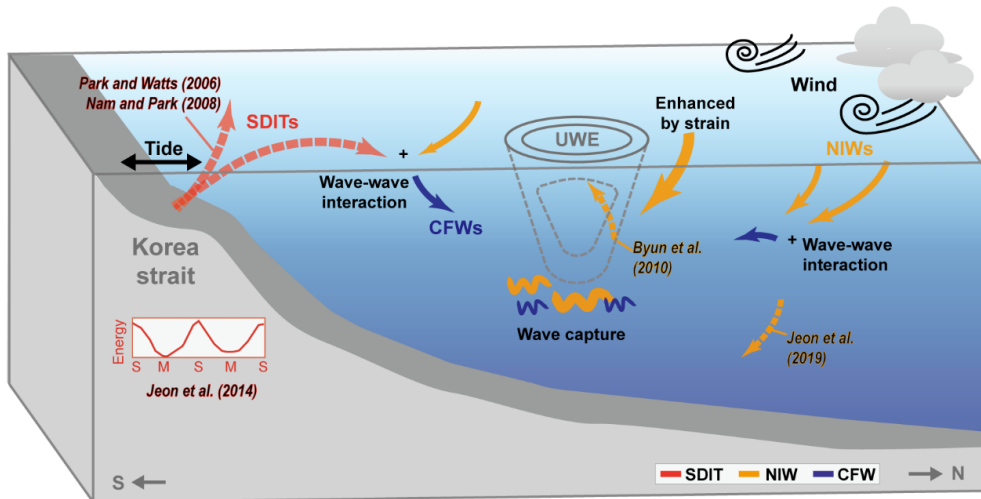


Figure 6.1. Schematic illustration of mechanisms underlying observed enhancements of internal waves in the southwestern East Sea. The SDIT, NIWs, and CFWs are shown in red, orange, and blue, respectively. The mechanisms relevant to observed enhancements of internal waves discussed in this (solid arrows) and previous (dashed arrows with colored label) studies (Park and Watts, 2006; Nam and Park, 2008; Byun et al., 2010; Jeon et al., 2014; 2019).

Remarkable time-depth variations of SDITs in addition to noticeable spring-neap tide cycles were found largely following mesoscale conditions favourable for generating the SDITs at the shelf break in the north of the Korea Strait and eastward refracting of the poleward propagating SDITs toward the observation site in the northern Ulleung Basin. It was revealed that the generated SDIT refracted northeastward with 61 % probability and northwestward with 39 % probability from the composite analysis. With the background conditions for SDIT generation and refraction at the northern slope of the Korea Strait, the variations of semidiurnal kinetic energy toward the observation site could be guessed. But, due to the modulation of SDIT interacting with mesoscale background flows, the generation and propagation at the SDIT generation site cannot be inferred from observed SDIT kinetic energies at the EC1.

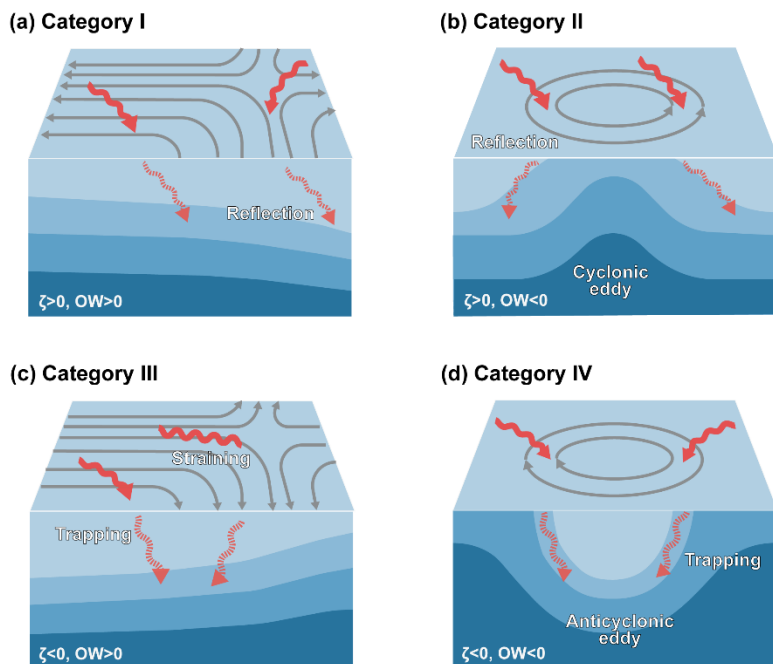


Figure 6.2. Schematics for (a) Category I, (b) Category II, (c) Category III, and (d) Category IV.

Nonseasonal variations in NIW kinetic energies can be diagnose by four categories through mesoscale conditions such as relative vorticity and Okubo-Weiss parameter. This is because the NIW trapping and exponential change of wavenumber due to straining can be inferred from the background field.

Importance of local and remote wave-wave interaction processes and forward energy cascading from NIWs and SDITs into CFWs was emphasised to account for time-depth patterns of KE_{CFW} and the frequency spectrum of horizontal kinetic energy. The observation reveals that CFWs and forward energy cascading from low-to high-frequency internal waves are enhanced not only by direct local and remote wind forcing or by remote tidal forcing, but also through remarkable interactions among the internal waves, and with the mesoscale field via wave capture (Doppler shift of NIWs) and wave guide (refraction of SDITs). The results support previous works, which consistently show that 1) the NIWs are affected by mesoscale strain and vorticity (Kunze, 1985; Buhler and McIntyre, 2005; Polzin, 2008; 2010, Whitt and Thomas, 2015; Jing et al., 2017; 2018), 2) ITs are either refracted or trapped by the background fields (Kim et al., 2005; Park and Watts, 2006; Nam and Park, 2008; Jeon et al., 2014; Seo et al., 2016), and 3) NIWs and SDITs significantly interact to shape the CFWs via forward energy cascading (Garrett and Munk, 1975; Hibiya et al., 2002; Alford, 2003; Alford et al., 2017; MacKinnon et al., 2017; Whalen et al., 2020)

References

- Alford, M. H. (2003) Redistribution of energy available for ocean mixing. *Nature*. 428, 159-62, 2003 W0018 21, 159–163.
- Alford, M. H., MacKinnon, J. A., Simmons, H. L. & Nash, J. D. (2016) Near-Inertial Internal Gravity Waves in the Ocean. *Ann. Rev. Mar. Sci.* 8, 95–123.
- Alford, M. H., Sloyan, B. M. & Simmons, H. L. (2017) Internal Waves in the East Australian Current. *Geophys. Res. Lett.* 44, 12,280-12,288.
- Ansong, J. K., Arbic, B. K., Alford, M. H., Buijsman, M. C., Shriver, J. F., Zhao, Z., ... & Zamudio, L. (2017). Semidiurnal internal tide energy fluxes and their variability in a global ocean model and moored observations. *Journal of Geophysical Research: Oceans*, 122(3), 1882-1900.
- Arbic, B. K., Alford, M. H., Ansong, J. K., Buijsman, M. C., Ciotti, R. B., Farrar, J. T., ... & Zhao, Z. (2018). Primer on global internal tide and internal gravity wave continuum modeling in HYCOM and MITgcm. *New frontiers in operational oceanography*, 307-392.
- Baines, P. G. (1982) On internal tide generation models. *Deep Sea Res. Part A, Oceanogr. Res. Pap.* 29, 307–338.
- Blaker, A. T., Hirschi, J. J., Sinha, B., De Cuevas, B., Alderson, S., Coward, A., & Madec, G. (2012). Large near-inertial oscillations of the Atlantic meridional overturning circulation. *Ocean Modelling*, 42, 50-56.
- Bühler, O. & McIntyre, M. E. (2005) Wave capture and wave-vortex duality. *J. Fluid Mech.* 534, 67–95.
- Byun, S. S., Park, J. J., Chang, K. Il & Schmitt, R. W. (2010) Observation of near-inertial wave reflections within the thermostad layer of an anticyclonic mesoscale eddy. *Geophys. Res. Lett.* 37, 1–6.
- Carrere, L., Arbic, B. K., Dushaw, B., Egbert, G., Erofeeva, S., Lyard, F., ... & Picot, N. (2021). Accuracy assessment of global internal-tide models using satellite altimetry. *Ocean Science*, 17(1), 147-180.
- Chang, K. -I., Teague, W. J., Lyu, S. J., Perkins, H. T., Lee, D. -K., Watts, D. R., Kim, Y. -B., Mitchell, D. A., Lee, C. M. and Kim, K. (2004). Circulation and currents in the southwestern East/Japan Sea: Overview and review, *Progr. Oceanogr.*, 61, pp. 105–156.
- Chelton, D. B., DeSzoeke, R. A., Schlax, M. G., El Naggar, K., & Siwertz, N. (1998). Geographical variability of the first baroclinic Rossby radius of deformation. *Journal of Physical Oceanography*, 28(3), 433-460.
- Chen, S., Hu, J. and Polton, J. A. (2015). Features of near-inertial motions observed on the northern South China Sea shelf during the passage of two typhoons. *Acta Oceanologica Sinica*, 34(1), 38-43.
- Chiswell, S. M. (2003). Deep equatorward propagation of inertial oscillations. *Geophysical research letters*, 30(10).
- Clément, L., Frajka-Williams, E., Sheen, K. L., Bearley, J. A. & Naveira Garabato, A. C. (2016) Generation of internal waves by eddies impinging on the western boundary of the North Atlantic. *J. Phys. Oceanogr.* 46, 1067–1079.

- Crawford, G. B., & Large, W. G. (1996). A numerical investigation of resonant inertial response of the ocean to wind forcing. *Journal of physical oceanography*, 26(6), 873-891.
- Danioux, E., Klein, P., & Rivière, P. (2008). Propagation of wind energy into the deep ocean through a fully turbulent mesoscale eddy field. *Journal of Physical Oceanography*, 38(10), 2224-2241.
- Danioux, E. et al. (2011) Emergence of wind-driven near-inertial waves in the deep ocean triggered by small-scale eddy vorticity structures. *J. Phys. Oceanogr.* 41, 1297–1307.
- Danioux, E., Vanneste, J., & Bühler, O. (2015). On the concentration of near-inertial waves in anticyclones. *arXiv preprint arXiv:1503.00551*.
- D'Asaro, E. A. (1985) The energy flux from the wind to near-inertial motions in the surface mixed layer. *J. Phys. Ocean.* 15, 1043–1059.
- Doodson, A.T. (2016). The harmonic development of the tide-generating potential, *Proc. R. Soc. London, Ser. A.* 100, 305-239
- de Boyer Montégut, C., Madec, G., Fischer, A. S., Lazar, A. and Iudicone, D. (2004). Mixed layer depth over the global ocean: An examination of profile data and a profile-based climatology. *J. Geophys. Res.*, 109, C12003, doi:10.1029/2004JC002378.
- Dunphy, M. & Lamb, K. G. (2014) Focusing and vertical mode scattering of the first mode internal tide by mesoscale eddy interaction. *J. Geophys. Res. Ocean.* 119, 523–536.
- Eden, C., & Greatbatch, R. J. (2008). Towards a mesoscale eddy closure. *Ocean Modelling*, 20(3), 223-239.
- Egbert, G. D., & Ray, R. D. (2000). Significant dissipation of tidal energy in the deep ocean inferred from satellite altimeter data. *Nature*, 405(6788), 775-778.
- Elipot, S., Lumpkin, R. & Prieto, G. (2010) Modification of inertial oscillations by the mesoscale eddy field. *J. Geophys. Res. Ocean.* 115, 1–20.
- Faghmous, J. H., Frenger, I., Yao, Y., Warmka, R., Lindell, A., & Kumar, V. (2015). A daily global mesoscale ocean eddy dataset from satellite altimetry. *Scientific data*, 2(1), 1-16.
- Federiuk, J., & Allen, J. S. (1996). Model studies of near-inertial waves in flow over the Oregon continental shelf. *Journal of physical oceanography*, 26(10), 2053-2075.
- Ferrari, R. & Wunsch, C. (2009) Ocean circulation kinetic energy: reservoirs, sources, and sinks. *Annu. Rev. Fluid Mech.* 41, 253–282.
- Furuichi, N., Hibiya, T., & Niwa, Y. (2008). Model-predicted distribution of wind-induced internal wave energy in the world's oceans. *Journal of Geophysical Research: Oceans*, 113(C9).
- Garrett, C. & Munk, W. (1975) Space-Time scales of internal waves: a progress report. *J. Geophys. Res.* 80, 291–297.
- Garrett, C. J. R. & Munk, W. (1979) Internal waves in the ocean: a progress report. *Ann. Rev. Fluid Mech.* 11, 339–369.
- Garrett, C. (2001) What is the ‘Near-inertial’ band and why is it different from the

- rest of the internal wave spectrum? *J. Phys. Oceanogr.* 31, 962–971.
- Garrett, C. & Kunze, E. (2007) Internal Tide Generation in the Deep Ocean. *Annu. Rev. Fluid Mech.* 39, 57–87. 16.
- Good, S. A., Martin, M. J. and Rayner, N. A. (2013). EN4: Quality controlled ocean temperature and salinity profiles and monthly objective analyses with uncertainty estimates, *J. Geophys. Res. Oceans*, 118, pp. 6704– 6716, doi:10.1002/2013JC009067.
- Han, M., Cho, Y. K., Kang, H. W., & Nam, S. (2020). Decadal changes in meridional overturning circulation in the East Sea (Sea of Japan). *Journal of Physical Oceanography*, 50(6), 1773-1791.
- Hibiya, T., Nagasawa, M. & Niwa, Y. (2002) Nonlinear energy transfer within the oceanic internal wave spectrum at mid and high latitudes. *J. Geophys. Res. C Ocean*. 107, 28–1.
- Hibiya, T., Ijichi, T. & Robertson, R. (2017) The impacts of ocean bottom roughness and tidal flow amplitude on abyssal mixing. *J. Geophys. Res. Ocean*. 122, 5645–5651.
- Huangfu, J., Huang, R., & Chen, W. (2017). Relationship between the South China Sea summer monsoon onset and tropical cyclone genesis over the western North Pacific. *International Journal of Climatology*, 37(15), 5206-5210.
- Ichiye, T., & Takano, K. (1988). Mesoscale eddies in the Japan Sea. *La mer*, 26(2), 69-75.
- Jang, H. Y., & Yeh, S. W. (2013). Analysis of Atmosphere-Ocean Interactions over South China Sea and its Relationship with Northeast Asian Precipitation Variability during Summer. *Atmosphere*, 23(3), 283-291.
- Japan Meteorological Agency. (2015). Annual report on the activities of the RSMC Tokyo – Typhoon center 2015
- Jeon, C. et al. (2014) Seasonal variation of semidiurnal internal tides in the East/Japan Sea. *J. Geophys. Res. Ocean*. 119, 2843–2859.
- Jeon, C., Park, J. H. & Park, Y. G. (2019) Temporal and spatial variability of near-inertial waves in the East/Japan Sea from a high-resolution wind-forced ocean model. *J. Geophys. Res. Ocean*. 124, 6015–6029.
- Jiang, J., Lu, Y. and Perrie, W. (2005) Estimating the energy flux from the wind to ocean inertial motions: The sensitivity to surface wind fields. *Geophysical research letters*, 32(15).
- Jin, H., Park, Y. G., Pak, G. and Kim, Y. H. (2019). On the Persistence of Warm Eddies in the East Sea. *The Sea*, 24(2), 318-331.
- Jing, Z., Wu, L. & Ma, X. (2017) Energy exchange between the mesoscale oceanic eddies and wind-forced near-inertial oscillations. *J. Phys. Oceanogr.* 47, 721–733.
- Jing, Z., Chang, P., Dimarco, S. F. & Wu, L. (2018) Observed energy exchange between low-frequency flows and internal waves in the Gulf of Mexico. *J. Phys. Oceanogr.* 48, 995–1008. 14.
- Jochum, M., Briegleb, B. P., Danabasoglu, G., Large, W. G., Norton, N. J., Jayne, S.

- R., Alford, M. H. and Bryan, F. O. (2013). The impact of oceanic near-inertial waves on climate. *Journal of Climate*, 26(9), pp. 2833-2844.
- Kawaguchi, Y., Wagawa, T. and Igeta, Y. (2020). Near-inertial internal waves and multiple-inertial oscillations trapped by negative vorticity anomaly in the central Sea of Japan. *Progress in Oceanography*, 181, 102240, doi: 10.1016/j.pocean.2019.102240.
- Kim, H. J., Park, Y. G. & Kim, K. (2005) Generation mechanism of near-inertial internal waves observed off the East Coast of Korea. *Cont. Shelf Res.* 25, 1712–1719.
- Kim, D. J., Nam, S. H., Kim, H. R., Moon, W. M. & Kim, K. (2005) Can near-inertial internal waves in the East Sea be observed by synthetic aperture radar? *Geophys. Res. Lett.* 32, 1–4.
- Kim, Y. B., Chang, K. Il, Kim, K., Park, J. H. & Lee, J. H. (2009) Vertical structure of low-frequency currents in the southwestern East Sea (Sea of Japan). *J. Oceanogr.* 65, 259–271.
- Korea Meteorological Agency. (2016). 2015 Typhoon analysis report (11-1360000-00197-10)
- Kunze, E. (1985) Near-inertial wave propagation in geostrophic shear. *J. Phys. Oceanogr.* 15, 544–565.
- Le Boyer, A., Alford, M. H., Pinkel, R., Hennon, T. D., Yang, Y. J., Ko, D. & Nash, J. (2020) Frequency shift of near-inertial waves in the South China Sea. *J. Phys. Oceanogr.* 50, 1121–1135.
- Leaman, K. D. & Sanford, T. B. (1975) Vertical energy propagation of inertial waves: A vector spectral analysis of velocity profiles. *J. Geophys. Res.* 80, 1975–1978.
- Lee, D. K. & Niiler, P. P. (1998) The inertial chimney: The near-inertial energy drainage from the ocean surface to the deep layer. *J. Geophys. Res.* 103, 7579–7591.
- Lee, K., Nam, S. H. and Kim, Y. G. (2019). Statistical Characteristics of East Sea Mesoscale Eddies Detected, Tracked, and Grouped Using Satellite Altimeter Data from 1993 to 2017. *The Sea*, 24(2), pp. 267-281, doi: 10.7850/jkso.2019.24.2.267
- Lee, H. and Nam, S. H. (2021). EC1, long and continuous mooring time series from 1996 to 2020. SEANOE. doi: 10.17882/78916.
- Loder, J. W., and C. Garrett (1978), The 18.6-year cycle of sea surface temperature in shallow seas due to variation in tidal mixing, *J. Geophys.Res.*, 83, 1967 – 1970
- Li, D. et al. (2018) Elevated particulate organic carbon export flux induced by internal waves in the oligotrophic northern South China Sea. *Sci. Rep.* 8, 1–7.
- Lie, H. (1988) Near-inertial current oscillations off the mid-east coast of Korea. *Prog. Oceanogr.* 21, 241–253.
- Lie, H., Shin, C. W., & Seung, Y. H. (1992) Internal tidal oscillations of temperature off Jukbyun on the east coast of Korea. *J. Oceanogr. Soc. Kor.*, 27(3), 228–236.
- Lim, S. H., Jang, C. J., Oh, I. S. & Park, J. J. (2012) Climatology of the mixed layer depth in the East/Japan Sea. *J. Mar. Syst.* 96–97, 1–14.

- Lucas, A. J., Franks, P. J. S. & Dupont, C. L. (2011) Horizontal internal-tide fluxes support elevated phytoplankton productivity over the inner continental shelf. *Limnol. Oceanogr. Fluids Environ.* 1, 56–74.
- Nam, S. H. (2006) Near-inertial current variability off the east coast of Korea. Ph.D. thesis, Seoul Natl Univ, Seoul, Republic of Korea, 132pp.
- Nam, S. & Park, Y. G. (2013) Simulation of wind-induced near-inertial oscillations in a mixed layer near the east coast of Korea in the East/Japan Sea. *Acta Oceanol. Sin.* 32, 11–20.
- Nam, S. H., Kim, D. J., Kim, H. R. & Kim, Y. G. (2007) Typhoon-induced, highly nonlinear internal solitary waves off the east coast of Korea. *Geophys. Res. Lett.* 34, 1–5.
- Nam, S. H. & Park, J. H. (2008) Semidiurnal internal tides off the east coast of Korea inferred from synthetic aperture radar images. *Geophys. Res. Lett.* 35, 1–6.
- Nash, J. D., Kunze, E., Toole, J. M., & Schmitt, R. W. (2004). Internal tide reflection and turbulent mixing on the continental slope. *Journal of Physical Oceanography*, 34(5), 1117-1134.
- Noh, S. & Nam, S. H., (2018) EC1, mooring time-series since 1996. SEANOE. <https://doi.org/10.17882/58134> 29.
- Noh, S. and Nam, S. (2020). Observations of enhanced internal waves in an area of strong mesoscale variability in the south-western East Sea (Japan Sea). *Scientific Reports*, 10(1), pp.1-13.
- Nikurashin, M., Ferrari, R., Grisouard, N. & Polzin, K. (2014) The impact of finite-amplitude bottom topography on internal wave generation in the Southern Ocean. *J. Phys. Oceanogr.* 44, 2938–2950
- Niwa, Y., & Hibiya, T. (2001). Numerical study of the spatial distribution of the M2 internal tide in the Pacific Ocean. *Journal of Geophysical Research: Oceans*, 106(C10), 22441-22449..
- Niwa, Y. & Hibiya, T. (2014) Generation of baroclinic tide energy in a global three-dimensional numerical model with different spatial grid resolutions. *Ocean Model.* 80, 59–73.
- Nycander, J. (2005). Generation of internal waves in the deep ocean by tides. *Journal of Geophysical Research: Oceans*, 110(C10).
- MacKinnon, J. A. & Winters, K. B. (2005) Subtropical catastrophe: Significant loss of low-mode tidal energy at 28.9. *Geophys. Res. Lett.* 32, 1–5.
- MacKinnon, J. A. et al. (2017) Climate process team on internal wave-driven ocean mixing. *Bull. Am. Meteorol. Soc.* 98, 2429–2454. 27.
- Melet, A., Hallberg, R., Legg, S., Nikurashin, M., Polzin, K. L., & Adcroft, A. (2016). Climatic impacts of parameterized internal-wave driven mixing. American Geophysical Union, 2016, PC24B-2140.
- Min, Y., Jeong, J. Y., Jang, C. J., Lee, J., Jeong, J., Min, I. K., Shim, J. S. and Kim, Y. S. (2020). Quality Control of Observed Temperature Time Series from the Korea Ocean Research Stations: Preliminary Application of Ocean Observation Initiative's Approach and Its Limitation. *Ocean and Polar Research*, 42(3), pp.195-210, doi:

10.4217/OPR.2020.42.3.195.

- Mitchell, D. A., Teague, W. J., Wimbush, M., Watts, D. R., & Sutyrin, G. G. (2005). The Dok Cold Eddy, *Journal of Physical Oceanography*, 35(3), 273-288.
- Mori, K., Matsuno, T. and Senju, T. (2005). Seasonal/Spatial Variations of the Near-Inertial Oscillations in the Deep Water of the Japan Sea. *J Oceanogr*, 61(4), pp. 761–773, doi: 10.1007/s10872-005-0082-7.
- Morimoto, A., Yanagi, T., & Kaneko, A. (2000). Tidal correction of altimetric data in the Japan Sea. *Journal of oceanography*, 56(1), 31-41.
- Muacho, S., Da Silva, J. C. B., Brotas, V. & Oliveira, P. B. (2013) Effect of internal waves on near-surface chlorophyll concentration and primary production in the Nazaré Canyon (west of the Iberian Peninsula). *Deep. Res. Part I Oceanogr. Res. Pap.* 81, 89–96.
- Mulet, S., Rio, M. H., Etienne, H., Artana, C., Cancet, M., Dibarboure, G., ... & Strub, P. T. (2021). The new CNES-CLS18 global mean dynamic topography. *Ocean Science*, 17(3), 789-808.
- Müller, P. & Briscoe, M. (2000) Diapycnal mixing and internal waves. *Oceanography*. 13, 98–103.
- Munk, W. & Wunsch, C. (1998) Abyssal recipes II: Energetics of tidal and wind mixing. *Deep. Res. Part I Oceanogr. Res. Pap.* 45, 1977–2010.
- Okubo, A. (1970) Horizontal dispersion of floatable particles in the vicinity of velocity singularities such as convergences. *Deep. Res. Oceanogr. Abstr.* 17, 445–454.
- Pan, X., Wong, G. T. F., Shiah, F. K. & Ho, T. Y. (2012) Enhancement of biological productivity by internal waves: Observations in the summertime in the northern South China Sea. *J. Oceanogr.* 68, 427–437.
- Park, J. J., Kim, K. & Crawford, W. R. (2004) Inertial currents estimated from surface trajectories of ARGO floats. *Geophys. Res. Lett.* 31, 2–5.
- Park, J. H. & Watts, D. R. (2005) Near-inertial oscillations interacting with mesoscale circulation in the southwestern Japan/East Sea. *Geophys. Res. Lett.* 32, 1–4.
- Park, J. H. & Watts, D. R. (2006) Internal tides in the southwestern Japan/East Sea. *J. Phys. Oceanogr.* 36, 22–34.
- Park, J. J., Kim, K. and Schmitt, R. W. (2009). Global distribution of the decay timescale of mixed layer inertial motions observed by satellite-tracked drifters, *J. Geophys. Res.*, 114, C11010, doi:10.1029/2008JC005216.
- Plueddemann, A. J. & Pinkel, R. (1989) Characterization of the patterns of diel migration using a Doppler sonar. *Deep Sea Res. Part A, Oceanogr. Res. Pap.* 36, 509–530.
- Pollard, R. T. & Millard, R. C. (1970) Comparison between observed and simulated wind-generated inertial oscillations. *Deep. Res. Oceanogr. Abstr.* 17.
- Polzin, K. L. (2008) Mesoscale eddy-internal wave coupling. Part I: Symmetry, wave capture, and results from the mid-ocean dynamics experiment. *J. Phys. Oceanogr.* 38, 2556–2574.
- Polzin, K. L. (2010) Mesoscale eddy-internal wave coupling. Part II: Energetics and

- results from PolyMode. *J. Phys. Oceanogr.* 40, 789–801.
- Polzin, K. L. & Lvov, Y. V. (2011) Toward regional characterizations of the oceanic internal wavefield. *Rev. Geophys.* 49, 1–61. 15.
- Price, J. F. (1981). Upper ocean response to a hurricane. *Journal of Physical Oceanography*, 11(2), pp. 153-175.
- Rainville, L. & Pinkel, R. (2006) Propagation of low-mode internal waves through the ocean. *J. Phys. Oceanogr.* 36, 1220–1236.
- Rodionov, S. N. (2006). Use of prewhitening in climate regime shift detection. *Geophysical Research Letters*, 33(12).
- Seo, S. et al. (2016) Internal tides in the southwestern East/Japan Sea from observation and simulation. *J. Coast. Res.* 75, 557–561.
- Shcherbina, A. Y., Talley, L. D., Firing, E. & Hacker, P. (2003) Near-surface frontal zone trapping and deep upward propagation of internal wave energy in the Japan/East sea. *J. Phys. Oceanogr.* 33, 900–912. 26.
- Shin, H. -R., Shin, C. -W., Kim, C., Byun, S. -K. and Hwang, S.-C. (2005). Movement and structural variation of warm eddy WE92 for three years in the Western East/Japan Sea, *Deep-Sea Res.*, 52, pp. 1742–1762.
- Song, H., Marshall, J., Campin, J. M., & McGillicuddy Jr, D. J. (2019). Impact of Near-Inertial Waves on Vertical Mixing and Air-Sea CO₂ Fluxes in the Southern Ocean. *Journal of Geophysical Research: Oceans*, 124(7), 4605-4617.
- Song, H., Jeon, C., Chae, J. Y., Lee, E. J., Lee, K. N., Takayama, K., Choi, Y. and Park, J. H. (2020). Effects of Typhoon and Mesoscale Eddy on Generation and Distribution of Near-Inertial Wave Energy in the East Sea. *The Sea*, 25(3), pp. 55-66. doi: 10.7850/JKSO.2020.25.3.055
- Simmons, H. L., Hallberg, R. W. & Arbic, B. K. (2004) Internal wave generation in a global baroclinic tide model. *Deep. Res. Part II Top. Stud. Oceanogr.* 51, 3043–3068.
- Simmons, H. L. (2008) Spectral modification and geographic redistribution of the semi-diurnal internal tide. *Ocean Model.* 21, 126–138.
- Simmons, H. L. & Alford, M. H. (2012) Simulating the long-range swell of internal waves generated by ocean storms. *Oceanography*. 25, 30–41.
- Thomas, L. N. (2017) On the modifications of near-inertial waves at fronts: implications for energy transfer across scales. *Ocean Dyn.* 67, 1335–1350.
- Thomson, R. E., & Emery, W. J. (2014). Data analysis methods in physical oceanography. Newnes.
- Torrence, C. and Compo, G. P. (1998). A practical guide to wavelet analysis. *Bulletin of the American Meteorological society*, 79(1), pp. 61-78.
- Trusenkova, O. O., Stanichnyi, S. V., & Ratner, Y. B. (2007). Major variability modes and wind patterns over the Sea of Japan and adjacent areas. *Izvestiya, Atmospheric and Oceanic Physics*, 43(5), 634-648.
- U.S. Integrated Ocean Observing System. (2019). Manual for Real-Time Quality Control of In-Situ Current Observations. Version 2.1. Silver Spring, MD, U.S. Department of Commerce, National Oceanic and Atmospheric Administration, National Ocean

- Service, Integrated Ocean Observing System, doi:10.25923/sqe9-e310
- Vanneste, J. (2013) Balance and Spontaneous Wave Generation in Geophysical Flows. *Annu. Rev. Fluid Mech.* 45, 147–172.
- Vic, C., Garabato, A. C. N., Green, J. M., Waterhouse, A. F., Zhao, Z., Melet, A., ... & Stephenson, G. R. (2019). Deep-ocean mixing driven by small-scale internal tides. *Nature communications*, 10(1), 1-9.
- Villamaña, M. et al. (2017) Role of internal waves on mixing, nutrient supply and phytoplankton community structure during spring and neap tides in the upwelling ecosystem of Ría de Vigo (NW Iberian Peninsula). *Limnol. Oceanogr.* 62, 1014–1030.
- Whalen, C. B., MacKinnon, J. A., & Talley, L. D. (2018). Large-scale impacts of the mesoscale environment on mixing from wind-driven internal waves. *Nature Geoscience*, 11(11), 842-847.
- Whalen, C.B., de Lavergne, C., Naveira Garabato, A.C. et al. (2020). Internal wave-driven mixing: governing processes and consequences for climate. *Nat Rev Earth Environ* 1, 606–621. doi: 10.1038/s43017-020-0097-z
- Whitt, D. B. & Thomas, L. N. (2015) Resonant generation and energetics of wind-forced near-inertial motions in a geostrophic flow. *J. Phys. Oceanogr.* 45, 181–208.
- Wunsch, C. (1975) Internal tides in the ocean. *Rev. Geophys.* 13, 167–182.
- Xiao, J., Xie, Q., Wang, D., Yang, L., Shu, Y., Liu, C., ... & Chen, G. (2016). On the near-inertial variations of meridional overturning circulation in the South China Sea. *Ocean Science*, 12(1), 335-344.
- Xie, J. H. & Vanneste, J. (2015) A generalised-Lagrangian-mean model of the interactions between near-inertial waves and mean flow. *J. Fluid Mech.* 774, 143–169.
- Yihui, D., & Chan, J. C. (2005). The East Asian summer monsoon: an overview. *Meteorology and Atmospheric Physics*, 89(1), 117-142.
- Zhai, X., Greatbatch, R. J., Eden, C., & Hibiy, T. (2009). On the loss of wind-induced near-inertial energy to turbulent mixing in the upper ocean. *Journal of Physical Oceanography*, 39(11), 3040-3045.
- Zhao, Z., Alford, M. H., Girton, J. B., Rainville, L. & Simmons, H. L. (2016) Global observations of open-ocean mode-1 M2 internal tides. *J. Phys. Oceanogr.* 46, 1657–1684.
- Zhao, Z. (2019). Mapping internal tides from satellite altimetry without blind directions. *Journal of Geophysical Research: Oceans*, 124, 8605– 8625. <https://doi.org/10.1029/2019JC015507>

Abstract in Korean

내부파는 바람과 조석에 의해 주로 생성되어, 생성 해역에서부터 다른 해역으로 전파하고 시간이 지나면 점차 소멸한다. 내부파는 소멸 과정에서 난류 혼합을 증폭시키며 해수 혼합에 필요한 에너지의 상당 부분을 설명하고, 또 에너지를 재분배하는 데 중요한 역할을 한다. 내부파의 쇄파로 인한 난류 혼합은 열을 비롯한 다른 물질들의 수직 혼합에 영향을 미치며, 궁극적으로 열염순환, 해양 생태계, 나아가 기후 시스템에 영향을 주는 것으로 알려져 있다. 두 종류의 장주기 내부파로는 관성 주파수에 가까운 주파수를 가진 준관성주기 내부파와 조석 기원의 내부파인 내부 조석이 있다. 이들의 상호작용, 또는 배경 흐름장(해류 또는 소용돌이)과의 상호작용은 준관성주기와 조석주기보다 짧은 주기의 내부파 혹은 단주기 내부파를 생성한다. 그러나 이들이 해양 혼합과 에너지와 물질 순환에 중요한 역할을 함에도 불구하고 준관성주기 내부파와 내부 조석파로부터 단주기 내부파가 생성되는 과정에 대한 관측은 많이 보고되지 않았다. 이 논문에서는 동해 남서부 해역에서 장기간 연속적으로 얻어진 계류 자료를 이용하여 단주기 내부파의 증폭 원인을 규명하고, 준관성주기 내부파와 반일주기 내부 조석파의 비계절 변동에 대해 고찰하였다.

동해 남서부 해역에서 관측된 단주기 내부파(2–10 시간 주기)의 증폭 원인으로 준관성주기 내부파, 반일주기 내부 조석, 중규모 흐름장, 그리고 이들의 상호작용에 대해 토의하였다. 준관성주기 내부파는 해양 표층에서 국지적인 바람 외력에 의해 생성되며, 중규모 흐름장의 변형률에 비례하여 에너지가 증폭될 수 있음을 보였다. 또한 준관성주기 내부파는 중규모 배경장의 변형률이 상대 와도보다 크게 증가할 때, 중규모 배경정과 비선형 상호 작용하여 에너지가 증폭할 수 있음을 보였다. 반일주기 내부 조석은 관측 위치와 멀리 떨어진 대한해협 북단에서 생성되어 관측 위치로 전파해 오는데, 내부조석의 전파 방향(굴절)은 중규모 흐름장에 좌우된다. 관측된 다섯 번의 단주기 내부파의 증폭은 1) 증폭된 준관성주기 내부파, 2) 증폭된 반일주기 내부조석파, 또는 3) 이들 내부파 간의 상호작용에 의해 일어남을 알 수 있

었다. 본 연구에서 동해 남서부 해역에서의 내부파 증폭으로부터, 동한 난류의 사행 혹은 울릉 난수성 소용돌이와 같은 중규모 흐름장의 상대와도와 변형률이 준관성주기부터 부력주파수까지 이르는 내부파 증폭에 영향을 준다는 것을 밝혀냈다.

동일 해역에서 2000년부터 2020년까지 21년 간 얻어진 유속자료로부터 400 m에서의 준관성주기 운동에너지의 계절내(3–100일 시간 규모) 변동, 경년 변동, 십년 규모 변동을 살펴보았다. 계절내 변동하는 준관성주기 운동에너지는 95% 신뢰수준에서 음의 와도, 중규모 배경장의 양의 변형률, 양의 Okubo–Weiss 조건일 때 그렇지 않은 조건에 비해 약 12배 운동에너지가 유의하게 증가하였다. 또한, 준관성주기 에너지 증폭은 대부분 2010년대에 나타났는데, 2000년부터 2020년까지 400 m에서 부력 주파수의 증가를 고려할 때 2010년대의 준관성주기 에너지가 2000년대에 비해 약 19 % 감소해야 하는 것과는 상반된다. 이는 2000년대와 2010년대의 동해 남서부 해역의 중규모 배경장에서 기인한 것으로, 실제로 관측 해역 인근에서 2014년부터 2016년까지 2년 이상 지속된 울릉 난수성 소용돌이는 음의 와도를 제공하여 준관성주기 운동에너지가 증폭할 수 있도록 하였다.

동일 해역에서 2000년부터 2020년까지 21년 간 관측된 반일주기 내부조석 에너지를 살펴본 결과, 대한해협 북단에서 반일주기 내부조석이 생성 조건을 만족할 때 관측 해역 400 m에서의 반일주기 내부조석 에너지는 95% 신뢰수준에서 유의하게 증가하였다. 반일주기 내부조석 에너지는 14, 28, 56일 주기에서 변동성이 크게 나타나는데, 14일과 28일 주기는 대조–소조 변동 주기와 일치하며, 56일 주기는 중규모 배경장의 변동 주기와 관련이 있다. 생성된 내부조석은 61 %의 확률로 동쪽 굴절을 하며 31 % 확률로 서쪽 굴절하였는데, 이는 대한해협에서 생성된 반일주기 내부 조석과가 중규모 배경장과 상호작용하여 굴절 방향이 달라지는 것을 의미한다.

이 논문에서는 내부파의 증폭 원인을 규명하고, 준관성주기 내부파, 반일주기 내부 조석과 중규모 배경장의 상호작용을 계절내 규모뿐만 아니라 경년 및 십년 규모 변동을 장기간 수집된 연속 시계열 자료로부터 규명하였다. 이 논문을 통해 밝힌 연구 결과는 중규모 배경장에 의해 증폭된 내부파

에서 기인한 혼합이 해양 내 에너지를 재분배하고 자오면 순환이나 해양 내 물질 혼합에 미치는 영향을 계절내 규모, 경년 및 십년 규모 변동으로 살펴보는 연구에 기여할 것으로 기대된다.

Appendix

I. Derivation of dispersion relation for near-inertial waves in the geostrophic currents (Kunze, 1985)

Dispersion relation for near-inertial waves propagating in geostrophic currents is formulated including the mean flow. Assumptions for this dispersion relation are

1. Wave scales are much smaller than flow scales (the WKB approximation)
2. Retain only the interaction terms involving wave shear
3. Mean flow is a quasi-geostrophic motion; mean vertical motion is neglected
4. Wave-wave interaction terms drop out

then, the equations of motion are

$$\frac{\partial u}{\partial t} + (\mathbf{V} \cdot \nabla)u + u \frac{\partial U}{\partial x} + v \frac{\partial U}{\partial y} + w \frac{\partial U}{\partial z} - fv = -\frac{\partial p}{\partial x} \quad (\text{Eq. 1-a})$$

$$\frac{\partial v}{\partial t} + (\mathbf{V} \cdot \nabla)v + u \frac{\partial V}{\partial x} + v \frac{\partial V}{\partial y} + w \frac{\partial V}{\partial z} + fu = -\frac{\partial p}{\partial y} \quad (\text{Eq. 1-b})$$

$$\frac{\partial w}{\partial t} + (\mathbf{V} \cdot \nabla)w = -\frac{\partial p}{\partial z} - b \quad (\text{Eq. 1-c})$$

$$\frac{\partial u}{\partial x} + \frac{\partial v}{\partial y} + \frac{\partial w}{\partial z} = 0 \quad (\text{Eq. 1-d})$$

$$\frac{\partial b}{\partial t} + (\mathbf{V} \cdot \nabla)b + u \frac{\partial B}{\partial x} + v \frac{\partial B}{\partial y} - N^2 w = 0 \quad (\text{Eq. 1-e})$$

where $\mathbf{v} = (u, v, w)$ and $\mathbf{V} = (U, V, W)$ are the wave and the mean flow velocity, b and B are the wave and mean flow buoyancy, p the wave induced pressure (normalized by ρ_0), and $N = \left[-\frac{g}{\rho_0} \frac{\partial \rho}{\partial z} \right]^{1/2}$ the time-averaged buoyancy frequency.

To obtain the dispersion relation, the plane wave form solution is used here,

$$\psi = \psi_0 e^{i(k_x x + k_y y + k_z z - \omega t)}$$

Where ω is the fixed frequency in Eulerian frame, and $\mathbf{k} = (k_x, k_y, k_z)$ is the wavevector.

First, start with the Eq. 1-a,

$$\frac{\partial u}{\partial t} + (\mathbf{V} \cdot \nabla) u + u \frac{\partial U}{\partial x} + v \frac{\partial U}{\partial y} + w \frac{\partial U}{\partial z} - fv = -\frac{\partial p}{\partial x} \quad (\text{Eq. 1-a})$$

expansion and transposition the Eq. 1-a,

$$\frac{\partial u}{\partial t} + U \frac{\partial u}{\partial x} + V \frac{\partial u}{\partial y} + W \frac{\partial u}{\partial z} + u \frac{\partial U}{\partial x} + v \frac{\partial U}{\partial y} + w \frac{\partial U}{\partial z} - fv + \frac{\partial p}{\partial x} = 0$$

substitution plane wave solution,

$$-i\omega u + ik_x U u + ik_y V u + ik_z W u + u \frac{\partial U}{\partial x} + v \frac{\partial U}{\partial y} + w \frac{\partial U}{\partial z} - fv + ik_x p = 0$$

then,

$$-iu\{\omega - (k_x U + k_y V + k_z W)\} + u \frac{\partial U}{\partial x} + v \frac{\partial U}{\partial y} + w \frac{\partial U}{\partial z} - fv + ik_x p = 0$$

Using the Doppler shift ($\mathbf{k} \cdot \mathbf{V}$),

$$\omega_0 = \omega - (\mathbf{k} \cdot \mathbf{V})$$

then,

$$-iu\omega_0 + u \frac{\partial U}{\partial x} + v \frac{\partial U}{\partial y} + w \frac{\partial U}{\partial z} - fv + ik_x p = 0$$

The Eq.2-a is obtained.

$$u(-i\omega_0 + \frac{\partial U}{\partial x}) + v(-f + \frac{\partial U}{\partial y}) + w \frac{\partial U}{\partial z} + ik_x p = 0 \quad (\text{Eq. 2-a})$$

Same manner with Eq.1-b.

$$\frac{\partial v}{\partial t} + (\mathbf{V} \cdot \nabla) v + u \frac{\partial V}{\partial x} + v \frac{\partial V}{\partial y} + w \frac{\partial V}{\partial z} + fu = -\frac{\partial p}{\partial y} \quad (\text{Eq. 1-b})$$

expansion and transposition the Eq. 1-b,

$$\frac{\partial v}{\partial t} + U \frac{\partial v}{\partial x} + V \frac{\partial v}{\partial y} + W \frac{\partial v}{\partial z} + u \frac{\partial V}{\partial x} + v \frac{\partial V}{\partial y} + w \frac{\partial V}{\partial z} + fu + \frac{\partial p}{\partial y} = 0$$

substitution plane wave solution,

$$\begin{aligned} -i\omega v + ik_x U v + ik_y V v + ik_z W v + u \frac{\partial V}{\partial x} + v \frac{\partial V}{\partial y} + w \frac{\partial V}{\partial z} + fu + ik_y p &= 0 \\ -iv\{\omega - (k_x U + k_y V + k_z W)\} + u \frac{\partial V}{\partial x} + v \frac{\partial V}{\partial y} + w \frac{\partial V}{\partial z} + fu + ik_y p &= 0 \end{aligned}$$

Using the Doppler shift,

$$-iv\omega_0 + u \frac{\partial V}{\partial x} + v \frac{\partial V}{\partial y} + w \frac{\partial V}{\partial z} + fu + ik_y p = 0$$

The Eq.2-b is obtained.

$$u(f + \frac{\partial V}{\partial x}) + v(-i\omega_0 + \frac{\partial V}{\partial y}) + w \frac{\partial V}{\partial z} + ik_y p = 0 \quad (\text{Eq. 2-b})$$

Same manner with Eq.1-c,

$$\frac{\partial w}{\partial t} + (\mathbf{V} \cdot \nabla)w = -\frac{\partial p}{\partial z} - b \quad (\text{Eq. 1-c})$$

expansion and transposition the Eq. 1-c,

$$\frac{\partial w}{\partial t} + U \frac{\partial w}{\partial x} + V \frac{\partial w}{\partial y} + W \frac{\partial w}{\partial z} + \frac{\partial p}{\partial z} + b = 0$$

substitution plane wave solution,

$$\begin{aligned} -i\omega w + ik_x U w + ik_y V w + ik_z W w + ik_z p + b &= 0 \\ -iw\{\omega - (k_x U + k_y V + k_z W)\} + ik_z p + b &= 0 \end{aligned}$$

Using the Doppler shift, the Eq.2-c is obtained.

$$-iu\omega_0 + ik_z p + b = 0 \quad (\text{Eq. 2-c})$$

For the Eq.1-d,

$$\frac{\partial u}{\partial x} + \frac{\partial v}{\partial y} + \frac{\partial w}{\partial z} = 0 \quad (\text{Eq. 1-d})$$

substitution plane wave solution, then the Eq.2-d is obtained.

$$ik_x u + ik_y v + ik_z w = 0 \quad (\text{Eq. 2-d})$$

For the Eq.1-e,

$$\frac{\partial b}{\partial t} + (\mathbf{V} \cdot \nabla) b + u \frac{\partial B}{\partial x} + v \frac{\partial B}{\partial y} - N^2 w = 0 \quad (\text{Eq. 1-e})$$

substitution thermal wind relation,

$$\begin{aligned} -f \frac{\partial V}{\partial z} &= \frac{\partial B}{\partial x} \\ -f \frac{\partial U}{\partial z} &= \frac{\partial B}{\partial y} \end{aligned}$$

then,

$$\frac{\partial b}{\partial t} + (\mathbf{V} \cdot \nabla) b - fu \frac{\partial V}{\partial z} + fv \frac{\partial U}{\partial z} - N^2 w = 0$$

expansion and transposition

$$\frac{\partial b}{\partial t} + U \frac{\partial b}{\partial z} + V \frac{\partial b}{\partial z} + W \frac{\partial b}{\partial z} - fu \frac{\partial V}{\partial z} + fv \frac{\partial U}{\partial z} - N^2 w = 0$$

substitution plane wave solution,

$$\begin{aligned} -i\omega b + ik_x Ub + ik_y Vb + ik_z Wb - fu \frac{\partial V}{\partial z} + fv \frac{\partial U}{\partial z} - N^2 w &= 0 \\ -ib\{\omega - (k_x U + k_y V + k_z W)\} - fu \frac{\partial V}{\partial z} + fv \frac{\partial U}{\partial z} - N^2 w &= 0 \end{aligned}$$

Using the Doppler shift, then the Eq.2-e is obtained

$$-ib\omega_0 - fu \frac{\partial V}{\partial z} + fv \frac{\partial U}{\partial z} - N^2 w = 0 \quad (\text{Eq. 2-e})$$

The equations of motion are changed to,

$$u(-i\omega_0 + \frac{\partial U}{\partial x}) + v(-f + \frac{\partial U}{\partial y}) + w\frac{\partial U}{\partial z} + ik_x p = 0 \quad (\text{Eq. 2-a})$$

$$u(f + \frac{\partial V}{\partial x}) + v(-i\omega_0 + \frac{\partial V}{\partial y}) + w\frac{\partial V}{\partial z} + ik_y p = 0 \quad (\text{Eq. 2-b})$$

$$-iu\omega_0 + ik_z p + b = 0 \quad (\text{Eq. 2-c})$$

$$ik_x u + ik_y v + ik_z w = 0 \quad (\text{Eq. 2-d})$$

$$-ib\omega_0 - fu\frac{\partial V}{\partial z} + fv\frac{\partial U}{\partial z} - N^2 w = 0 \quad (\text{Eq. 2-e})$$

Then, convert to matrix form

$$\begin{pmatrix} (-i\omega_0 + \frac{\partial U}{\partial x}) & (-f + \frac{\partial U}{\partial y}) & \frac{\partial U}{\partial z} & ik_x & 0 \\ (f + \frac{\partial V}{\partial x}) & (-i\omega_0 + \frac{\partial V}{\partial y}) & \frac{\partial V}{\partial z} & ik_y & 0 \\ 0 & 0 & -i\omega_0 & ik_z & 1 \\ ik_x & ik_y & ik_z & 0 & 0 \\ -f\frac{\partial V}{\partial z} & f\frac{\partial U}{\partial z} & -N^2 & 0 & -i\omega_0 \end{pmatrix} \begin{pmatrix} u \\ v \\ w \\ p \\ b \end{pmatrix} = 0$$

From the determinant of left-side matrix, then cubic expression for the intrinsic frequency ω_0 is obtained (Same as A1 in Kunze, 1985).

$$\begin{aligned} & ik^2 \omega_0^3 + \omega_0^2 \left[\left(\frac{\partial V}{\partial x} + \frac{\partial U}{\partial y} \right) k_x k_y + \left(\frac{\partial U}{\partial z} k_x + \frac{\partial V}{\partial z} k_y \right) k_z - \frac{\partial U}{\partial x} k_y^2 - \frac{\partial V}{\partial y} k_x^2 - \left(\frac{\partial V}{\partial x} + \frac{\partial U}{\partial y} \right) k_z^2 \right] - i\omega_0 \left[N^2 k_H^2 + f_{eff}^2 k_z^2 + \left(2f + \frac{\partial V}{\partial x} \right) \frac{\partial U}{\partial z} k_y k_z + \left(-2f + \frac{\partial U}{\partial y} \right) \frac{\partial V}{\partial z} k_x k_z - \frac{\partial U}{\partial x} \frac{\partial V}{\partial z} k_y k_z - \frac{\partial V}{\partial y} \frac{\partial U}{\partial z} k_x k_z \right] + \left\{ N^2 \left[\frac{\partial U}{\partial x} k_y^2 - \left(\frac{\partial U}{\partial y} + \frac{\partial V}{\partial x} \right) k_x k_y + \frac{\partial V}{\partial y} k_x^2 \right] + f \left(\frac{\partial V}{\partial z} k_x - \frac{\partial U}{\partial z} k_y \right) \left(\frac{\partial U}{\partial z} k_x - \frac{\partial V}{\partial z} k_y \right) - fk_z \left[\left(f + \frac{\partial V}{\partial x} \right) \frac{\partial U}{\partial z} k_x + \left(f - \frac{\partial U}{\partial y} \right) \frac{\partial V}{\partial z} k_y \right] + \frac{\partial U}{\partial x} \frac{\partial U}{\partial z} k_y - \frac{\partial V}{\partial y} \frac{\partial V}{\partial z} k_x \right\} = 0 \end{aligned}$$

where k_H is the horizontal wavenumber.

$$\begin{aligned}
|A| &= \begin{vmatrix} A_{11} & A_{12} & A_{13} & A_{14} & A_{15} \\ A_{21} & A_{22} & A_{23} & A_{24} & A_{25} \\ A_{31} & A_{32} & A_{33} & A_{34} & A_{35} \\ A_{41} & A_{42} & A_{43} & A_{44} & A_{45} \\ A_{51} & A_{52} & A_{53} & A_{54} & A_{55} \end{vmatrix} \\
&= A_{11} \begin{vmatrix} A_{22} & A_{23} & A_{24} & A_{25} \\ A_{32} & A_{33} & A_{34} & A_{35} \\ A_{42} & A_{43} & A_{44} & A_{45} \\ A_{52} & A_{53} & A_{54} & A_{55} \end{vmatrix} - A_{21} \begin{vmatrix} A_{12} & A_{13} & A_{14} & A_{15} \\ A_{32} & A_{33} & A_{34} & A_{35} \\ A_{42} & A_{43} & A_{44} & A_{45} \\ A_{52} & A_{53} & A_{54} & A_{55} \end{vmatrix} \\
&\quad + A_{31} \begin{vmatrix} A_{12} & A_{13} & A_{14} & A_{15} \\ A_{22} & A_{23} & A_{24} & A_{25} \\ A_{42} & A_{43} & A_{44} & A_{45} \\ A_{52} & A_{53} & A_{54} & A_{55} \end{vmatrix} - A_{41} \begin{vmatrix} A_{12} & A_{13} & A_{14} & A_{15} \\ A_{22} & A_{23} & A_{24} & A_{25} \\ A_{32} & A_{33} & A_{34} & A_{35} \\ A_{52} & A_{53} & A_{54} & A_{55} \end{vmatrix} \\
&\quad + A_{51} \begin{vmatrix} A_{12} & A_{13} & A_{14} & A_{15} \\ A_{22} & A_{23} & A_{24} & A_{25} \\ A_{32} & A_{33} & A_{34} & A_{35} \\ A_{42} & A_{43} & A_{44} & A_{45} \end{vmatrix}
\end{aligned}$$

Figure I.1. Expansion of the determinant (<https://semath.info/src/determinant-five-by-five.html>)

The effective Coriolis frequency is defined by,

$$f_{eff} = \left[f^2 + f \left(\frac{\partial V}{\partial x} - \frac{\partial U}{\partial y} \right) - \frac{\partial U}{\partial x} \frac{\partial V}{\partial y} \right]^{1/2}$$

Scale analysis applied to cubic expression for the intrinsic frequency using two assumptions,

1. The ratio of vertical to horizontal wavelengths

$$\frac{(k_x, k_y)}{k_z} \sim \frac{f}{N} \sqrt{2\varepsilon}$$

where $\varepsilon \ll 1$ implying $k \sim k_z$

2. Horizontal shear is much less than f

$$\left| \frac{\partial U}{\partial y} \right|, \left| \frac{\partial V}{\partial x} \right| \sim f \delta_f$$

where $\delta_f \ll 1$.

3. The effective Coriolis frequency is simplified to

$$f_{eff} \approx f + \frac{1}{2} \left(\frac{\partial V}{\partial x} - \frac{\partial U}{\partial y} \right) = f + \frac{1}{2} \zeta$$

and vorticity ζ is typically $\ll 0.2f$

4. Final assumption is

$$\left| \frac{\partial U}{\partial z} \right|, \left| \frac{\partial V}{\partial z} \right| \sim N \delta_N$$

where $\delta_N \ll 1$.

Put $\omega_0 = f$, then the magnitudes of each terms in cubic expression are

$$(1) k^2 \omega_0^3 \rightarrow k_z^2 f^3$$

$$(2) \omega_0^2 \left(\frac{\partial V}{\partial x} + \frac{\partial U}{\partial y} \right) k_x k_y \rightarrow f^2 f \delta_f k^2 = f^2 f \delta_f \left(\frac{f}{N} k_z \sqrt{2\varepsilon} \right)^2 = \frac{f^5}{N^2} k_z^2 \delta_f^2 2\varepsilon$$

$$(3) \omega_0^2 \left(\frac{\partial U}{\partial z} k_x + \frac{\partial V}{\partial z} k_y \right) k_z \rightarrow f^2 f \delta_f k k_z = f^2 f \delta_f \frac{f}{N} k_z \sqrt{2\varepsilon} k_z = \frac{f^4}{N} k_z^2 \delta_f \sqrt{2\varepsilon}$$

$$(4) \omega_0^2 \left(-\frac{\partial U}{\partial x} k_y^2 - \frac{\partial V}{\partial y} k_x^2 \right) \rightarrow f^2 f \delta_f k^2 = f^2 f \delta_f \left(\frac{f}{N} k_z \sqrt{2\varepsilon} \right)^2 = \frac{f^5}{N^2} k_z^2 \delta_f^2 2\varepsilon$$

$$(5) -\omega_0^2 \left(\frac{\partial V}{\partial x} + \frac{\partial U}{\partial y} \right) k_z^2 \rightarrow f^2 f \delta_f k_z^2 = f^3 \delta_f k_z^2$$

$$(6) -i\omega_0 N^2 k_H^2 \rightarrow f N^2 \left(\frac{f}{N} k_z \sqrt{2\varepsilon} \right)^2 = f^3 k_z 2\varepsilon$$

$$(7) -i\omega_0 f_{eff}^2 k_z^2 \rightarrow f f^2 k_z^2 = f^3 k_z^2$$

$$(8) -i\omega_0 \left\{ \left(2f + \frac{\partial V}{\partial x} \right) \frac{\partial U}{\partial z} k_y k_z + \left(-2f + \frac{\partial U}{\partial y} \right) \frac{\partial V}{\partial z} k_x k_z \right\}$$

$$\rightarrow f f N \delta_N k_z \frac{f}{N} \sqrt{2\varepsilon} k_z = f^3 \delta_N k_z^2 \sqrt{2\varepsilon}$$

$$(9) -i\omega_0 \left(-\frac{\partial U}{\partial x} \frac{\partial V}{\partial z} k_y k_z - \frac{\partial V}{\partial y} \frac{\partial U}{\partial z} k_x k_z \right)$$

$$\rightarrow ff\delta_f N \delta_N k_z \frac{f}{N} \sqrt{2\varepsilon} k_z = f^3 \delta_f \delta_N k_z^2 \sqrt{2\varepsilon}$$

$$(10) N^2 \left[\frac{\partial U}{\partial x} k_y^2 - \left(\frac{\partial U}{\partial y} + \frac{\partial V}{\partial x} \right) k_x k_y + \frac{\partial V}{\partial y} k_x^2 \right]$$

$$\rightarrow N^2 f \delta_f \left(\frac{f}{N} k_z \sqrt{2\varepsilon} \right)^2 = f^3 \delta_f k_z^2 2\varepsilon$$

$$(11) f \left(\frac{\partial V}{\partial z} k_x - \frac{\partial U}{\partial z} k_y \right) \left(\frac{\partial U}{\partial z} k_x - \frac{\partial V}{\partial z} k_y \right)$$

$$\rightarrow \left(f N \delta_N k_z \frac{f}{N} \sqrt{2\varepsilon} \right) \left(N \delta_N k_z \frac{f}{N} \sqrt{2\varepsilon} \right) = f^3 \delta_N^2 k_z^2 2\varepsilon$$

$$(12) -fk_z \left[\left(f + \frac{\partial V}{\partial x} \right) \frac{\partial U}{\partial z} k_x + \left(f - \frac{\partial U}{\partial y} \right) \frac{\partial V}{\partial z} k_y \right]$$

$$\rightarrow fk_z \left(f N \delta_N k_z \frac{f}{N} \sqrt{2\varepsilon} \right) = f^3 \delta_N k_z^2 \sqrt{2\varepsilon}$$

$$(13) \frac{\partial U}{\partial x} \frac{\partial U}{\partial z} k_y - \frac{\partial V}{\partial y} \frac{\partial V}{\partial z} k_x$$

$$\rightarrow f \delta_f N \delta_N k_z \frac{f}{N} \sqrt{2\varepsilon} = f^2 \delta_N k_z \sqrt{2\varepsilon}$$

From scale analysis, the main balance terms are (1) and (7).

In baroclinic flow,

$$\frac{\partial U}{\partial Z} \neq 0, \quad \frac{\partial V}{\partial Z} \neq 0$$

then, cubic expression for the intrinsic frequency ω_0 becomes

$$\begin{aligned} \omega_0^3 - i\omega_0^2 & \left[\frac{\partial U}{\partial Z} k_x + \frac{\partial V}{\partial Z} k_y \right] \frac{1}{k_z} - \omega_0 \left[\frac{N^2 k_H^2}{k_z^2} + f_{eff}^2 + 2f \left(\frac{\partial U}{\partial Z} k_y - \frac{\partial V}{\partial Z} k_x \right) \frac{1}{k_z} \right] \\ & + i \left\{ f^2 \left(\frac{\partial U}{\partial Z} k_x + \frac{\partial V}{\partial Z} k_y \right) \frac{1}{k_z} \right. \\ & \left. + \frac{N^2}{k_z^2} \left[\frac{\partial U}{\partial x} k_y^2 - \left(\frac{\partial U}{\partial y} + \frac{\partial V}{\partial x} \right) k_x k_y + \frac{\partial V}{\partial y} k_x^2 \right] \right\} = 0 \end{aligned}$$

Solving for ω_0 ,

$$\omega_0 = \omega - (\mathbf{k} \cdot \mathbf{V}) \approx \left[f_{eff} + \frac{N^2 k_H^2}{2fk_z^2} + \frac{1}{k_z} \left(\frac{\partial U}{\partial Z} k_x + \frac{\partial V}{\partial Z} k_y \right) \right] + i \left\{ \frac{\zeta}{2fk_z} \left(\frac{\partial U}{\partial Z} k_x + \frac{\partial V}{\partial Z} k_y \right) + \frac{N^2}{k_z^2} \left[\frac{\partial U}{\partial x} k_y^2 - \left(\frac{\partial U}{\partial y} + \frac{\partial V}{\partial x} \right) k_x k_y + \frac{\partial V}{\partial y} k_x^2 \right] \right\}$$

$$\frac{\partial V}{\partial z} k_y \Big) + \frac{N^2}{2f{k_z}^2} \left[\frac{\partial U}{\partial x} {k_y}^2 - \left(\frac{\partial U}{\partial y} + \frac{\partial V}{\partial x} \right) k_x k_y + \frac{\partial V}{\partial y} {k_x}^2 \right] \Big\}$$